Hemodynamic Modeling of Cerebral Aneurysms

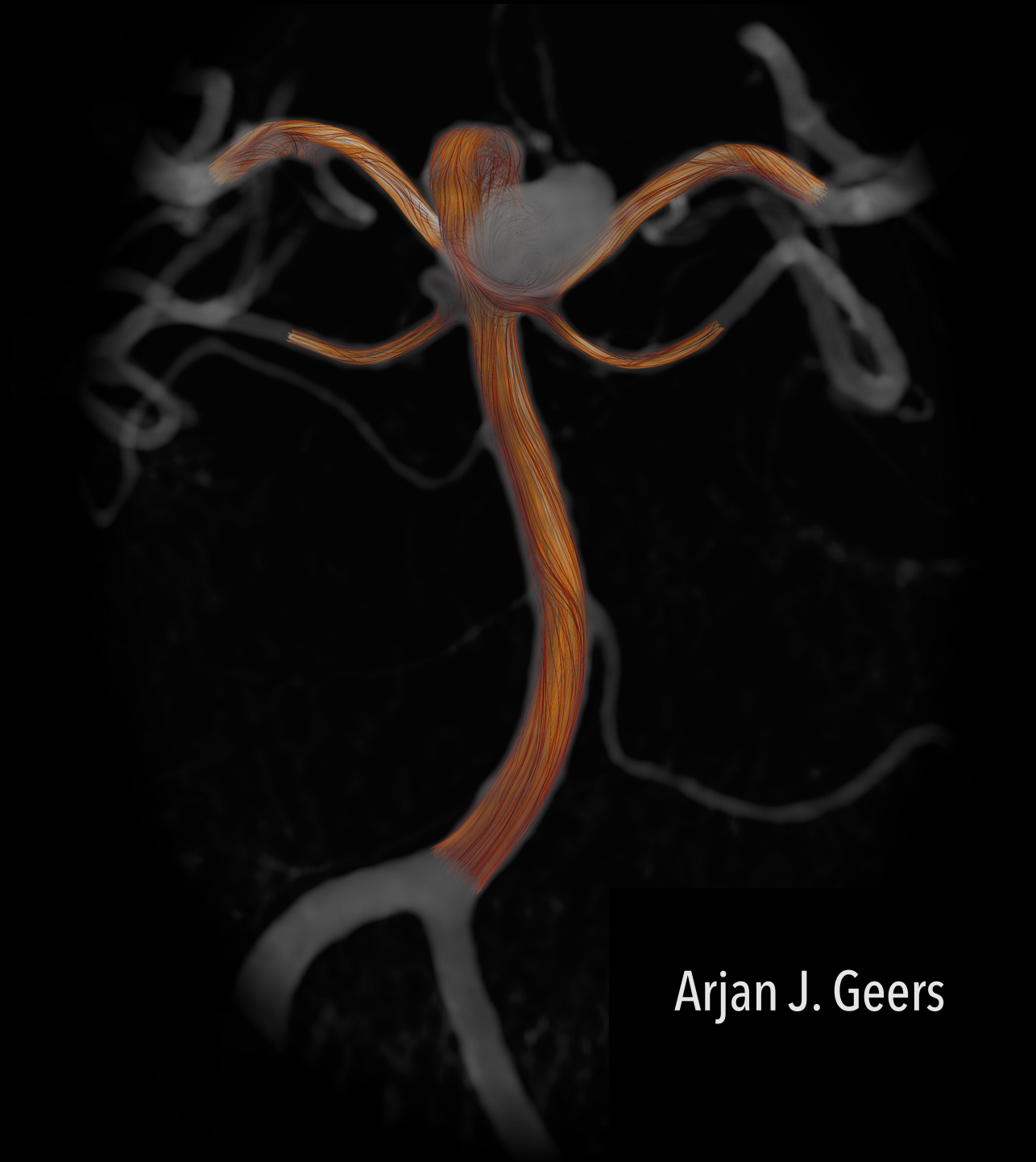

Arjan J. Geers

Hemodynamic Modeling of Cerebral Aneurysms

Hemodynamic modeling of cerebral aneurysms; PhD thesis
Universitat Pompeu Fabra, Barcelona, Spain

This thesis was typeset using LaTeX2e and output as PDF. Fonts: Avenir for the cover, `qtxmath` for math, Bitstream Vera Sans for plots and diagrams, and TeX Gyre Termes (`tgtermes`) for all else. Plots were created with Python library Matplotlib [86]. Visualizations of vascular models and CFD simulations were created in Paraview and ANSYS CFX-Post. Drawings, diagrams, and image compilations were created in Inkscape. Color schemes: RdBu for contour plots and 7-class Set1 by ColorBrewer 2.0 [23] for all else.

Cover: Basilar artery with a double-lobed aneurysm at its tip, viewed from posterior to anterior. A 3D rotational angiography image is shown together with streamlines visualizing the simulated blood flow field. The anterior lobe receives a large portion of the flow coming from the parent vessel, while the posterior lobe is a region of low flow velocity.

Hemodynamic Modeling of Cerebral Aneurysms

Arjan J. Geers

PhD Thesis / 2014

Department of Information and Communication Technologies
Universitat Pompeu Fabra, Barcelona, Spain

Supervisors: Prof. Alejandro F. Frangi
Universitat Pompeu Fabra, Barcelona, Spain
The University of Sheffield, Sheffield, UK

Dr. Ignacio Larrabide
Universitat Pompeu Fabra, Barcelona, Spain
Universidad Nacional del Centro de la Provincia de Buenos Aires, Tandil, Argentina

Reading Committee: Prof. Yiannis Ventikos
University College London, London, UK

Dr. Juan M. Macho
Hospital Clínic i Provincial de Barcelona, Barcelona, Spain

Dr. Petia Radeva
Universitat de Barcelona, Barcelona, Spain
Computer Vision Center, Barcelona, Spain

Dr. Coloma Ballester (reserve)
Universitat Pompeu Fabra, Barcelona, Spain

Prof. Miguel Ángel González Ballester (reserve)
Universitat Pompeu Fabra, Barcelona, Spain

This thesis was submitted on 22 September 2014 and defended on 12 January 2015.

The work described in this thesis was carried out at the Center for Computational Imaging and Simulation Technologies in Biomedicine (CISTIB), Department of Information and Communication Technologies, Universitat Pompeu Fabra, Barcelona, Spain; and the Biomedical Research Networking Centre on Bioengineering, Biomaterials and Nanomedicine (CIBER-BBN).

Financial support for this work was provided by the Spanish Ministry of Science and Innovation through projects CDTEAM (CEN-2005003) and cvREMOD (CEN-20091044), the European Commission through projects @neurIST (FP6-IST-027703) and VPH-NoE (FP7-IST-223920), and Philips Healthcare. ANSYS UK Ltd provided us with free licenses for their mesh generation and CFD simulation software.

To Cata and her many answers

Abstract / Resumen

Abstract — Cerebral aneurysms are localized, pathological dilatations of cerebral arteries. Their rupture causes a subarachnoid hemorrhage and is associated with high rates of morbidity and mortality. Better understanding of the mechanisms underlying aneurysm pathophysiology is crucial for the development of new preventive and therapeutic strategies.

In addition to systemic risk factors such as hypertension, gender and age, hemodynamics is believed to play an important role as local risk factor. While techniques exist to measure the hemodynamics in vivo, they provide low-resolution data and are limited to assessing the patient's current condition. Over the last decade, the emergence of computational modeling has greatly improved our understanding of how hemodynamic stresses are associated to the initiation, growth and rupture of aneurysms and how they are altered by endovascular treatment devices.

Hemodynamic simulations are obtained using computational fluid dynamics (CFD) techniques. They are personalised by extracting the vascular geometry from medical images. Other input parameters, such as the blood viscosity and flow rate boundary conditions, are typically estimated from average physiological measurements reported in the literature. Before hemodynamic simulations can become part of clinical decision-making, it is essential that we assess their reproducibility and accuracy.

The aim of this thesis was to identify hemodynamic factors that can be reliably computed and that can be used to study aneurysm pathophysiology. We addressed the following questions: 1. Are hemodynamic simulations reproducible across imaging modalities commonly used in clinical practice? 2. Are hemodynamic simulations reproducible across different CFD solvers? 3. Can computationally inexpensive steady flow simulations be used to answer clinically relevant questions? 4. Which reliable hemodynamic factors are associated with aneurysm initiation?

Resumen — Los aneurismas cerebrales son dilataciones patológicas y localizadas de las arterias cerebrales. Su ruptura causa una hemorragia subaracnoidea y está asociada a altas tasas de morbilidad y mortalidad. Un mejor entendimiento de los mecanismos de fondo de la patofisiología de los aneurismas es crucial para desarrollar nuevas estrategias preventivas y terapéuticas.

Adicionalmente a los factores de riesgo sistémicos, como la hipertensión, el género y la edad, se cree que la hemodinámica juega un papel importante como factor de riesgo local. Mientras que hay técnicas para medir la hemodinámica *in vivo*, éstas proveen datos de baja resolución y están limitadas a evaluar la condición actual del paciente. Durante la última década, la emergencia del modelado computacional ha mejorado nuestro entendimiento de como los estreses hemodinámicos están asociados a la iniciación, el crecimiento y la ruptura de los aneurismas, y, como son alterados por los tratamientos con dispositivos endovasculares.

Las simulaciones hemodinámicas se obtienen usando técnicas de dinámica computacional de fluidos. Éstas se personalizan extrayendo la geometria vascular a partir de imágenes médicas. Otros parámetros de contorno, como la viscosidad sanguínea y la velocidad de flujo, típicamente se estiman de medidas fisiológicas promedio reportadas en la literatura. Antes de que las simulaciones hemodinámicas puedan hacerse parte de las decisiones clínicas rutinarias, es esencial evaluar su reproducibilidad y exactitud.

El objetivo de esta tesis era identificar factores hemodinámicos que puedan calcularse confiablemente y puedan usarse para estudiar la patofisiología de los aneurismas. Hemos abordado las siguientes preguntasa: 1. Son las simulaciones hemodinámicas reproducibles entre modalidades de imagen usadas comunmente en la práctica clinica? 2. Son las simulaciones hemodinámicas reproducibles entre diferentes solvers computacionales? 3. Podemos usar simulaciones computacionalmente económicas de flujo estable para responder preguntas clinicamente relevantes? 4. Cuales factores hemodinámicos confiables están asociados con la iniciación de aneurismas?

Contents

Acronyms

3DRA	Three-dimensional rotational angiography
ACA	Anterior cerebral artery
ACA-A1	A1 segment of the anterior cerebral artery
ACA-A2	A2 segment of the anterior cerebral artery
ACoA	Anterior communicating artery
AChA	Anterior choroidal artery
AFI	Aneurysm formation indicator
BA	Basilar artery
CFD	Computational fluid dynamics
CT	Computed tomography
CTA	Computed tomographic angiography
CV	Coefficient of variation
DSA	Digital subtraction angiography
ED	End diastole
FRW	Flow rate waveform
GON	Gradient oscillatory number
HR	Heart rate
ICA	Internal carotid artery
ICS	International Interdisciplinary Cerebrovascular Symposium
MCA	Middle cerebral artery
MISR	Maximally inscribed sphere radius
MRA	Magnetic resonance angiography
NSI	Nonsphericity index
RMSD	Root-mean-square deviation
RMSE	Root-mean-square error

OphthA	Ophthalmic artery
OSI	Oscillatory shear index
PCMRA	Phase contrast magnetic resonance angiography
PCA	Posterior cerebral artery
PComA	Posterior communicating artery
PI	Pulsatility index
PIV	Particle imaging velocimetry
PS	Peak systole
SAH	Subarachnoid hemorrhage
SD	Standard deviation
SE	Standard error
TA	Time-averaged
transWSS	Transverse wall shear stress
VA	Vertebral artery
VISC	Virtual Intracranial Stenting Challenge
VTK	Visualization Toolkit
VMTK	Vascular Modeling Toolkit
WSS	Wall shear stress
WSSG	Wall shear stress gradient

1

Introduction

1.1 Clinical context

Cerebral aneurysms are localized, pathological dilatations of cerebral arteries (Figure 1.1) [25], which are found in 2 % of the general population [159]. They often remain asymptomatic during the course of life [159], yet severe complications arise when they rupture and cause a subarachnoid hemorrhage (SAH) [83]. Although SAHs account for only 5 % of all strokes [55, 190], they are particularly devastating as they occur at a relatively young age and are often fatal [94]. Half of the patients die after aneurysm rupture, another 10 to 20 % become disabled and dependent on help [83].

Treatment strategies are aimed at excluding the aneurysm from circulation. The two common procedures are neurosurgical clipping and endovascular coiling [25]. Clipping

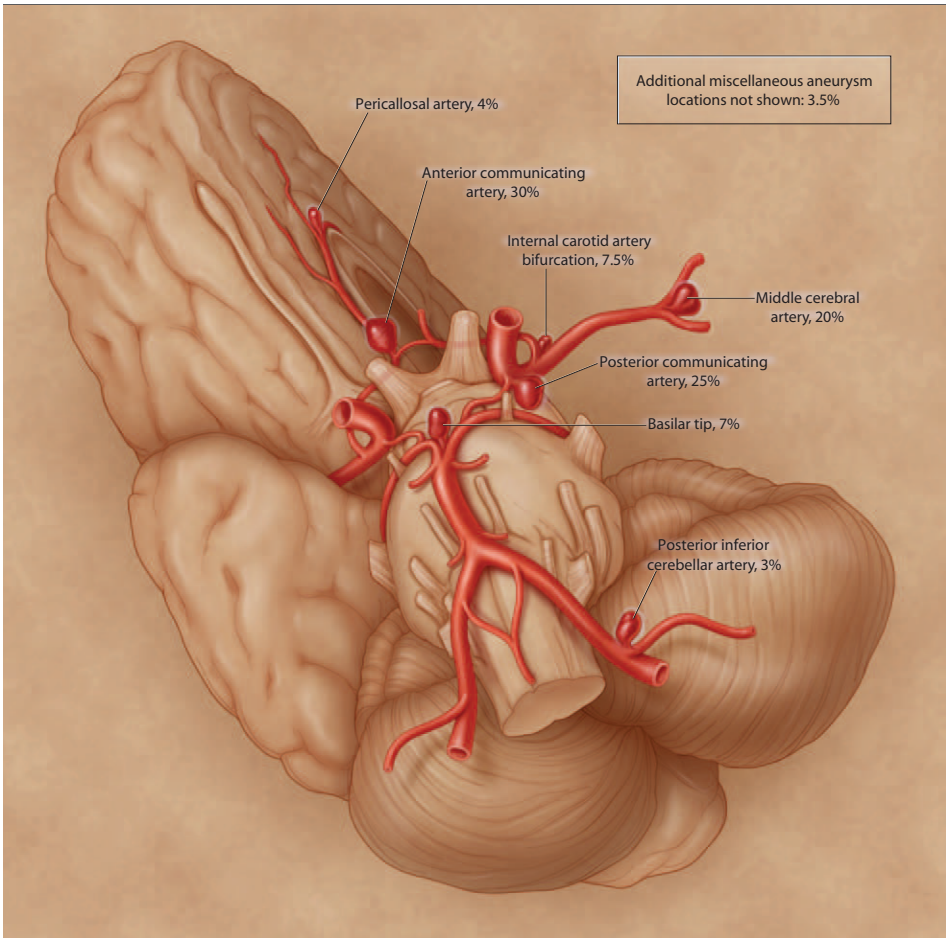

Figure 1.1: *The cerebral vasculature, showing the most frequent locations of cerebral aneurysms. Percentages indicate the incidence of aneurysms. Reproduced with permission from [25], Copyright Massachusetts Medical Society.*

involves opening the skull and placing a permanent clip across the neck of the aneurysm. Coiling involves partially filling the aneurysm with thin biocompatible metal wires to promote thrombosis. When necessary, the coils are kept in place by a stent. Both procedures come with a significant risk for the patient, clipping more so than coiling [138, 154, 194], and there is a chance of recurrence [138]. The choice of procedure depends on the location and shape of the aneurysm, and the tortuosity of the parent vessel [25]. In recent years, flow diversion has emerged as a new endovascular procedure. Flow diversion involves deploying a low-porosity stent, a so-called flow diverter, in the parent vessel to greatly reduce the blood flow into the aneurysm and, thus, promote thrombosis. It provides an alternative for wide-necked and large aneurysms for which coiling is challenging or not an option. Early clinical studies have shown promising results [124, 180], but the safety and effectiveness of the procedure remains controversial [9, 24, 27, 112, 193].

Improvements in neuroradiological imaging have led to more frequent detection of unruptured aneurysms. Unlike ruptured aneurysms, not all unruptured aneurysms need to be treated. To make a sound decision on whether and how to intervene, one should weigh the risk of treatment against the risk of rupture. In current clinical practice, several factors are considered, including aneurysm size, lobulation and location; life expectancy; family history; nicotine use; and clinical symptoms [54, 205]. These factors are well-supported by evidence, but seem to insufficiently capture the complexities of the problem at hand. Therefore, one of the major challenges in the management of aneurysms lies with the definition of accurate predictors of aneurysm rupture and treatment outcome.

In this clinical context, there are many open questions. Why do aneurysms form? Do aneurysms constitute a single disease? Why do some aneurysms stabilize after initial growth while others keep growing? How can we predict aneurysm rupture? How can we predict treatment outcome?

1.2 Importance of hemodynamics

The mechanisms underlying the initiation, growth and rupture of cerebral aneurysms remain unclear. For many years, aneurysms were believed to be congenital, but it is now well-accepted that they develop during the course of life [173]. Several systemic risk factors have been identified, including smoking, hypertension, excessive alcohol intake, female gender, and genetic predisposition [56, 98, 99, 161]. In addition, some properties of cerebral arteries, such as the lack of an external elastic lamina, seem to render them susceptible to aneurysm formation [85, 120]. However, these factors affect the whole cerebral vasculature, whereas the distribution of aneurysms suggests that also local factors are involved [143, 162]. Specifically, the majority of aneurysms are found at the apex of bifurcations or the outer wall of vascular bends, which are characterized by high hemodynamic stress [2, 3, 108, 151]. This has long established the importance of hemodynamic stress in aneurysm formation [105, 173].

Hemodynamic stress consists of pressure and wall shear stress (WSS) [48]. Due to the

pulsatile nature of blood flow, both components vary during the cardiac cycle. Pressure elicits circumferential stress in the arterial wall, causing cyclic stretching of intramural cells. WSS is the flow-induced frictional force exerted directly on the endothelial cells [125, 158, 162, 196]. Through their interaction with the arterial wall, these stresses act as mechanical stimuli of vascular biology. Under healthy circumstances, arteries can adapt to changes in hemodynamic stress and maintain homeostasis. When weakened by systemic risk factors, however, these changes may lead to the pathological growth and remodeling associated with aneurysm formation [53, 133]. Aneurysm progression is further escalated by the inflammatory response of the tissue [133, 149, 186]. This constitutes a three-way relationship: hemodynamic stress triggers vascular growth and remodeling (1), which changes the vascular geometry in an attempt to restore 'normal' wall stress and WSS (2), which in turn alters the flow field and, thus, the hemodynamic stress (3) [75, 133]. Some aneurysms stabilize by finding a balance between wall degradation and repair, while others continue to grow. Aneurysms rupture when wall stress exceeds wall strength, which is typically due to a sudden increase in blood pressure [199].

In conclusion, the pathophysiology of aneurysms depends on the interplay between multiple factors. The key role of hemodynamics among them has motivated our research on this topic.

1.3 In vivo measurement of hemodynamics

In vivo techniques are available to assess the hemodynamics in cerebral arteries. Transcranial Doppler ultrasound (TCD) measures the blood flow velocity through windows of the skull. The technique has a high temporal resolution and is noninvasive, but measurements are difficult to obtain because of the skull's anatomy and the tortuosity of arteries [163, 178]. Endovascular dual-sensor guidewires measure both velocity and pressure. The technique is invasive, but has the advantage that measurements can be performed during endovascular treatment of the aneurysm [58, 131, 163, 166]. Phase contrast magnetic resonance angiography (PCMRA) measures the 3D velocity field at different instances of the cardiac cycle. From the velocity field, additional hemodynamic variables, such as the WSS, can be derived [128]. It is the only technique that can provide an estimation of the WSS distribution, but, due to current low temporal and spatial resolutions, its accuracy is limited. As a result, only large-scale WSS features can be reliably measured [192].

Unfortunately, none of the in vivo techniques currently provide the level of detail desired to study the hemodynamics of cerebral aneurysms. Moreover, they are limited to assessing the patient's condition at the time of acquisition and do not allow for testing hypothetical conditions. The ability to explore hypothetical conditions is essential for treatment planning and for noninvasively evaluating the hemodynamics at different levels of physical activity. Fortunately, this flexibility is offered by computational modeling of hemodynamics, which forms the core of the research presented in this thesis.

1.4 Computational modeling of hemodynamics

1.4.1 Perspective

Over the last decade, computational modeling has emerged as the most important technique to study the hemodynamics in cerebral aneurysms. By combining data obtained from the patient with computational modeling, we can enhance our assessment of the patient's condition and predict the future development of the disease and the outcome of treatment. As computational power increases and model accuracy improves, we believe that this technique will one day find its way into clinical practice.

Complementing clinical measurements with computational modeling is in line with the Physiome and Virtual Physiological Human initiatives, which aim to develop an integrated framework to model the human body as a single complex system [57, 87]. To accomplish this, the model should integrate the physiological processes and their interactions across different length and time scales, scientific disciplines, and anatomical subsystems. The ultimate goal is to build a computer model of each patient, using patient-specific data and population-based information. For the population as a whole, these models can be used to better understand human physiology and to optimize treatment development. For the individual patient, these models can be used to improve diagnosis and therapeutic planning.

1.4.2 Computational fluid dynamics

Fluid dynamics is the study of the motion of fluids. Since the phenomena of interest are macroscopic, we can neglect the local movement of molecules and regard the fluid as a continuous medium. This means it can be considered a collection of infinitesimally small volume elements, whose movements are dictated by a flow field. To fully determine the flow field, we need to find an expression for velocity vector $\boldsymbol{v}$, pressure p, and density ρ as a function of space and time. These three variables can be found by solving the Navier-Stokes equations: the continuity equation, the momentum equation and the energy equation. Although blood is composed of blood cells suspended in blood plasma, on the scale of interest, it may be considered a homogenous, Newtonian, incompressible fluid with constant density. Under these assumptions, the energy equation gets uncoupled and a complete solution of the flow field can be found by merely solving the continuity and momentum equations [4, 130, 210].

The continuity equation follows from the principle of mass conservation. Under the assumption of an incompressible fluid, it simplifies to

$$\nabla \cdot \boldsymbol{v} = 0 \tag{1.1}$$

The momentum equation follows from the principle of momentum conservation. For a viscous, incompressible fluid we get

$$\rho \frac{D\boldsymbol{v}}{Dt} = \rho \boldsymbol{F} - \nabla p + \mu \nabla^2 \boldsymbol{v} \tag{1.2}$$

where D/Dt is the Lagrangian derivative, representing the time rate of change within a given fluid element as it moves through space, $\boldsymbol{F}$ combines all the forces acting on the infinitesimally small volume elements per unit mass, and μ is the viscosity.

The Navier-Stokes equations were developed halfway through the 1800s. The closely coupled equations are nonlinear in almost any situation and, therefore, hard or impossible to solve analytically in most practical situations. This problem is overcome by converting the partial differential equations into a matrix of discrete equations. They provide a solution for the velocity and pressure for each node or element of a discretized computational domain. The branch of fluid dynamics that uses numerical methods to solve the Navier-Stokes equations is known as computational fluid dynamics (CFD).

In the beginning of the 20th century, the first rudimentary numerical solutions for simple flow problems were generated, but the iterative process by which this was achieved was enormously time consuming [104, 183]. The introduction of modern computer technologies made it gradually feasible to perform numerical calculations on real flow problems within reasonable timescales. After developing algorithms and codes during the 1960s and 1970s, commercial software became available from the early 1980s. Ever since, software has been improved and the rapid increase in computational power has made it possible to find flow solutions for highly complex problems, including clinical ones. The first papers on aneurysms date from the 1980s and 1990s with simulations of 2D idealized vascular models [63, 72, 150]. In 2002, simulations of 3D image-based vascular models were introduced, which marked the beginning of an exciting new field of research [26, 38, 45, 97, 175].

1.4.3 Modeling pipeline

The modeling pipeline we used to construct hemodynamic simulations was based on the one described by Cebral et al. [34]. The steps are summarized below. More details will be provided in subsequent chapters of this thesis.

- *Medical image* Patients are imaged with different imaging modalities. Depending on the stage of the care cycle, a different trade-off is made between the invasiveness of the modality and the quality of the image. Computed tomographic angiography (CTA) and magnetic resonance angiography (MRA) are preferred for non-acute diagnosis and follow-up. Digital subtraction angiography (DSA), a 2D modality, and 3D rotational angiography (3DRA) are preferred for treatment and pre-treatment planning. The images used in our studies were either 3DRA or CTA datasets. As example, Figure 1.2 shows the cerebral vasculature of the same patient imaged with DSA, 3DRA and CTA.

- *Vascular model* Patient-specific vascular models, represented by triangular surface meshes, are constructed by segmenting the image, i.e., by finding the boundary between

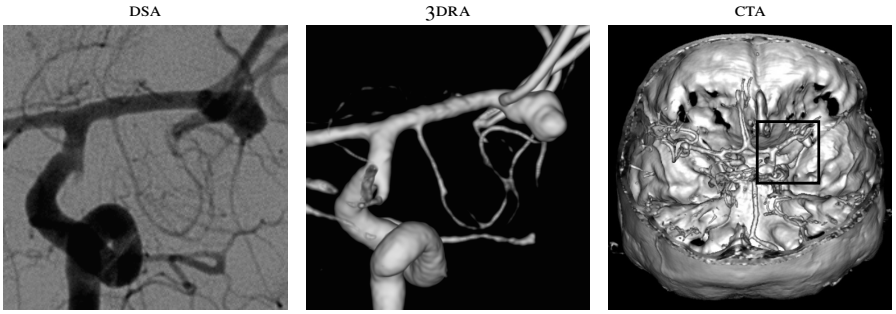

Figure 1.2: *The same patient imaged with three different imaging modalities: digital subtraction angiography (DSA), 3D rotational angiography (3DRA), and computed tomographic angiography (CTA). The DSA/3DRA's field of view is indicated in the CTA image.*

lumen and arterial wall. The simplest segmentation method is to threshold intensity values in the image, but this will likely generate inaccurate object boundaries. Instead, more advanced methods have been developed. The one in our studies was developed in-house [20, 78] and uses deformable models whose evolution is driven by minimal local curvature (internal force) and a combination of region-based information and image-gradient maps (external force). Because of limitations in image quality and segmentation, the segmentation output is typically manually post-processed to remove touching vessels and obtain a smooth surface (Figure 1.3).

- *Volumetric mesh* Based on vascular models, volumetric meshes are created to serve as computational domains for the CFD solver. In our studies, we used unstructured meshes containing tetrahedral elements in the center of the lumen and prism elements at the wall (Figure 1.3).

- *Boundary conditions* The numerical solution of the Navier-Stokes equations requires the boundary conditions of the computational domain to be specified. With this additional set of constraints as input, the CFD algorithm solves the differential equations for the complete domain. In our studies, blood was modeled as an incompressible Newtonian fluid [140]. The vessel wall was assumed to be rigid with a no-slip boundary condition [50]. Preferably, one uses patient-specific flow and pressure information as boundary condition, but this information is rarely acquired in the clinic. Instead, we imposed a 'typical' or population-averaged flow rate waveform at the inlet, scaled according to prescribed time-averaged flow rate or WSS values. Zero-pressure boundary conditions were imposed at all outlets.

- *CFD simulation* CFD simulations were created with CFX (ANSYS, Canonsburg, PA, USA), which is a commercial vertex-centered finite volume solver (Figure 1.3).

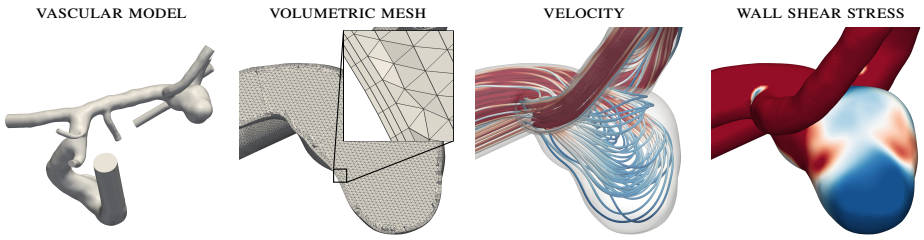

Figure 1.3: *Computer model of the patient in Figure 1.2: vascular model, volumetric mesh composed of tetrahedral and prism elements, streamlines representation of the velocity field, and contour plot of the wall shear stress magnitude.*

1.5 Aim and research questions

Computational modeling has shown great potential to help us understand the role of hemodynamics in the pathophysiology and treatment of aneurysms. Given that they rely on several assumptions, they provide an approximation of the flow field. It is thus important to evaluate their sensitivity, reproducibility and accuracy to be able to correctly interpret their output. In particular, this is crucial before they become part of clinical decision-making.

The aim of the work presented in this thesis was to identify hemodynamic factors that can be reliably computed and that can be used to study aneurysm pathophysiology. We addressed the following questions:

1. Are hemodynamic simulations reproducible across imaging modalities commonly used in clinical practice?
2. Are hemodynamic simulations reproducible across research groups?
3. Can computationally inexpensive steady flow simulations be used to answer clinically relevant questions?
4. Which reliable hemodynamic factors are associated with aneurysm initiation?

1.6 Contributions

Chapters 2 to 5 each present a study addressing one of the research questions. The chapters were adapted from published or submitted journal papers and are self-contained. In this section, we provide a brief outline of the thesis, summarizing its contributions.

- *Chapter 2* Ideally, hemodynamic simulations should be available at each stage of the patient care cycle. However, depending on the stage a different trade-off is made between the invasiveness of the modality and the quality of the image. The two most commonly used modalities are 3DRA and CTA. Compared with CTA, 3DRA produces vascular

models with superior anatomical accuracy, but its relative invasiveness restricts the use of this modality to treatment and pre-treatment planning. CTA is used for diagnosis and follow-up. In this study, we assessed the reproducibility of hemodynamic simulations across imaging modalities for a group of patients imaged with both 3DRA and CTA.
— Published in the American Journal of Neuroradiology

- *Chapter 3* Research groups use a wide range of implementations and set-ups to obtain volumetric meshes and CFD solutions. Along with extensive in-house studies, there is a need for comparing CFD solutions from different research groups for the same input data. To this end, the author of this thesis co-organized the 2011 edition of the Virtual Intracranial Stenting Challenge (VISC'11). This chapter reports on the design and findings of the challenge. The aim was to assess the reproducibility with which research groups can simulate the velocity field in a cerebral aneurysm before and after treatment with five different configurations of high-porosity stents. The velocity field of the untreated case was validated against in vitro measurements obtained with particle image velocimetry.
— Published in the Annals of Biomedical Engineering

- *Chapter 4* The majority of studies use unsteady, pulsatile flow simulations to capture the changing flow rate and inertia effects during the cardiac cycle. The enormous amount of generated data is typically reduced by extracting and analyzing the time-averaged, peak systole or end diastole flow field. In this study, we explored the possibility to approximate these flow fields with steady flow simulations. The shorter time required to create these simulations could aid the introduction of CFD into clinical practice.
— Published in the Journal of Biomechanics

- *Chapter 5* In this study, we characterized the WSS field at the aneurysm initiation site. All included aneurysms were from a single location. This location was neither a bifurcation apex nor the outer wall of a vascular bend, which – attributed to being high WSS regions – are the most common aneurysm locations. Studying locations with lesser-known hemodynamic conditions can provide great insight into the hemodynamic mechanisms underlying aneurysm initiation. Vascular geometries with the aneurysm removed were matched by controls that never formed an aneurysm at that particular location, but elsewhere.
— Prepared for submission

1.7 Conclusions

- The main flow characteristics of an aneurysm are reproduced across imaging modalities. However, substantial discrepancies are found for quantitative hemodynamic variables, such as the average WSS on the aneurysm. Therefore, one can reliably approximate and refer to only the main flow characteristics.
— Chapter 2

- Given geometry and flow rate boundary conditions, research groups can accurately simulate the velocity field inside a cerebral aneurysm and find excellent agreement on the hemodynamic effect of different stent configurations.
  — Chapter 3

- Steady flow simulations can accurately approximate the time-averaged, but not the peak systole and end diastole, WSS field of an aneurysm. The reduction in computation time, with respect to pulsatile flow simulations, could help facilitate the introduction of CFD into clinical practice.
  — Chapter 4

- Aneurysms form in regions of high WSS and high WSS gradients. They coincide with focal regions of high WSS pulsatility.
  — Chapter 5

- Time-averaged WSS distributions, not magnitudes, are largely unaffected by physiological variations in inlet flow rate. Given the lack of patient-specific flow rate boundary conditions, we recommend normalizing WSS fields to focus analysis on WSS distributions rather than magnitudes in studies associating WSS to aneurysm initiation, growth or rupture.
  — Chapter 4 and 5

1.8 Future prospects

Over the last decade, hemodynamic modeling of cerebral aneurysms has become a vivid field of research. Thanks to the potential of computational modeling in medicine and the wide-spread availability of CFD as a technique, the field has grown tremendously. In this section, we wish to provide our vision for possible future directions:

- The overestimation of aneurysm neck size by 3DRA, in comparison to higher-resolution DSA, was recently shown to have non-negligible consequences for the simulated hemodynamics [164]. Further advancements in image quality and segmentation algorithms are needed to obtain more accurate vascular models and, thus, more accurate hemodynamic simulations.

- Studies associating hemodynamic factors to aneurysm initiation or rupture make strong assumptions regarding the vascular geometry. Aneurysm rupture might affect the aneurysm geometry and aneurysm formation might affect the parent vessel geometry [165, 168]. Large prospective studies are needed.

- The lack of patient-specific boundary conditions is a huge limitation of current hemodynamic modeling [92, 102, 129, 131, 163]. Perhaps even more so than with improving the accuracy of vascular models, which will occur at the ‘periphery’ of our field through

advances in imaging and segmentation, hemodynamic modelers should play an active role in retrieving flow and pressure information from the patient. Moreover, rather than using a single set of boundary conditions, stochastic simulation techniques could be employed to obtain a space of possible CFD solutions and account for the great variability observed under different levels of physical activity [47].

- Hemodynamic modeling is commonly restricted to assessing only a portion of the cerebral vasculature. In the vein of the VPH initiative, multiscale modeling could be achieved by coupling the 3D model to lumped parameter and/or 1D models [18, 145]. This would allow us to evaluate how changes elsewhere in the circulation affect the region-of-interest.

- Hemodynamics is only one aspect of the mechanisms underlying aneurysm pathophysiology. It is therefore important to investigate its interaction with vascular biology by complementing histological analyses with hemodynamic modeling [53, 134, 135] and developing fluid-solid-growth models of cerebral aneurysms [1, 84, 200, 201].

2

Reproducibility of hemodynamic simulations across imaging modalities 3DRA and CTA

Abstract — Patient-specific simulations of the hemodynamics in cerebral aneurysms can be constructed by using image-based vascular models and computational fluid dynamics (CFD) techniques. This work evaluates the impact of the choice of imaging technique on these simulations. Ten aneurysms, imaged with three-dimensional rotational angiography (3DRA) and computed tomographic angiography (CTA), were analyzed to assess the reproducibility of geometric and hemodynamic variables across the two modalities. Compared with 3DRA models, we found that CTA models often had larger aneurysm necks ($p = 0.05$) and that most of the smallest vessels (between 0.7 and 1.0 mm) could not be reconstructed successfully with CTA. With respect to the values measured in the 3DRA models, the flow rate differed by 14.1 ± 2.8 % (mean ± standard error) just proximal to the aneurysm and 33.9 ± 7.6 % at the aneurysm neck. The mean wall shear stress (WSS) on the aneurysm differed by 44.2 ± 6.0 %. Even when normalized to the parent vessel WSS, a difference of 31.4 ± 9.9 % remained, with the normalized WSS in most cases being larger in the CTA model ($p = 0.04$). Despite these substantial differences, excellent agreement ($\kappa \geq 0.9$) was found for qualitative variables that describe the flow field, such as the structure of the flow pattern and the flow complexity. We therefore conclude that although relatively large differences were found for all evaluated quantitative hemodynamic variables, the main flow characteristics were reproduced across imaging modalities.

Adapted from: Geers AJ, Larrabide I, Radaelli AG, Bogunovic H, Kim M, Gratama van Andel HAF, Majoie CB, VanBavel E, Frangi AF. *Patient-specific computational hemodynamics of intracranial aneurysms from 3D rotational angiography and CT angiography: an in vivo reproducibility study.* American Journal of Neuroradiology, 32(3): 581–586, 2011

2.1 Introduction

Degradative biological processes in the arterial wall that lead to growth and rupture of cerebral aneurysms [65] have been related to intra-aneurysmal hemodynamics [72, 75, 105]. Computational fluid dynamics (CFD) simulations have been used to gain insight into the patient-specific hemodynamics and could potentially assist rupture-risk assessment [30, 31, 35, 37, 95] and treatment planning [39, 44, 101, 106, 115, 123, 155].

Vascular models can be constructed through segmentation of three-dimensional rotational angiography (3DRA) and computed tomographic angiography (CTA) images. Compared with CTA, 3DRA produces images with higher contrast, higher spatial resolution, and lower visibility of bone [7, 177, 204], which lead to better segmentation results [78] and superior anatomic accuracy [153, 181, 195]. However, acquisition of 3DRA images involves the introduction of a catheter into the cerebral vasculature to locally inject contrast agent, making it more invasive than CTA, which involves contrast injection in a peripheral vein [49, 206]. As a result of this trade-off, 3DRA is often used before and during treatment, whereas CTA is often used for diagnosis and follow-up studies [25].

To the best of our knowledge, the reproducibility of hemodynamic simulations based on in vivo images from different modalities is yet unknown. Previous studies did show that among all input parameters of the modeling pipeline, the vascular geometry has the greatest impact on its output [34, 184]. Because the choice of imaging technique may affect the vascular geometry, it could give rise to differences in hemodynamic predictions. To investigate this issue, we conducted a study comparing simulations with 3DRA- and CTA-based vascular models of 10 aneurysms.

2.2 Methods

2.2.1 Patient population

Clinical data were obtained at the Department of Radiology of the Academic Medical Center in Amsterdam, the Netherlands, for a study including 108 patients imaged with both 3DRA and CTA within a three-day interval [160]. Approval from the institutional review board was obtained for review of anonymized medical records and images. As part of this study, the quality of CTA images was rated by two experienced clinicians. From a subgroup of 80 patients with the highest quality images, 4 patients with 10 aneurysms were randomly chosen for our study (Table 2.1).

2.2.2 Imaging protocols

3DRA images were acquired with a single-plane angiographic unit (Integris Allura Neuro; Philips Healthcare, Best, the Netherlands). Nonionic contrast agent (320 mg I/ml of iodixanol, Visipaque; GE Healthcare, Cork, Ireland) was injected through a 6F catheter positioned in the internal carotid artery (ICA) or vertebral artery (VA). One hundred images

Table 2.1: *Clinical information of the patient population.*

Patient			Aneurysm			
No.	Sex	Age [yr]	No.	Side	Location[a]	Rupture
1	F	45	1	Right	MCA bifurcation	Y
			2	Left	MCA bifurcation	N
2	F	74	3	Left	ICA	Y
3	F	37	4	Right	MCA	N
			5	Right	MCA	N
			6	Right	MCA bifurcation	N
4	F	43	7	Left	MCA	N
			8	Right	MCA	N
			9	Right	MCA bifurcation	Y
			10	Middle	BA terminus	N

[a] MCA = middle cerebral artery; ICA = internal carotid artery; BA = basilar artery.

were acquired during a 240° rotational run in 8 seconds with 15 to 21 ml of contrast agent at 3 ml/s. A 3D image of the region of interest was reconstructed with a $256 \times 256 \times 256$ matrix on a dedicated workstation.

CTA images were acquired with a 4-section spiral CT scanner (Somatom, Sensation 4; Siemens, Erlangen, Germany). 80 to 100 ml of nonionic contrast agent (320 mg I/ml of iodixanol, Visipaque) was injected in a cubital vein at a rate of 4 ml/s. Scanning delay was automatically adjusted by a bolus-tracking technique. Parameters were set as follows: 120 kV, 250 mA s, 4 mm × 1 mm detector collimation, pitch of 0.875, section thickness of 1.3 mm, increment of 0.5 mm, 512×512 matrix, H30f reconstruction kernel [160].

2.2.3 Vascular modeling

Patient-specific vascular models were constructed from the image datasets by using a completely automatic geodesic active regions segmentation algorithm [78]. This approach drives the evolution of geometric deformable models toward the vascular boundaries by taken into account the minimal local curvature (internal force) and a combination of region-based information and image-gradient maps (external force). Region-based information is used to initialize the model and prevents the leakage of the evolving front when the image gradient is weak. The accuracy of the segmentation algorithm was recently investigated for both 3DRA and CTA [78]. In a study of 10 clinical datasets, the technique compared favorably with other techniques, showing a high overlap with respect to the ground truth (91.13 % and 73.31 % for 3DRA and CTA, respectively) and an error distance to the ground truth close to the in-plane resolution (0.40 and 0.38 mm, respectively).

The segmentation process outputs a surface mesh representing the vascular boundaries. Subsequently, postprocessing operations were applied manually to separate touching vessels, extrude poorly segmented in- and outlets, smooth the surface, and improve the mesh quality. Operations were executed with ReMESH, Version 2.0 (IMATI-GE/CNR, Genova, Italy) [10].

In the rest of this chapter, we will refer to vascular models obtained from 3DRA or CTA images and their corresponding CFD simulations as 3DRA and CTA models, respectively.

2.2.4 Blood flow modeling

Unstructured meshes containing tetrahedral and prismatic elements were created with ICEM CFD, v11.0 (ANSYS, Canonsburg, Pennsylvania). Element sizes ranged between 0.1 and 0.2 mm, with smaller elements in high curvature regions. Three prismatic boundary layers with a total thickness of approximately 0.15 mm covered the vessel wall to locally ensure an accurate definition of the velocity gradient. On average, meshes consisted of 0.4 million nodes and 1.5 million elements.

Transient CFD simulations were created with CFX, v11.0 (ANSYS), which uses a finite volume approach to solve the Navier-Stokes equations. Blood was modeled as an incompressible Newtonian fluid with density $\rho = 1060\,\mathrm{kg/m^3}$ and viscosity $\mu = 4\,\mathrm{mPa\,s}$). The vessel wall was assumed to be rigid with a no-slip boundary condition. A straight inlet extension was added to the image-based vasculature, and a parabolic velocity profile was imposed at the inlet of the extension. Because patient-specific flow information was not available, a flow rate waveform from a healthy volunteer acquired with phase-contrast magnetic resonance imaging described the pulsatile flow conditions at the inlet. This waveform was scaled to obtain a physiologically realistic mean wall shear stress (WSS) of 1.5 Pa near the inlet of the 3DRA model [158]. To prevent hemodynamic discrepancies further downstream due to a difference in inflow conditions, we chose an equal inflow rate for the corresponding CTA model. We will elaborate on this modeling choice in Section 2.4. Traction-free boundary conditions were prescribed at all outlets. Time steps were chosen to be 3 ms around peak systole, where the time-derivative of the flow rate is relatively large, and 20 ms elsewhere. To reduce initial transients, we computed two complete cardiac cycles and data of the second cardiac cycle were stored and analyzed.

2.2.5 Data analysis

Quantitative geometric and hemodynamic variables were measured in both models. Unless otherwise stated, the time-averaged flow field was analyzed. The aneurysm neck area (A_N) and the volume of the aneurysm (V_A) were measured to quantify features of the aneurysm geometry. The distribution of flow was described by measuring the flow rate in the parent vessel just proximal to the aneurysm (Q_P), the flow rate into the aneurysm (Q_A), and their ratio to normalize the flow rate into the aneurysm (NQ_A). The WSS plays an important role in the development of aneurysms [75]. We therefore measured the mean WSS on a segment of the parent vessel just proximal to the aneurysm (WSS_P), the mean WSS on the aneurysm wall (WSS_A), and their ratio to normalize the WSS on the aneurysm wall ($NWSS_A$). Normalized measurements were included to differentiate discrepancies in hemodynamic patterns from scaling of hemodynamic variables as a result of differences in vessel size and differences in flow divisions at proximal bifurcations. Furthermore, we

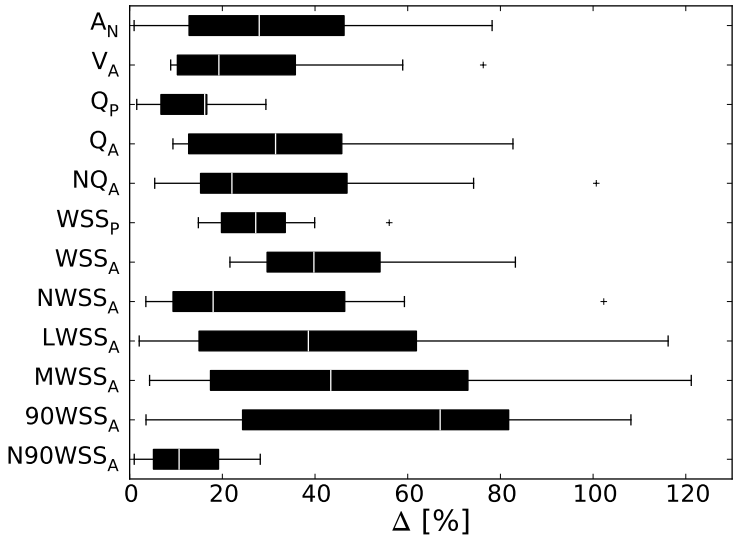

Figure 2.1: *Boxplot showing the distribution of differences* Δ *for each geometric and hemodynamic variable among the 10 aneurysms.* Δ *is defined as the relative difference between the two models with respect to the 3DRA model. Outliers, marked with an asterisk, are defined as data points that are* > 1.5 *times the interquartile range above the upper or below the lower quartile. See variable definitions in Section 2.2.5.*

evaluated two WSS-derived quantitative variables that have been associated with a clinical history of rupture: the portion of aneurysm wall under low WSS (< 0.4 Pa) at end diastole ($LWSS_A$) [95] and the maximum WSS on the aneurysm wall at peak systole ($MWSS_A$) [30, 31]. In addition to the latter, two other measures of high WSS were evaluated: the 90th percentile value of the WSS on the aneurysm at peak systole ($90WSS_A$) and this percentile normalized by the mean WSS on the aneurysm at peak systole ($N90WSS_A$).

For each variable, the relative difference between the two models with respect to the 3DRA model (Δ) was determined. The mean and standard error (SE) of this difference over all 10 cases were calculated. The Wilcoxon signed-rank test was used to test the significance of the differences between the two models. Differences were considered statistically significant for $p \leq 0.05$.

The intra-aneurysmal flow field was characterized using qualitative variables that have been proposed by Castro et al. [31] and Cebral et al. [35], namely the location and size of the impingement region on the aneurysm wall; the size of the inflow jet in the aneurysm; and the flow complexity, stability, and pattern type in the aneurysm. Data were obtained by two independent observers through inspection of streamlines color-coded with the magnitude of the velocity and color maps of the WSS and the oscillatory shear index (OSI). The OSI describes the oscillatory nature of the WSS during the cardiac cycle with 0.0 and 0.5 representing minimum and maximum oscillation, respectively [111]. The hemodynamic results were examined for the flow field at end diastole and peak systole

Table 2.2: *Differences in geometry and hemodynamics for all aneurysms.*

		Δ^c	
Variable[a]	p-value[b]	Mean [%]	SE [%]
A_N [mm^2]	0.05	33.0	8.3
V_A [mm^3]	0.38	27.8	7.4
Q_P [ml/s]	0.85	14.1	2.8
Q_A [ml/s]	0.38	33.9	7.6
NQ_A [-]	0.63	35.9	9.8
WSS_P [Pa]	0.28	28.6	4.0
WSS_A [Pa]	0.43	44.2	6.0
$NWSS_A$ [-]	0.04	31.4	9.9
$LWSS_A$ [%]	0.11	13.7	4.0
$MWSS_A$ [Pa]	0.85	47.9	11.9
$90WSS_A$ [Pa]	0.28	56.5	11.7
$N90WSS_A$ [-]	0.85	12.6	3.1

[a] See variable definitions in Section 2.2.5.
[b] p-values were calculated with the Wilcoxon signed-rank test.
[c] Δ is defined as the relative difference between the two models with respect to the 3DRA model; SE = standard error.

and for the time-averaged flow field. Agreement between the two imaging modalities and agreement between the two observers were tested with free-marginal statistics [22]. Agreement was categorized as poor ($\kappa < 0.20$), fair ($0.20 < \kappa < 0.40$), moderate ($0.40 < \kappa < 0.60$), good ($0.60 < \kappa < 0.80$), or excellent ($\kappa \geq 0.80$).

2.3 Results

2.3.1 Main observations

The flow rate in the parent vessel, measured just proximal to the aneurysm, differed by 14.1 ± 2.8 % (mean $\pm$ SE) due to geometric differences in proximal bifurcations that affected their flow splits (Table 2.2). In some cases, bifurcations to smaller vessels, such as the ophthalmic artery or the anterior choroidal artery, were missing in the CTA model but were successfully reconstructed in the 3DRA model. Naturally, these variations gave rise to differences in the flow split. Most of the missing small vessels were < 1 mm in diameter (measured in the 3DRA model), whereas the smallest vessels in 3DRA models were approximately 0.7 mm in diameter. The segmentation algorithm failed to preserve these vessels due to the lower spatial resolution of CTA and the presence of bone tissue near vascular structures.

The lower spatial resolution of CTA also made it difficult for the segmentation algorithm to distinguish vascular structures that were in close proximity to each other. As a result, the aneurysm neck was significantly wider in CTA models ($\Delta = 33.0 \pm 8.3$ %, $p = 0.05$). This affected the flow split at the aneurysm neck, which was reflected in a

Table 2.3: *Intermodality and interobserver agreement for qualitative hemodynamic variables.*

		κ_{modality}		κ_{observer}	
Variable	No. of categories	κ^{a}	Agreement	κ^{a}	Agreement
Impingement location	3	0.95	Excellent	0.76	Good
Impingment region size	2	1.00	Excellent	1.00	Excellent
Jet size	2	1.00	Excellent	1.00	Excellent
Flow complexity	2	0.90	Excellent	1.00	Excellent
Flow stability	2	0.90	Excellent	0.81	Excellent
Flow pattern type	3	0.95	Excellent	0.76	Good

[a] κ is the free-marginal κ coefficient to measure interrater agreement.

$35.9 \pm 9.8\,\%$ difference in the normalized inflow into the aneurysm. The difference in mean WSS on the aneurysm wall was relatively large ($\Delta = 44.2 \pm 6.0\,\%$, $p = 0.43$). However, the difference slightly decreased after normalization, and this variable was found to be significantly higher in CTA models ($\Delta = 31.4 \pm 9.9\,\%$, $p = 0.04$). Regarding the two variables that have been associated with rupture, the differences were relatively large for the maximum WSS on the aneurysm wall at peak systole ($\Delta = 47.9 \pm 11.9\,\%$, $p = 0.85$) and relatively small for the portion of aneurysm wall under low WSS ($< 0.4\,\text{Pa}$) at end diastole ($\Delta = 13.7 \pm 4.0\,\%$, $p = 0.11$). As an alternative to quantify high WSS on the aneurysm, N90WSS gave relatively small differences between both modalities ($\Delta = 12.6 \pm 4.0\,\%$, $p = 0.85$).

Overall, differences in geometric and hemodynamic variables appeared to be relatively large and varied considerably from one aneurysm to another (Figure 2.1). However, the main blood flow characteristics were often the same for the 3DRA and CTA models. Excellent agreement was found between the 3DRA and CTA models for all evaluated qualitative variables (κ-values ranging from 0.9 to 1.0) with the interobserver variability being slightly higher (κ-values ranging from 0.8 to 1.0) (Table 2.3). We qualitatively assessed the OSI distributions to be moderately similar; although corresponding regions of high OSI could often be recognized, there were clear differences in more detailed features.

2.3.2 Representative cases

To shed more light on the output of our experiments and to better understand the relationship between geometric and hemodynamic differences, we present four representative cases for further discussion. Numerical data are provided in Table 2.4 and visualizations of the hemodynamic simulations are presented in Figure 2.2.

Aneurysm 1 was located at the middle cerebral artery (MCA) bifurcation and had ruptured before image acquisition. The flow rate in the parent vessel and the inflow into the aneurysm were similar (16.1 % and 9.9 % higher in the CTA model, respectively). Also, agreement was found for all studied qualitative variables. The mean WSS on the aneurysm wall was 61.9 % larger in the CTA model. After normalization by the WSS on the parent vessel wall, this difference was 20.2 %.

Table 2.4: *Differences in geometry and hemodynamics for the four selected aneurysms.*

	Aneurysm 1		Aneurysm 6		Aneurysm 9		Aneurysm 10	
Variable[a]	3DRA	CTA	3DRA	CTA	3DRA	CTA	3DRA	CTA
A_N [mm^2]	10.87	11.16	5.40	7.86	7.33	12.17	12.15	12.26
V_A [mm^3]	99.97	90.72	36.35	50.72	63.43	69.04	17.74	20.11
Q_P [ml/s]	0.80	0.93	1.31	0.99	0.76	0.89	0.43	0.45
Q_A [ml/s]	0.25	0.27	0.31	0.28	0.32	0.42	0.14	0.12
NQ_A [-]	0.31	0.29	0.24	0.28	0.42	0.48	0.33	0.27
WSS_P [Pa]	2.33	3.14	6.34	2.79	3.93	4.51	1.01	0.79
WSS_A [Pa]	0.29	0.48	1.68	0.81	0.98	1.51	0.33	0.23
$NWSS_A$ [-]	0.13	0.15	0.26	0.29	0.25	0.33	0.33	0.30
$LWSS_A$ [%]	98.41	96.52	75.32	86.81	79.60	67.04	99.11	99.84
$MWSS_A$ [Pa]	26.34	39.74	89.55	44.69	42.10	43.91	5.44	3.62
$90WSS_A$ [Pa]	1.35	2.45	5.87	2.24	4.85	8.35	0.43	0.41
$N90WSS_A$ [-]	2.53	1.82	2.26	2.24	2.20	2.30	1.61	1.93

[a] See variable definitions in Section 2.2.5.

Aneurysm 6 was located at the MCA bifurcation and was unruptured at the moment of image acquisition. Compared with the other nine cases, the 24.5 % lower flow rate in the parent vessel of the CTA model was a relatively large difference. By measuring the outflow through all outlets, two explanations could be identified: First, the geometric difference in the bifurcation from the ICA to the anterior cerebral artery (ACA) and MCA led to a larger outflow through the ACA in the CTA model. Second, the outflow through the branching vessels near the two proximal aneurysms was relatively much larger. Aneurysm 6 had a more complex flow pattern in the 3DRA model. It appears that the aneurysm shape in this model was more bottle-necked than that in the CTA model, which disrupted the inflow and created a high WSS area at the neck. When reviewing the evolution of the WSS distribution over the cardiac cycle, the 3DRA model clearly showed a shift of the impingement region on the aneurysm wall, whereas the impingement region in the CTA model was static. This instability of flow in the 3DRA model was also apparent from the large region on the aneurysm wall with high OSI values.

Aneurysm 9 was located on the MCA bifurcation and had ruptured before image acquisition. In the CTA model, the flow rate into the aneurysm was 34.2 % larger and the mean WSS on the aneurysm wall was 54.8 % larger. Geometrically, the main difference between the two models was the 66.0 % larger aneurysm neck area in the CTA model. This effectively led to the partial elimination of a bulge at the distal end of the neck, which was apparent in the 3DRA model. After the split at the aneurysm neck, the main flow jet detached from the aneurysm wall and created a second impingement region farther up the aneurysm sac. As a result, the bulge formed a relatively large region of low flow and low WSS. Due to the partial elimination of the bulge, this low-flow region was much less pronounced in the CTA model.

Aneurysm 10 was located on the basilar artery (BA) terminus and was unruptured at the moment of image acquisition. We found relatively small differences of < 35 % for

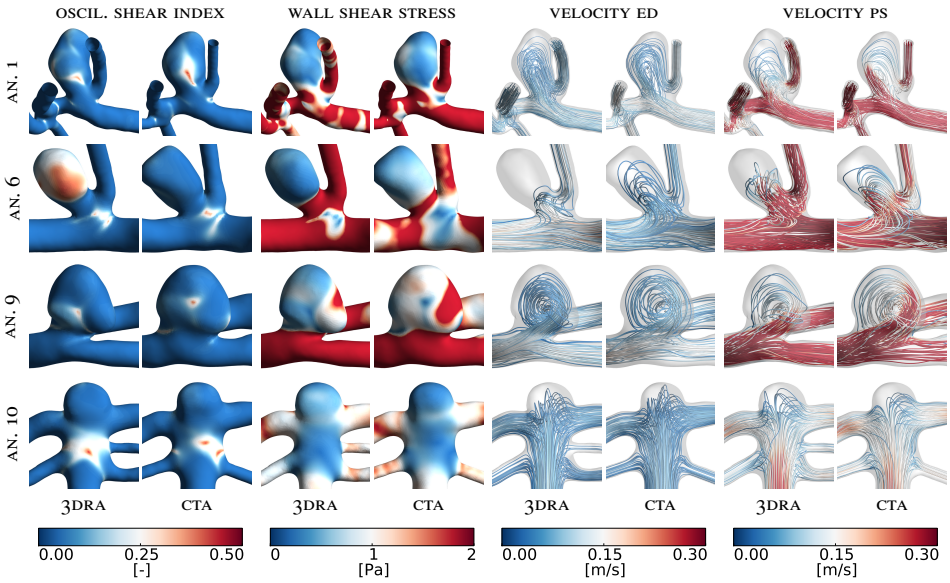

Figure 2.2: *Visualizations of hemodynamic simulations for cases 1, 6, 9, and 10. The view was chosen to most clearly present the main hemodynamic features. Displayed are streamlines color-coded with the velocity magnitude representing the flow fields at end diastole (ED) and peak systole (PS), the time-averaged WSS magnitude, and the OSI.*

all quantitative hemodynamic variables. For all qualitative hemodynamic variables, both observers found agreement between the two models. We did recognize an imaging artifact previously reported by Jou et al. [96], which led to a flattened top of the aneurysm in the 3DRA image and, hence, in the 3DRA model. However, besides a slight disruption in the curve of the main flow jet at the aneurysm top, which slightly increased the WSS magnitude at that location, no major hemodynamic differences were observed between the two models.

2.4 Discussion

The purpose of this study was to assess the impact of the imaging technique on image-based computational hemodynamic simulations of cerebral aneurysms. To this end, we conducted a study comparing simulations with 3DRA- and CTA-based vascular models of 10 aneurysms. Although relatively large discrepancies exceeding normal physiologic variation [21] were found between 3DRA and CTA models for quantitative hemodynamic variables, the visual categorization of flow characteristics was mostly reproduced across modalities and observers.

2.4.1 Main sensitivities of hemodynamic simulations

Hemodynamic simulations are believed to be sensitive to the geometry of image-based vascular models [34, 184], which in turn depends on a number of aspects, including the imaging technique, image quality, segmentation algorithm, and manual postprocessing of surface meshes. To investigate the sensitivity of hemodynamic simulations to the latter, Cebral et al. [34] let three modelers each reconstruct vascular models of four aneurysms and compared the computed hemodynamics. With results similar to those of our current study, they found that the differences in geometry did not alter the main flow characteristics in most cases. In the same work, they reported that small vessels branching off the parent vessel did not cause substantial differences in the intra-aneurysmal flow patterns, and Dempere-Marco et al. [50] came to the same conclusion after comparing rigid and nonrigid wall conditions. However, as demonstrated by Castro et al. [28], including an anatomically realistic parent vessel in the vascular model instead of a straight extrusion did prove essential to reproduce the main flow characteristics.

Besides the vascular geometry, the impact of the flow rate waveform has also received much attention [21, 34, 80, 93, 197]. Hoi et al. [81] found differences in ICA and VA waveform shapes between young and older adults, but concluded on the basis of a CFD study [80] of the carotid bifurcation that the computed hemodynamics are relatively robust to the assumed waveform shape in comparison with assumptions made on the time-averaged flow rate, and especially in comparison with geometry-related uncertainties. Venugopal et al. [197] similarly stressed the relative importance of the assumed flow rate and the outflow ratios in comparison with the assumed heart rate. Other studies evaluated the intra-aneurysmal hemodynamics during rest and exercise conditions, which essentially combined the change in waveform shape, flow rate, and heart rate. Bowker et al. [21] found that the overall flow patterns did not significantly change with a heart rate increase from 70 to 121 beats per minute and a flow rate increase of 8 %. However, Jiang and Strother [93] increased the heart rate from 60 to 150 beats per minute and the flow rate 21 % and reported that the overall flow patterns did change significantly. Both studies observed large variations in hemodynamic changes for different aneurysm geometries, which raises the interesting question of whether hemodynamic differences between 3DRA and CTA models would change under exercise conditions. The results presented in the current work are based on rest flow conditions, and caution is warranted with generalizations across physiologic conditions. Future investigation may provide additional value by comparing 3DRA and CTA models for exercise flow conditions.

2.4.2 Hemodynamic variables for rupture risk assessment

To describe the main flow characteristics, Castro et al. [31] introduced and studied qualitative hemodynamic variables. In a database of 62 cases, these authors found that ruptured aneurysms had complex unstable flow patterns, small impingement regions, and small inflow jet sizes, whereas unruptured aneurysms had simple stable flow patterns, large

impingement regions, and large inflow jet sizes. Our study showed that these variables are mostly independent of the choice for 3DRA or CTA for construction of the vascular model. We, therefore, suggest that CTA might suffice for risk assessment based on predicted hemodynamics.

As part of the present study, we compared quantitative variables that have been correlated to aneurysm rupture to illustrate the potential variability due to the choice of imaging technique. Jou et al. [95] studied 26 aneurysms at the ICA and observed that the portion of the aneurysm dome with a WSS lower than 0.4 Pa at end diastole was significantly higher in ruptured aneurysms. We evaluated this variable for our 10 aneurysms and found a 13.7 % difference between the 3DRA and CTA models ($\Delta = 13.7 \pm 4.0$ %, $p = 0.11$). Castro et al. [31] studied 26 aneurysms at the anterior communicating artery and observed that the maximum WSS on the aneurysm at peak systole was significantly higher in ruptured aneurysms. We found a 47.9 % difference between the 3DRA and CTA models ($\Delta = 47.9 \pm 11.9$ %, $p = 0.85$). As an alternative measure of high WSS, we proposed the 90th percentile value of the WSS normalized by the mean WSS on the aneurysm at peak systole, which had a higher reproducibility ($\Delta = 12.6 \pm 4.0$ %, $p = 0.85$).

2.4.3 Inlet flow rate

To prevent the difference in the inflow rate propagating to the intra-aneurysmal hemodynamics, we chose to impose the same inflow rate on the 3DRA and the CTA models. Because patient-specific data were unavailable, the inflow rate was estimated on the basis of the inlet diameter so that the WSS near the inlet was 1.5 Pa. Inlets of cerebral vascular models are usually located on either the ICA or the VA, which both run through the skull base. For 3DRA segmentation, proximity of vasculature to bone poses no difficulty. However, in CTA images, the intensity values of bone and contrast agent overlap; this overlap makes it challenging for the algorithm to segment near-bone vasculature. As a result, CTA models are anatomically less accurate in the lower parts of the ICA and VA [78] and, therefore, should not be used to estimate the inflow rate. In our study, we found that the inlet area of the CTA model was, in 8 of 10 cases, smaller ($\Delta = 20.0 \pm 3.5$ %, $p = 0.11$), which would lead to a significantly smaller inflow rate ($\Delta = 29.3 \pm 5.2$ %, $p = 0.05$). Instead, we chose to obtain a physiologic estimation of the inflow rate on the basis of the 3DRA model and used the same value for both models.

2.4.4 Advances in medical imaging

In this study, a 4-section CT scanner was used to acquire the CTA data. However, the development of CT scanners is advancing rapidly and 16-, 64-, or even 320-section CT scanners are widespread or will become available soon. With the increasing number of detector rows, larger volumes are covered in a single rotation and scanning times are reduced. Also, the use of thinner sections leads to a higher out-of-plane resolution. However, the in-plane spatial resolution mainly depends on the detector geometry and the convolution

kernel and is not substantially improved in 16- or 64-section CTA [122]. Although some increase in anatomic accuracy has been found [132], the minimal improvement in spatial resolution will not substantially resolve the issues brought forward in this study, such as the omission of small vessels, the widening of the aneurysm neck, and the bone-related segmentation issues.

2.5 Conclusions

The purpose of this study was to assess the impact of the imaging technique on image-based computational hemodynamic simulations of intracranial aneurysms. We addressed this by conducting a study comparing simulations with 3DRA- and CTA-based vascular models of 10 aneurysms. Differences in quantitative hemodynamic variables were relatively large, with mean values varying from 14.1 % for the flow rate in the parent vessel to 44.2 % for the mean WSS on the aneurysm sac. However, for qualitative variables such as the flow pattern and the flow complexity, we found excellent agreement ($\kappa \geq 0.9$) between both imaging modalities. Although hemodynamic simulations should ideally be available to clinicians at all stages of the patient care cycle and across all imaging modalities, currently one can reliably approximate and refer to only the main flow characteristics.

3

Accuracy of hemodynamic simulations and reproducibility across research groups

Abstract — This chapter reports on the 2011 edition of the Virtual Intracranial Stenting Challenge (VISC). The challenge aimed to assess the reproducibility with which research groups can simulate the velocity field in a cerebral aneurysm, both untreated and treated with five different configurations of high-porosity stents. Particle imaging velocimetry (PIV) measurements were obtained to validate the untreated velocity field. Six participants, totalling three CFD solvers, were provided with surface meshes of the vascular geometry and the deployed stent geometries, and flow rate boundary conditions for all inlets and outlets. As output, they were invited to submit an abstract to the 8th International Interdisciplinary Cerebrovascular Symposium 2011 (ICS'11), outlining their methods and giving their interpretation of the performance of each stent configuration. After the challenge, all CFD solutions were collected and analyzed. To quantitatively analyze the data, we calculated the root-mean-square error over uniformly distributed nodes on a plane slicing the main flow jet along its axis and normalized it with the maximum velocity on the slice of the untreated case (NRME). Good agreement was found between CFD and PIV with a NRME of 7.28 %. Excellent agreement was found between CFD solutions, both untreated and treated, with an average NRME of 0.47 % (range: 0.28 to 1.03 %). In conclusion, given geometry and flow rates, research groups can accurately simulate the velocity field inside a cerebral aneurysm – as assessed by comparison with in vitro measurements – and find excellent agreement on the hemodynamic effect of different stent configurations.

Adapted from: Cito S, Geers AJ, Arroyo MP, Palero VR, Pallarés J, Vernet A, Blasco J, San Román L, Fu W, Qiao A, Janiga G, Miura Y, Ohta M, Mendina M, Usera G, Frangi AF. *Accuracy and reproducibility of patient-specific hemodynamic models of stented intracranial aneurysms: Report on the Virtual Intracranial Stenting Challenge 2011.* Annals of Biomedical Engineering. [Published online ahead of print]

3.1 Introduction

Hemodynamics plays an important role in the growth and rupture of cerebral aneurysms. Better understanding of this role could lead to improved diagnosis and treatment [136]. For over a decade, the hemodynamics in anatomically realistic aneurysms has been studied using computational fluid dynamics (CFD) [167]. Besides investigating associations between hemodynamics and aneurysmal growth and rupture, much attention has been given to quantifying the change in hemodynamics after endovascular treatment with coils [13, 101, 140], high-porosity stents [14, 106, 110], or low-porosity stents (also known as flow diverters) [12, 40, 114].

Sensitivity and validation studies are prerequisites for CFD simulations to be accepted as part of clinical decision-making [176]. Along with extensive in-house studies, there is a need for comparing CFD solutions from different research groups for the same input data. Since 2006, the yearly Virtual Intracranial Stenting Challenge (VISC) has been a unique platform evaluating the inter-group reproducibility of hemodynamic simulations of stented aneurysms. Results of the 2007 edition were reported by Radaelli et al. [155] and the aneurysm used in this edition has since served as a standard test case in our research community [32, 66, 169]. Radaelli et al. found that the six participating research groups, employing a range of mesh generation and CFD simulation techniques, all consistently quantified the change in an aneurysmal velocity field after virtual deployment of three different stents.

This chapter reports on the results of the 2011 edition of VISC in which six research groups, totaling three CFD solvers, participated. The aim of the challenge was to assess the reproducibility with which research groups can simulate the velocity field in a cerebral aneurysm before and after treatment with five different configurations of high-porosity stents. The main objectives were to: 1. validate the velocity field of the untreated case against in vitro measurements, 2. quantify the reproducibility between groups for both untreated and treated cases, and 3. compare the groups' independent interpretations of the performance of each stent configuration. Our study extends the evaluation performed in VISC'07 by including a wider variety of stent treatments, validating CFD results against experimental data, and performing a more thorough quantitative data analysis.

3.2 Methods

3.2.1 Vascular geometry

The subject of the challenge was an aneurysm located at the anterior communicating artery (ACoA) (Figure 3.1). As part of a previous study by Palero et al. [144], a life-size borosilicate glass model of this aneurysm and its surrounding vasculature had been manually constructed on the basis of a three-dimensional rotational angiography (3DRA) image. The model included the A1 and A2 segments of the left and right anterior cerebral

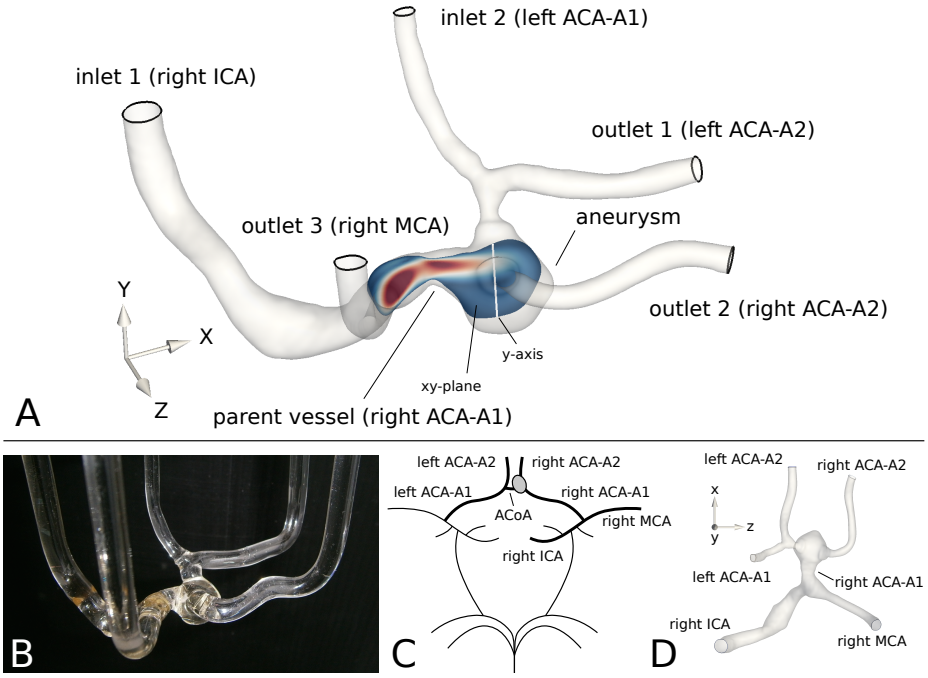

Figure 3.1: *Vascular geometry with an aneurysm located at the ACoA. (A) Surface mesh representation of the vascular geometry sliced by the xy-plane and the y-axis. The xy-plane corresponded to the laser sheet plane used during PIV acquisition. (B) Glass model seen from the same viewpoint as the surface mesh in panel A. (C) Diagram of the circle of Willis highlighting the vessels included in the vascular geometry. (D) Surface mesh viewed from the +y-direction to match orientation of the diagram in panel C.*

arteries (ACAs), the right middle cerebral artery (MCA) and the right internal carotid artery (ICA). The vessels' radii ranged from 0.9 to 3.4 mm and the aneurysm had a maximum diameter of 11 mm.

3.2.2 Particle image velocimetry

Particle image velocimetry (PIV) experiments were performed to obtain in vitro measurements of the velocity field in the aneurysm. PIV is a technique in which small particles follow the flow of a fluid through a transparent model [156]. The particles are illuminated by a thin laser sheet and two images are captured on camera shortly after each other. Knowing the time between the two images and the pixel size, the in-plane velocity components of the flow field can be determined. In our experiments, the laser sheet plane corresponded to the slice in Figure 3.1, which approximately sliced the main flow jet into the aneurysm along its axis.

Details on the PIV set-up for our study were previously reported by Palero et al. [144].

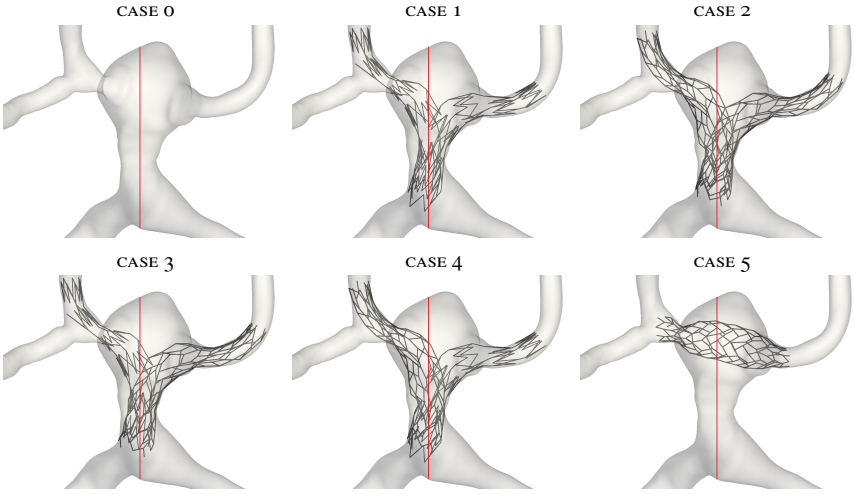

Figure 3.2: *Vascular model with and without virtually deployed stents. The red line indicates the slice location. Stent configurations were composed of open cell stents and closed cell stents. Case 0 corresponded to the untreated aneurysm, case 1 had two open cell stents, case 2 had two closed cell stents, case 3 and 4 both had one open cell stent and one closed cell stent, and case 5 had one closed cell stent.*

Briefly, it consisted of a New Wave Pegasus laser and a LaVision HighSpeedStar 5 camera with a CMOS sensor of 1024×1024 pixels. The nominal pixel size was $17\,\mu m \times 17\,\mu m$. The time interval between the images was $400\,\mu s$. We used a fluid that matched the refractive index of borosilicate glass ($n = 1.4734$) and that had a blood-like density $\rho = 1054\,kg/m^3$ and viscosity $\mu = 6.45\,mPa\,s$. This fluid was a mixture of benzyl alcohol ($n = 1.54$) and glycerol triacetate ($n = 1.429$) in a ratio of 40/60. The fluid was seeded with 4 to $7\,\mu m$ latex particles and pumped into the glass model through inlets 1 and 2 (Figure 3.1). Inflow rates were kept constant and could be controlled by changing the voltage of the pump. During image acquisition mass flow rates were measured at each inlet and outlet with a Transonic TS410 ultrasonic probe: 14.135 g/s (Reynolds number = 631) at inlet 1; 4.001 g/s (361) at inlet 2; 5.201 g/s (371) at outlet 1; 5.730 g/s (406) at outlet 2; and 7.201 g/s (420) at outlet 3. The glass model was immersed in a rectangular glass cell filled with the same liquid as inside the glass model to avoid reflections at its external wall.

3.2.3 Surface reconstruction and virtual stent deployment

The glass model was imaged with a 3DRA scanner (AXIOM Artis, Siemens Medical Solutions, Erlangen, Germany). The voxel size was $0.27\,mm \times 0.27\,mm \times 0.27\,mm$. The image was segmented by isosurface extraction to obtain a triagulated surface mesh representation of both the inner and outer surface of the glass model. To determine the optimal intensity value of the isosurface, branch diameters were compared between the computer and the

Table 3.1: *List of challenge participants.*

ID	Research group	Mesh software[a,b]	CFD software[a,b]
A	Beijing University of Technology and Beijing Union University, China	ICEM CFD v12.1	CFX v12. 1
B	Tohoku University, Sendai, Japan	GAMBIT v2.4	FLUENT v6.3
C	Universidad de la República, Montevideo, Uruguay	caffa3d.MBRi	caffa3d.MBRi
D	Otto-von-Guericke University Magdeburg, Germany	ICEM CFD v13.0	FLUENT v13.0
E	Universitat Pompeu Fabra, Barcelona, Spain	ICEM CFD v13.0	CFX v13.0
F	Universitat Rovira i Virgili, Tarragona, Spain	ICEM CFD v13.0	FLUENT v13.0

[a] ICEM CFD, GAMBIT, FLUENT and CFX are commercial software packages developed by ANSYS (Canonsburg, PA, USA).
[b] caffa3d.MBRi is an open-source software package developed by G. Usera [188].

physical model. As only the inner surface, which corresponded to the lumen edge, was relevant for our CFD analysis, the outer surface was discarded. The surface mesh was smoothed using a geometry-preserving smoothing algorithm [142] to reduce small surface perturbations. All inlet and outlet branches were clipped perpendicular to their axes and were, measured from the aneurysm, at least 10 diameters in length.

To aid the analysis of the data, we rigidly transformed the surface mesh such that the CFD output sliced by the xy-plane would match the PIV image (Figure 3.1). The position of the surface mesh with respect to the PIV image was initialized based on visual assessment during acquistion. It was further refined by comparing the shape of the slice edge with the lumen edge visible in the PIV image.

Clinicians of the Hospital Clínic in Barcelona, Spain, were consulted to propose stent configurations for treatment with high-porosity stents. They could choose any combination of two available stents: 1. Neuroform (Boston Scientific, Natick, MA, USA) open cell stent, and 2. Enterprise (Cordis, Miami Lakes, FL) closed cell stent. We adopted the strut patterns of these commercial stents, but changed the struts to be circular with a diameter of 0.1 mm [17]. Figure 3.2 shows the five proposed configurations. These five different treatments will be referred to as cases 1 to 5, whereas the untreated aneurysm will be referred to as case 0. Stents were virtually deployed using the constrained deformable simplex model approach developed by Larrabide et al. [115].

3.2.4 The challenge

The challenge was launched on 1 June 2011 with a call for participants sent out to the research community. Participants were invited to simulate the steady-state velocity field for all cases, assuming blood to be an incompressible Newtonian fluid with $\rho = 1054\,\mathrm{kg/m^3}$ and $\mu = 6.45\,\mathrm{mPa\,s}$ and the vessel wall to be rigid with a no-slip boundary condition. To guarantee adequate space discretization, participants were required to demonstrate the mesh independency of both untreated and treated solutions. As input data, we provided surface meshes of the vascular geometry and the deployed stent geometries, and flow rate boundary conditions for all inlets and outlets. As output, participants were invited to

submit an abstract to the 8th International Interdisciplinary Cerebrovascular Symposium 2011 (ICS'11; formerly known as the International Intracranial Stent Meeting), outlining their methods, reporting on their mesh dependency study, showing velocity contour plots on the slice and velocity profiles along the y-axis, and giving their interpretation of the performance of each stent configuration.

Of the eleven research groups that accepted the challenge, six succeeded to complete the CFD analysis and submit an abstract before the deadline on 7 August 2011 (Table 3.1). Five groups used commercial software produced by ANSYS (Canonsburg, PA, USA): ICEM CFD or GAMBIT for volumetric mesh generation and as CFD solver either cell-centered finite volume solver FLUENT or vertex-centered finite volume solver CFX. All these five groups created tetrahedral body-fitted meshes with on average 1.2 million elements (range: 0.6 to 2.0 million) for the untreated case and 3.5 million elements (range: 1.7 to 6.7 million) for the treated cases. To resolve the stent struts, elements with a relatively small edge length were used near the struts: groups A, B and D used an edge length of 0.04 mm, groups E and F used an edge length of 0.05 mm. The remaining group, group C, used its own open-source finite volume solver caffa3d.MBRi, which employed blocks of cubic elements and an immersed boundary approach to represent the vessel and stent geometries. They used 4.3 million elements for the untreated case (edge length of 0.15 mm) and 37.5 million elements for the treated cases (edge length of 0.075 mm). More details on caffa3D.MB, the predecessor of caffa3D.MBRi, can be found in [188].

Preliminary results of the challenge were published in the proceedings of ICS'11 and presented at the conference, which was held on 8–11 September 2011 in Shanghai, China.

3.2.5 Data analysis

After the challenge, all CFD solutions were collected and converted into VTK unstructured grids. In the case of group C, this was achieved by linearly interpolating the solutions onto the volumetric mesh of group F (arbitrary choice). Post-processing steps were carried out using Python 2.7.5 with libraries VTK 5.10.1, VMTK 1.2 [5] and Matplotlib 1.3.1 [86].

As mentioned earlier, the CFD output sliced by the xy-plane matched the PIV image. In the data analysis, we therefore focused on the in-plane velocity on this slice. To qualitatively compare the PIV and CFD results and the CFD results between research groups, we plotted velocity profiles along the y-axis and created contour plots of the velocity field on the slice (Figure 3.1). To quantitatively compare the results, we calculated the root-mean-square error (RMSE) of the velocity as follows. All PIV and CFD results were linearly interpolated onto a uniformly meshed slice with a nominal node spacing of 0.5 mm. Nodes outside the field of view of the PIV image or outside the computational domain of the CFD result were excluded from analysis. Note that due to slight variations in space discretization, nodes at the edge of the slice or near stent struts sometimes fell inside the computational domain for one research group but outside for another. Therefore, per case we only considered those nodes that fell within the computational domain for all groups. Subsequently, the velocity was averaged over all groups to obtain a reference CFD

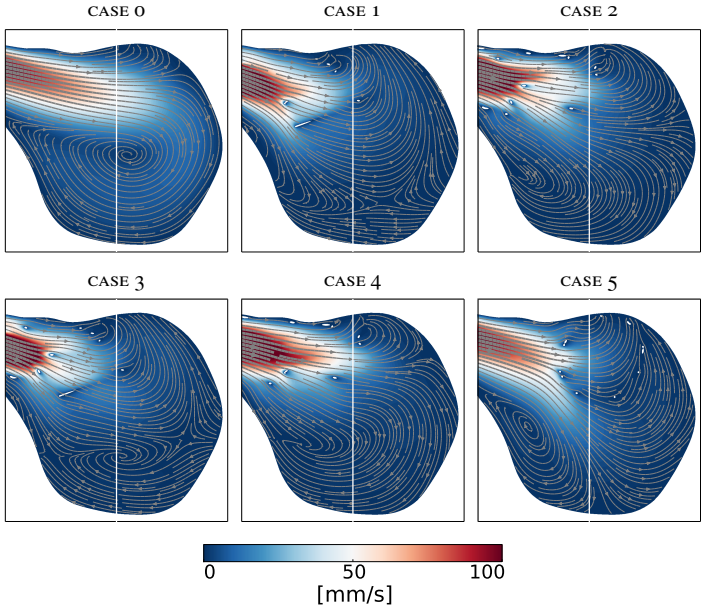

Figure 3.3: *All cases. In-plane velocity field with streamlines superimposed. The white line indicates the y-axis. White holes mark the location of stent struts. Results are from group E (arbitrary choice).*

result for each case. The node-wise RMSE of each PIV and CFD result was calculated with respect to this reference. Additionally, to put the error measurement in context, the RMSE was normalized (NRMSE) by the maximum velocity of the untreated case, as suggested by [191].

3.3 Results

Figure 3.3 shows for all cases the velocity field on the slice. Streamlines were superimposed to illustrate how stents changed not only the velocity magnitude, but also the flow direction. In the untreated case, the main flow jet entered the aneurysm, impinged the distal wall, and created one large vortex. In the treated cases, stent struts broke the main flow jet into several jets of reduced strength, leaving regions of low velocity in their wake and forming multiple vortices. In all cases, the fluid flowed to the top of the aneurysm toward the outlets.

Some similarities can be observed between cases. Cases 1 and 3 had relatively complex flow patterns, including a large vortex rotating in the direction opposite to the vortex in case 0. Cases 2 and 4 were more similar to case 0, but with the dominating flow jet impinging lower on the distal wall. These similarities are also apparent in Figure 3.4, which shows velocity profiles along the y-axis. The peak in case 0, corresponding to the main flow jet, was split into two relatively low-velocity peaks in cases 1 and 3, whereas one relatively

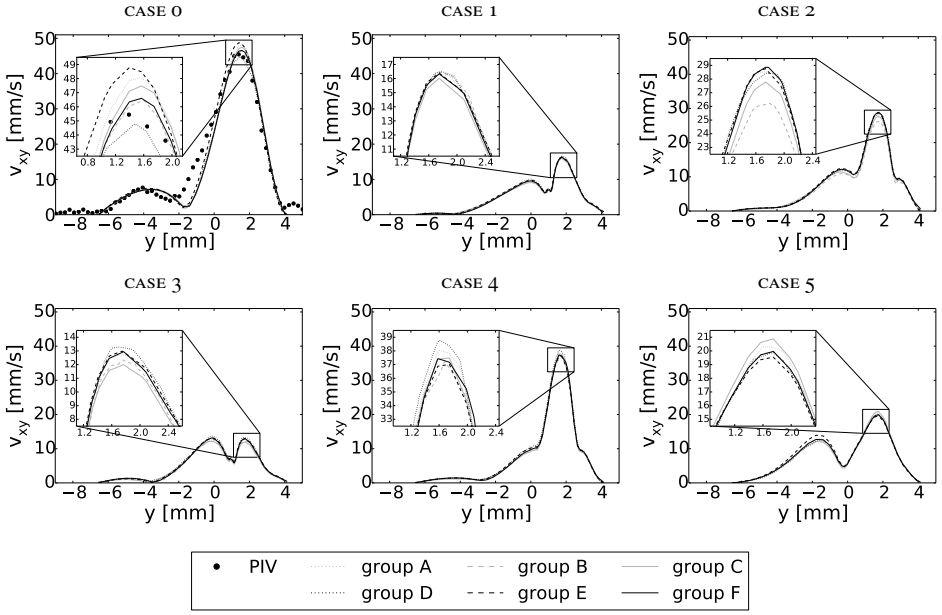

Figure 3.4: *All cases. In-plane velocity profile along the y-axis.*

high-velocity peak remained in cases 2 and 4. Note that these similarities can be partly attributed to the location of the y-axis with respect to the stent struts. As Figure 3.2 shows, inside the aneurysm the xy-plane sliced only one of the stents: the open cell stent in cases 1 and 3, and the open cell stent in cases 2 and 4. This is reflected by the identical stent strut patterns near the y-axis shown in Figure 3.3.

Case 5 was distinct from cases 1 to 4 with only a single stent located inside the aneurysm and without any stents in the parent vessel. By approximation, the slice shows a cross section of the stent and the y-axis runs through its center. The main flow jet was split into one part entering the stent and one part strongly diverted and impinging the bottom of the aneurysm. Two corresponding peaks can be seen in the velocity profile.

To qualitatively compare the PIV and CFD results and the CFD results between research groups, we considered the in-plane velocity profiles along the y-axis in Figure 3.4 and the in-plane velocity field on the slice in Figures 3.5 to 3.10. To quantitatively compare the results, we calculated the RMSE as previously described and normalized it with the maximum velocity of the untreated case of 97.8 mm/s to obtain the NRMSE.

The PIV result was reproduced well by each research group (Figures 3.4 and 3.5). The main differences were that in the PIV image the main flow jet was slightly broader and the vortex core was positioned slightly lower. The RMSE between the PIV result and the reference CFD result was 7.12 mm/s and the NRMSE was 7.28 %. To check the sensitivity of this error measurement to the exact location of the PIV image with respect to the vascular model, we repeated the measurement for parallel slices at different positions along the z-

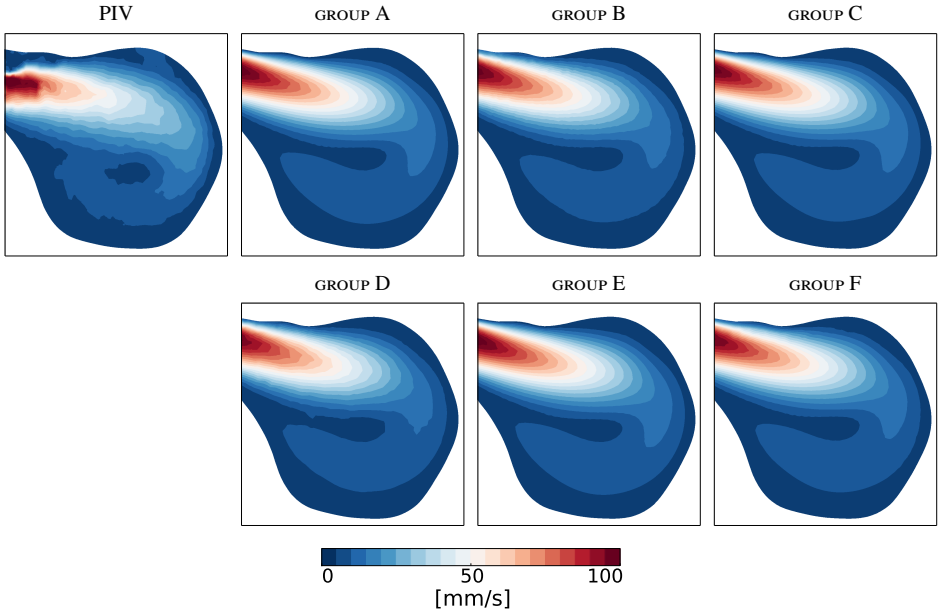

Figure 3.5: *Case 0. In-plane velocity field.*

axis. Similar RMSEs were found for slices at $z = -0.5$ mm (RMSE = 7.27 mm/s) and at $z = 0.5$ mm (RMSE = 6.96 mm/s).

CFD results from the different research groups participating in the challenge were very similar (Figures 3.4 to 3.10). The largest differences were found in regions with high velocity gradients such as the peaks of the velocity profiles where the maximum difference between any two groups was 4.0 mm/s, i.e. 4.1 % of the maximum velocity of the untreated case. The average RMSE between each research groups' CFD result and the reference CFD result was 0.46 mm/s (range: 0.27 to 1.00 mm/s) and the average NRMSE was 0.47 % (range: 0.28 to 1.03 %).

3.4 Discussion

3.4.1 Accuracy of hemodynamic simulations

The first objective of this challenge was to validate the velocity field of the untreated case against in vitro measurements. Similar to previous validation studies [61, 82, 157, 187], we found good agreement between CFD and PIV. Differences between the two techniques can be attributed to various aspects.

First, PIV measurements were affected by equipment and operator accuracy. To estimate the accuracy of our PIV measurements, we refer back to the study by Palero et al. in which the same glass model was used to demonstrate a new technique, which also

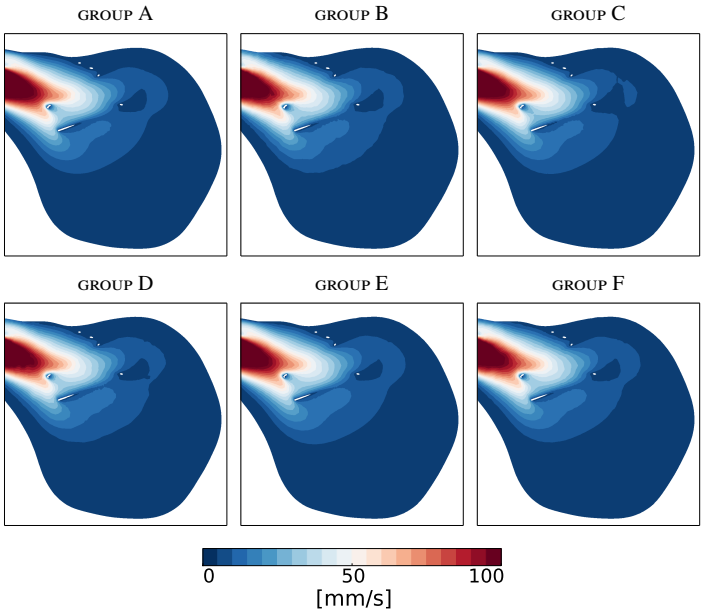

Figure 3.6: *Case 1. In-plane velocity field.*

uses a PIV set-up, called digital image plane holography [144]. Compared to regular PIV, the root-mean-square difference was 5 % of the maximum velocity measured with PIV, which is similar to the 7.28 % NRMSE we found between PIV and CFD. Additionally, slight inaccuracies in the refractive index matching between glass and fluid may have led to inaccuracies in the measured velocity field, most notably in regions where the normal on the glass surface was nearly perpendicular to the optical axis [187]. This could explain the relatively large differences between CFD and PIV near the aneurysm neck (see top left corner of the contour plot in Figure 3.5).

Second, CFD solutions were affected by the accuracy of input parameters. Even small geometric changes in the vascular model introduced during imaging or segmentation could have had a relatively large effect on the velocity field [82]. The location of the PIV plane with respect to the vascular model was estimated to be accurate within 1 mm and shifting the slice position along the z-axis by 0.5 mm in either direction changed the RMSE by 2 %. During the PIV experiment, we repeatedly measured the mass flow rate at all inlets and outlets and the fluid's viscosity. The coefficient of variation of these measurements was 1 % for the mass flow rate and 2.5 % for the viscosity.

3.4.2 Reproducibility of hemodynamic simulations

The second objective of this challenge was to quantify the reproducibility between groups for both untreated and treated cases. Similar to VISC'07, we found excellent agreement between all research groups [155]. The average NRMSE of 0.47 % lay within the typical

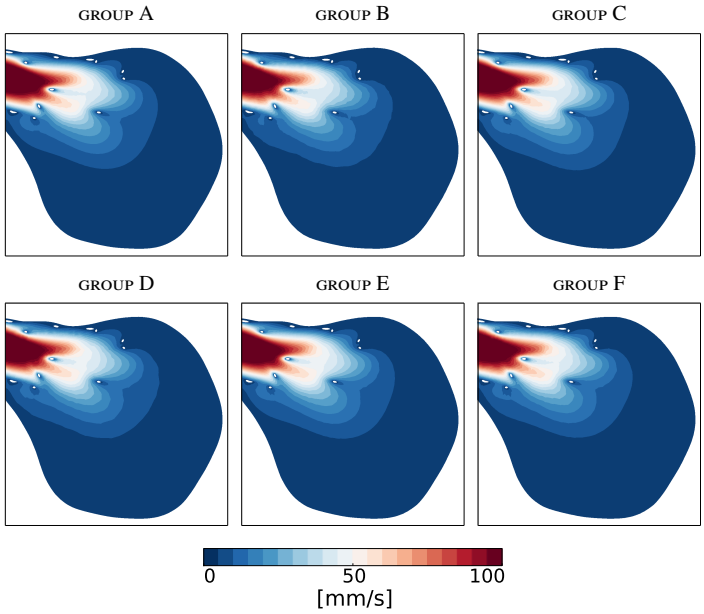

Figure 3.7: *Case 2. In-plane velocity field.*

tolerance threshold used in mesh dependency analyses. In fact, probably due to the higher mesh resolution near the stent struts, the NRMSE was significantly lower in treated cases than in the untreated case (0.45 vs. 0.59 %, $p \leq 0.05$ (Wilcoxon rank-sum test)).

3.4.3 Interpretation of treatment performance

The third objective of this challenge was to compare the groups' independent interpretations of the performance of each stent configuration. Predominantly, the hemodynamic analyses were carried out on the basis of the velocity contour plots and velocity profiles shown in this chapter. Some groups additionally created streamlines to assess the complete three-dimensional velocity field in the aneurysm or considered the wall shear stress on the aneurysm wall.

The general consensus was that in cases 1 and 3 the stents were most successful in diverting the main flow jet and reducing peak velocity. One group performed a quantitative assessment by considering the flow rate into the aneurysm and found reductions of 20 to 30 % with the largest reductions in cases 2 and 4. However, the reduction and ranking of treatments by reduction depended strongly on the location of the plane across which the inflow rate had been calculated.

A more comprehensive evaluation of the flow changes (e.g. changes in wall shear stress, vorticity, residence time, etc.) would be required to fully assess the advantages and disadvantages of each treatment option. Also, we would like to point out that the flow distribution among inlets and outlets might be affected by the stents, especially under

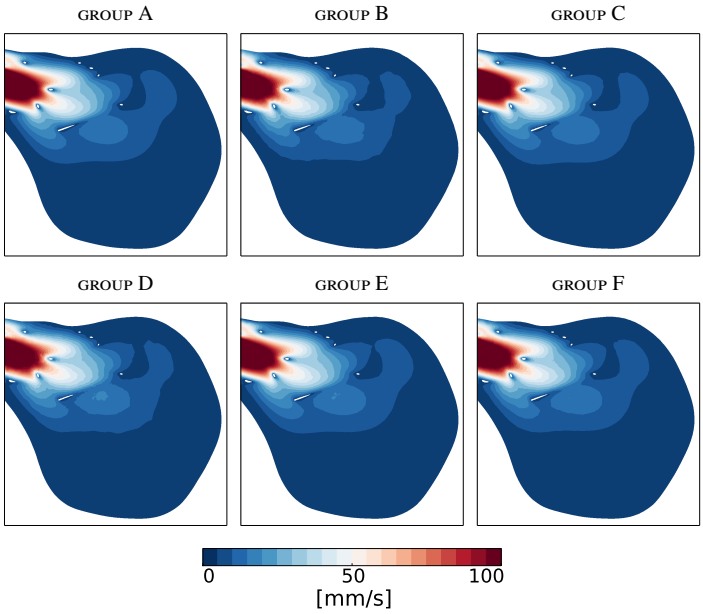

Figure 3.8: *Case 3. In-plane velocity field.*

pulsatile flow conditions. Therefore, rather than fixing the flow distribution as we did in the challenge, a more accurate flow field could be obtained by, for instance, linking the boundary conditions to a lumped parameter model representing the rest of the circulatory system [74].

3.4.4 Hemodynamic effect of high-porosity stents

The goal of endovascular treatment is to trigger thrombus formation and effectively exclude the aneurysm from the circulation [208]. Although the underlying mechanisms are not yet fully understood, favorable conditions for thrombus formation are low blood flow velocities and high blood residence times.

High-porosity stents, like the ones in this challenge, are primarily used to provide structural support for coils, but clearly induce a non-negligable reduction of the flow velocity. Their flow diverting properties have been linked to the higher success rate of stent-assisted coiling versus conventional coiling [89, 119], and have been successfully exploited by treating patients solely with these stents [43, 179, 211].

Other than with low-porosity stents, the designs of high-porosity stents are not optimized to divert flow and their performance may strongly depend on the exact positioning of the stent, and hence the stent struts, during its deployment [155]. To better understand the impact of high-porosity stents on intra-aneurysmal hemodynamics, CFD studies have been carried out to compare stent designs [66, 106], stent positioning [8], and stent configurations [14, 91, 110]. Our challenge has demonstrated that, given geometry and

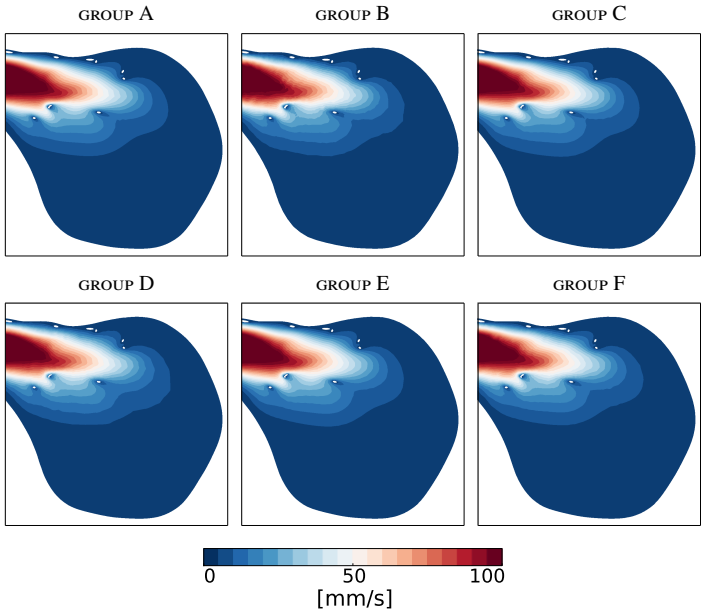

Figure 3.9: *Case 4. In-plane velocity field.*

flow rate boundary conditions, the CFD solutions of such studies can be consistently obtained by different research groups.

3.4.5 Future challenges

In this challenge, participants were provided with geometries and flow rate boundary conditions, and were free to choose meshing and CFD strategies. However, often when creating 'patient-specific' blood flow simulations, the only available input data are medical images of the cerebral vasculature. Future challenges may wish to give more freedom to participants by letting them extract the vascular geometry and/or choose the flow rates. As CFD solutions are most sensitive to uncertainties in these modeling assumptions [71, 102, 131, 164], we expect a greater variability between solutions.

A year after VISC'11, the ASME 2012 Summer Bioengineering Conference CFD Challenge attracted 25 research groups to calculate the pressure drop in a parent vessel of a giant aneurysm with a proximal stenosis [174]. Besides also suggesting to give more freedom to participants of future challenges, they offered another idea that we would like to reiterate. Although we sometimes observe large variabilities for simulated hemodynamic quantities, the stratification of a population of aneurysms for rupture risk or treatment success might remain unchanged. Therefore, rather than performing a detailed analysis of a single case, future challenges may wish to focus on the stratification of a population according to one or more agreed-upon hemodynamic criteria and, thus, investigate the reproducibility of clinically relevant information.

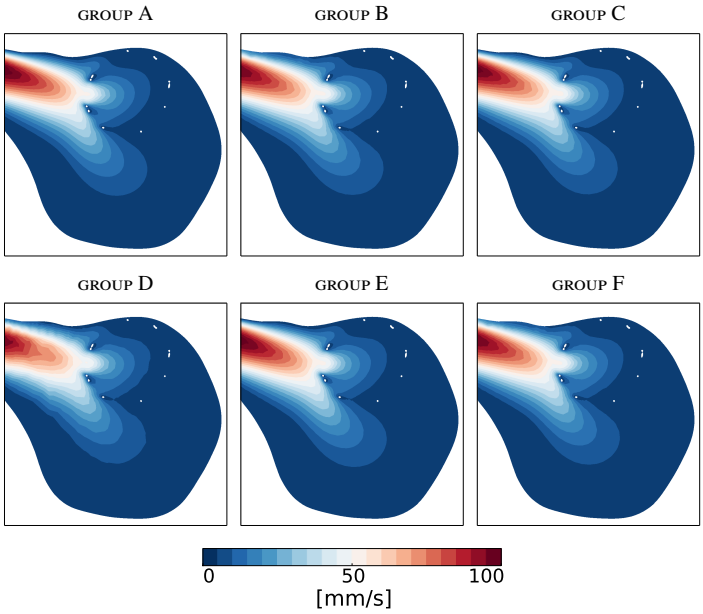

Figure 3.10: *Case 5. In-plane velocity field.*

3.5 Conclusions

This CFD challenge has demonstrated that, given stent and vascular geometries, and flow rate boundary conditions, research groups can accurately simulate the velocity field inside a cerebral aneurysm – as assessed by comparison with in vitro measurements – and find excellent agreement on the hemodynamic effect of different stent configurations. Future challenges may wish to focus more on the interpretation of the computed flow field and on predictions regarding aneurysm rupture and treatment success.

3.6 Online data

To promote the future use of the VISC'11 dataset, both the input data provided to the challenge participants and the PIV-measured velocity field have been made available on Figshare*†. Additionally, the CFD solutions of group E are also available on Figshare‡. Group C has made available the code to their well-documented open-source CFD solver caffa3d.MBRi§ and their VISC'11 solutions¶.

*http://dx.doi.org/10.6084/m9.figshare.1060443
†http://dx.doi.org/10.6084/m9.figshare.1060453
‡http://dx.doi.org/10.6084/m9.figshare.1060464
§http://www.fing.edu.uy/imfia/caffa3d.MB
¶http://www.fing.edu.uy/imfia/caffa3d.MB/CaffaViscTutorial.tar.gz

4

Approximating hemodynamics with steady flow simulations

Abstract — Computational fluid dynamics (CFD) simulations can be employed to gain a better understanding of hemodynamics in cerebral aneurysms and improve diagnosis and treatment. However, introduction of CFD techniques into clinical practice would require faster simulation times. The aim of this study was to evaluate the use of computationally inexpensive steady flow simulations to approximate the aneurysm's wall shear stress (WSS) field. Two experiments were conducted. Experiment 1 compared for two cases the time-averaged (TA), peak systole (PS) and end diastole (ED) WSS field between steady and pulsatile flow simulations. The flow rate waveform imposed at the inlet was varied to account for variations in heart rate, pulsatility index, and TA flow rate. Consistently across all flow rate waveforms, steady flow simulations accurately approximated the TA, but not the PS and ED, WSS field. Following up on experiment 1, experiment 2 tested the result for the TA WSS field in a larger population of 20 cases covering a wide range of aneurysm volumes and shapes. Steady flow simulations approximated the space-averaged WSS with a mean error of 4.3 %. WSS fields were locally compared by calculating the absolute error per node of the surface mesh. The coefficient of variation of the root-mean-square error over these nodes was on average 7.1 %. In conclusion, steady flow simulations can accurately approximate the TA WSS field of an aneurysm. The fast computation time of 6 minutes per simulation (on 64 processors) could help facilitate the introduction of CFD into clinical practice.

Adapted from: Geers AJ, Larrabide I, Morales HG, Frangi AF. *Approximating hemodynamics of cerebral aneurysms with steady flow simulations.* Journal of Biomechanics, 47(1):178–185, 2014

4.1 Introduction

Growth and rupture of cerebral aneurysms have been associated with the intra-aneurysmal hemodynamics [75]. Better understanding of hemodynamics could improve diagnosis and treatment. In the last decade, computational fluid dynamics (CFD) simulations have been employed to study the relationship between hemodynamics and rupture [41, 42, 137, 209] and the hemodynamic effect of endovascular treatment [40, 101, 114, 140]. In particular, research has focused on the wall shear stress (WSS), which is a key regulator of vascular biology and pathology [53, 125].

The majority of studies use unsteady, *pulsatile* flow simulations to capture the changing flow rate and inertia effects during the cardiac cycle. The enormous amount of generated data is typically reduced by extracting and analyzing the time-averaged (TA) [42, 137, 209], peak systole (PS) [30, 170] or end diastole (ED) flow field [67, 95]. Some researchers have argued, however, that in many cases the main flow features in the aneurysm remain relatively stable throughout the cardiac cycle [126, 141] and that computationally much less expensive *steady* flow simulations might already provide clinically relevant hemodynamic information [42]. The shorter time required to create these simulations could aid in the introduction of CFD into clinical practice. So far, comparisons between steady and pulsatile flow simulations have mostly been qualitative and based on few cases, but before steady flow simulations can be relied upon, it is essential to quantify for a large population the accuracy with which they can approximate aspects of the pulsatile flow field in the aneurysm.

The aim of this study was to quantify the error with which steady flow simulations can approximate the aneurysm's TA, PS, and ED WSS fields derived from pulsatile flow simulations. Since this error might depend on the flow rate waveform (FRW) imposed at the inlet of the vascular model, we systematically varied the heart rate, pulsatility index, and TA flow rate. The study's dataset included both terminal and lateral aneurysms, covering a wide range of aneurysm volumes and shapes.

4.2 Methods

4.2.1 Blood flow modeling

Aneurysm models included in this study were drawn from a large database created within the EU project @neurIST [198]. Patient-specific vascular models, represented by triangular surface meshes, were constructed by segmenting three-dimensional rotational angiography (3DRA) images using a geodesic active regions approach [20]. These models were smoothed using a geometry-preserving smoothing algorithm [142] to reduce small surface perturbations without displacing vertices by more than 0.02 mm. Touching vessels were removed. All inlet and outlet branches were clipped perpendicular to their axes and were, respectively, 12 and 4 diameters in length. To define the aneurysm region, the

Table 4.1: *Flow rate waveform descriptors.*

	Physiological variation		
Descriptor	lower	baseline	upper
Heart rate [bpm][a]	52	68	84
Pulsatility index [-][a]	0.58	0.92	1.26
TA flow rate [ml/s][b]	0.73 Q_A	Q_A	1.27 Q_A

[a] baseline = mean, lower = mean − 2SD, and upper = mean + 2SD where the mean and standard deviation (SD) are taken from [59] and [81].
[b] $Q_A = 48.21\,A^{1.84}$ where A is the inlet area in cm^2 [33].

aneurysm neck was manually delineated and a neck surface was automatically created from this curve. This approach has been demonstrated to have a low interobserver variability for volume and surface area measurements of the aneurysm [116]. All mesh editing operations were performed in @neuFuse (B3C, Bologna, Italy) [198], a software application developed within @neurIST.

Unstructured volumetric meshes were created using the octree approach with ICEM CFD 13.0 (ANSYS, Canonsburg, PA, USA). Meshes were composed of tetrahedral elements of 0.24 mm, and three prism layers with a total height of 0.08 mm and a side length of 0.12 mm. The total number of elements ranged from 1.2 to 3.8 million, the density from 1420 to 2950 elements per mm^3, depending on the surface-area-to-volume ratio of the computational domain. This mesh setup was selected following mesh dependency tests performed on both cases of experiment 1 (see Section 4.2.3). These tests demonstrated the mesh independency of the WSS field for steady flow simulations under the highest inflow rate conditions considered in this study.

CFD simulations were created with the commercial finite volume solver CFX 13.0 (ANSYS), using a second-order advection scheme, a second-order backward Euler transient scheme for unsteady simulations, and CFX' automatic time scale control for steady-state simulations. Solutions converged until the normalized residual of the WSS everywhere in the computational domain was $< 10^{-5}$. Blood was modeled as an incompressible Newtonian fluid with density $\rho = 1060\,kg/m^3$ and viscosity $\mu = 4$ mPa s. Vessel walls were assumed rigid with a no-slip boundary condition. Flow rate values (steady) or waveforms (pulsatile) were imposed at the inlet and zero-pressure boundary conditions at all outlets. For pulsatile flow simulations, the cardiac cycle was discretized in 200 uniformly distributed time steps and, to reduce the effect of initial transients, the second of two simulated cardiac cycles was analyzed. Tests performed on both cases of experiment 1 demonstrated WSS differences of < 1 % with respect to simulations with either 400 uniformly distributed time steps per cardiac cycle or from which the third cycle was analyzed.

4.2.2 Flow rate waveform transformation

FRWs describe how flow rate $Q(t)$ at the inlet of the vascular models changes over time t during the cardiac cycle. In this study, we used a physiological FRW $Q^0(t)$ that was

derived from phase-contrast magnetic resonance images of the internal carotid artery (ICA) of a healthy volunteer [36]. This FRW was then linearly transformed to obtain a FRW with specified heart rate (*HR*), TA flow rate (Q_{TA}), and pulsatility index (*PI*) given by $PI = (Q_{\mathrm{PS}} - Q_{\mathrm{ED}})/Q_{\mathrm{TA}}$. These three variables will be referred to as FRW descriptors. The transformation is given by

$$Q(t) = a\, Q^0(ct) + b \tag{4.1}$$

where

$$a = \frac{Q_{\mathrm{TA}}}{Q^0_{\mathrm{TA}}}\frac{PI}{PI^0}, \qquad b = Q_{\mathrm{TA}}(1 - \frac{PI}{PI^0}), \qquad c = \frac{HR}{HR^0}$$

Physiological values for the FRW descriptors (see Table 4.1) were derived from the literature. For each descriptor, we defined a baseline, an upper and a lower value. Values for *HR* and *PI* were obtained using the mean and standard deviation (SD) of these descriptors reported by Ford et al. and Hoi et al. [59, 81]: baseline = mean, lower = mean − 2SD, and upper = mean + 2SD. Values for Q_{TA} were obtained using the relationship $Q_A = 48.21\, A^{1.84}$ where Q_A is in ml/s and A is the inlet's cross-sectional area in cm^2 [33]. This relationship was determined by fitting a power-law function through measurements of Q and A of the ICAs and vertebral arteries of 11 normal subjects. Values for Q_{TA} were given by: baseline = Q_A, lower = $0.73Q_A$, and upper = $1.27Q_A$. The 27 % percent variation is the average relative error between prediction and measurement, derived from [33].

4.2.3 Experiments

Two experiments were conducted in this study. Figure 4.1 schematically represents the workflows of both experiments.

Experiment 1 was a detailed analysis of two cases to compare between steady and pulsatile flow simulations the TA, PS, and ED WSS fields, and to assess how the results depend on FRW descriptors. One aneurysm was located at the internal carotid bifurcation (terminal case) and one near the ophthalmic artery (lateral case). Per case, seven pulsatile flow simulations were created, each with a different FRW imposed at the inlet: one FRW with all descriptors at baseline, three FRWs with two descriptors at baseline and the third at its lower value, and three FRWs with two descriptors at baseline and the third at its upper value. Per pulsatile flow simulation, three steady flow simulations were created with corresponding flow rates imposed at the inlet: one with TA flow rate, one with PS (i.e. maximum) flow rate, and one with ED (i.e. minimum) flow rate. Because some flow rate values were repeated, a total of 13 steady flow simulations were created for both cases. Reynolds numbers (Re) ranged from 58 to 432 and Womersley numbers (α) from 2.6 to 4.2.

Experiment 2 was a follow-up of experiment 1, in which we found that the TA, but not the PS and ED, WSS field could be accurately approximated with steady flow simulations. To quantify in a larger population the error with which the TA WSS field

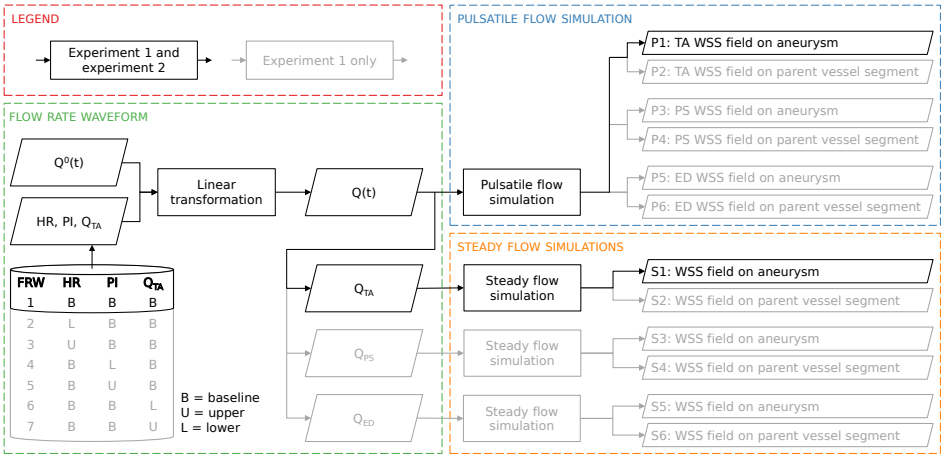

Figure 4.1: *Workflows of experiments 1 and 2. Sets of FRW descriptors HR, PI and Q_{TA} were created by keeping two descriptors at baseline and varying the third from lower to baseline to upper value (see Table 4.1). For each set of FRW descriptors, $Q^0(t)$ was linearly transformed to obtain $Q(t)$ from which then Q_{PS} and Q_{ED} were derived. One pulsatile flow simulation was created with $Q(t)$ imposed at the inlet of the vascular model and three corresponding steady flow simulations were created with flow rates Q_{TA}, Q_{PS} and Q_{ED} imposed at the inlet. In the data analysis, WSS field S1 was compared to P1, S2 to P2, etc.*

could be approximated, we selected 10 terminal and 10 lateral cases, covering a wide range of aneurysm volumes and shapes. Aneurysm shape was quantified with the nonsphericity index (NSI) given by $\mathrm{NSI} = 1-(18\pi)^{1/3}\, V^{2/3} S^{-1}$ where V is the volume and S is the surface area of the aneurysm [51]. Volumes ranged from 6 to 1315 mm^3 and NSIs from 0.03 to 0.32. Per case, we created one pulsatile flow simulation with the baseline FRW imposed at the inlet and one steady flow simulation with the corresponding TA flow rate imposed at the inlet. Reynolds numbers ranged from 44 to 301 and Womersley numbers from 2.1 to 4.3.

4.2.4 Data analysis

In experiment 1, two regions of interest (ROIs) were manually defined (Figure 4.2): a parent vessel segment of one diameter length just upstream from the carotid siphon and the aneurysm. The parent vessel segment was included in the analysis to elucidate the difference with the aneurysm. From the pulsatile flow simulation, the TA, PS, and ED WSS fields of both ROIs were extracted, where PS and ED were defined as the timesteps at which the space-averaged WSS ($\overline{\mathrm{WSS}}$) on the ROI was maximum and minimum, respectively. From the steady flow simulations, the corresponding WSS fields were extracted. In experiment 2, data analysis focused only on the TA WSS field of the aneurysm and the corresponding WSS field of the steady flow simulation.

To globally compare WSS fields, we calculated the $\overline{\mathrm{WSS}}$ of the ROI and the corre-

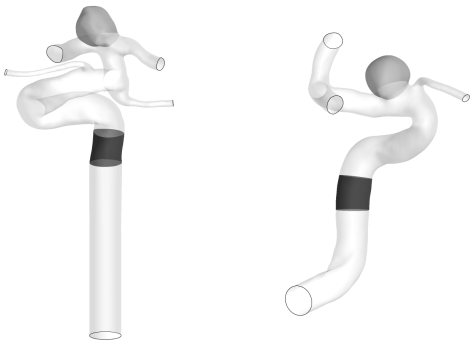

Figure 4.2: *Experiment 1. Vascular models of the terminal (left) and lateral (right) cases. The aneurysms are in light gray and the parent vessel segments are in dark gray.*

sponding relative error. To locally compare the fields, we visualized the absolute error of the WSS field and calculated the root-mean-square error (RMSE) over all nodes $i = 1, 2, \ldots, M$ of the ROI:

$$\mathrm{RMSE} = \sqrt{\frac{1}{M}\sum_{i=1}^{M}\left(\mathrm{WSS}_{\mathrm{pulsatile},i} - \mathrm{WSS}_{\mathrm{steady},i}\right)^2} \tag{4.2}$$

Additionally, the coefficient of variation (CV) of the RMSE was calculated to put the error measurement in context of $\overline{\mathrm{WSS}}$:

$$\mathrm{CVRMSE} = \mathrm{RMSE}/\overline{\mathrm{WSS}}_{\mathrm{pulsatile}} \tag{4.3}$$

4.3 Results

4.3.1 Experiment 1

Figure 4.3 shows $\overline{\mathrm{WSS}}$ on the parent vessel segment as a function of FRW descriptors. For both cases, steady flow simulations accurately approximated the TA $\overline{\mathrm{WSS}}$ with errors ranging from 0.0 to 1.5 %. PS $\overline{\mathrm{WSS}}$ was underestimated with errors ranging from 2.2 to 34.6 % and ED $\overline{\mathrm{WSS}}$ was overestimated with errors ranging from 1.7 to 23.3 %. The observed trends were consistent across all FRWs, but the size of the errors varied with changing FRW descriptors.

Figure 4.4 shows $\overline{\mathrm{WSS}}$ on the aneurysm as a function of FRW descriptors. The same as for the parent vessel segment, the aneurysm's TA WSS field was accurately approximated by steady flow simulations (error range: 1.9 to 7.8 %. Most notable difference with respect to the parent vessel segment was that steady flow simulations overestimated PS $\overline{\mathrm{WSS}}$ (8.0 to 48.8 %) and underestimated ED $\overline{\mathrm{WSS}}$ (8.5 to 30.0 %). Again, the observed trends were

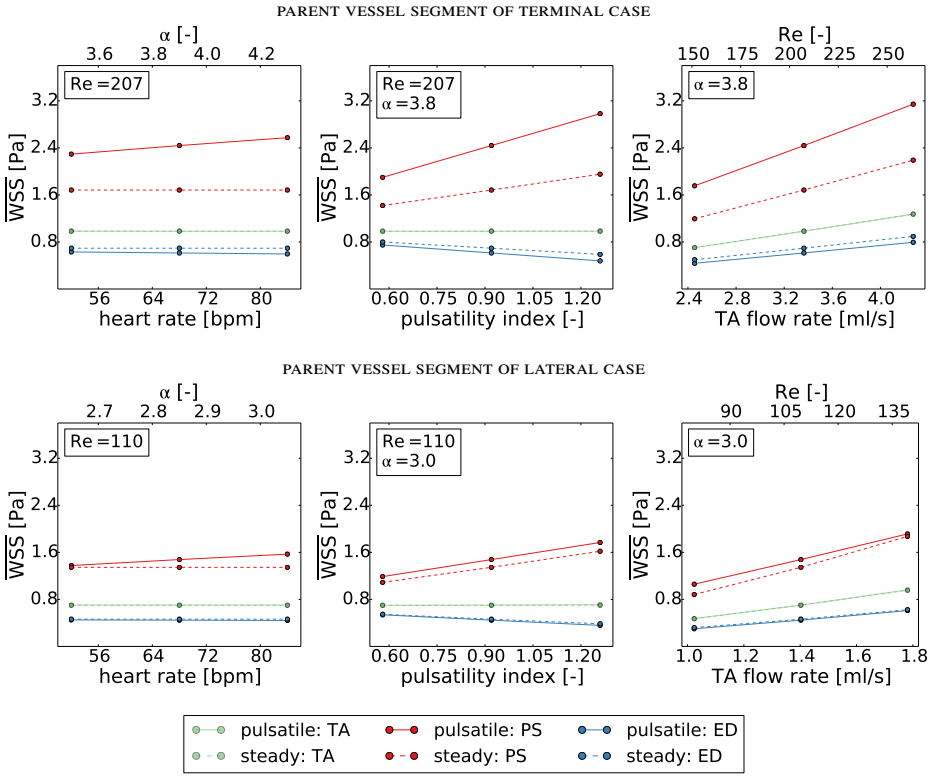

Figure 4.3: *Experiment 1. TA, PS, and ED* $\overline{\text{WSS}}$ *of the parent vessel segment as function of three FRW descriptors.*

consistent across all FRWs, but the size of the errors varied with changing FRW descriptors. Highlighting this variation for TA $\overline{\text{WSS}}$: errors remained approximately constant with increasing heart rate, increased with increasing pulsatility index, and decreased with increasing TA flow rate.

To visually compare the pulsatile and steady flow simulations, Figure 4.5 shows contour plots of the TA, PS, and ED WSS fields and the node-by-node absolute error. Figure 4.6 shows plots of the WSS magnitude along a line traced on the aneurysm wall. These plots correspond to the flow simulations with all three FRW descriptors at baseline. Steady flow simulations locally accurately approximated the TA WSS field on the aneurysm with a CVRMSE of 6.3 % for the terminal case and 5.2 % for the lateral case. Besides an offset in magnitude, the distribution of the PS and ED WSS fields was mostly similar. However, as the PS WSS field of the terminal case shows most clearly, relatively large differences in distribution could be found in some regions.

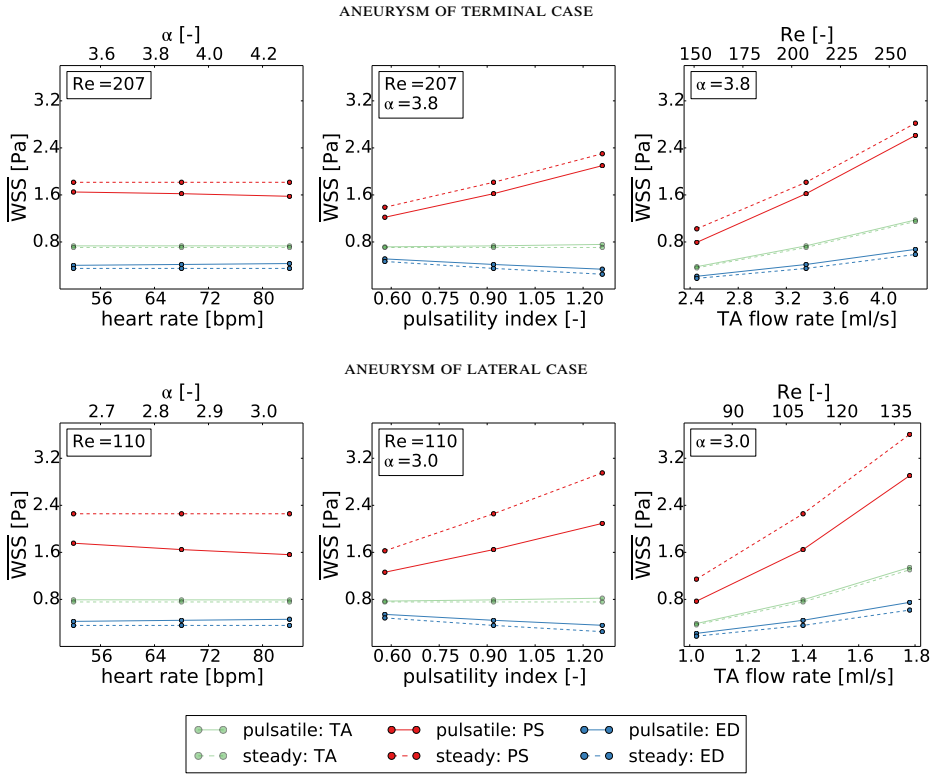

Figure 4.4: *Experiment 1. TA, PS, and ED* $\overline{\text{WSS}}$ *of the aneurysm as function of three FRW descriptors.*

4.3.2 Experiment 2

Figures 4.7 and 4.8 show contour plots of the TA WSS field and the absolute error of the TA WSS field, respectively. Colormaps were normalized to place the error in context of the aneurysm's $\overline{\text{WSS}}$. Relatively large local errors were found to coincide with regions of high WSS, such as the impingement region, and with regions of fluctuating WSS, which was assessed from animations of the changing WSS field during the cardiac cycle*.

Table 4.2 shows the relative error in $\overline{\text{WSS}}$ and CVRMSE. More details on the geometric and hemodynamic characteristics of each aneurysm can be found in Table 4.3. Steady flow simulations accurately approximated the $\overline{\text{WSS}}$ on the aneurysm with a relative error of 4.3 ± 1.7 % (mean ± standard error) and a CVRMSE of 7.1 ± 3.1 %. For all cases, $\overline{\text{WSS}}$ was slightly underestimated. To quantify the dependency of CVRMSE on the geometric characteristics of the aneurysm, we split the cases three times in two groups of 10: 1. by aneurysm type, 2. by volume, and 3. by NSI. On average, higher values of CVRMSE were found for terminal (8.4 %) vs. lateral (5.9 %) aneurysms, for large (7.9 %) vs. small (6.4 %)

*View animation online at http://dx.doi.org/10.6084/m9.figshare.1066898

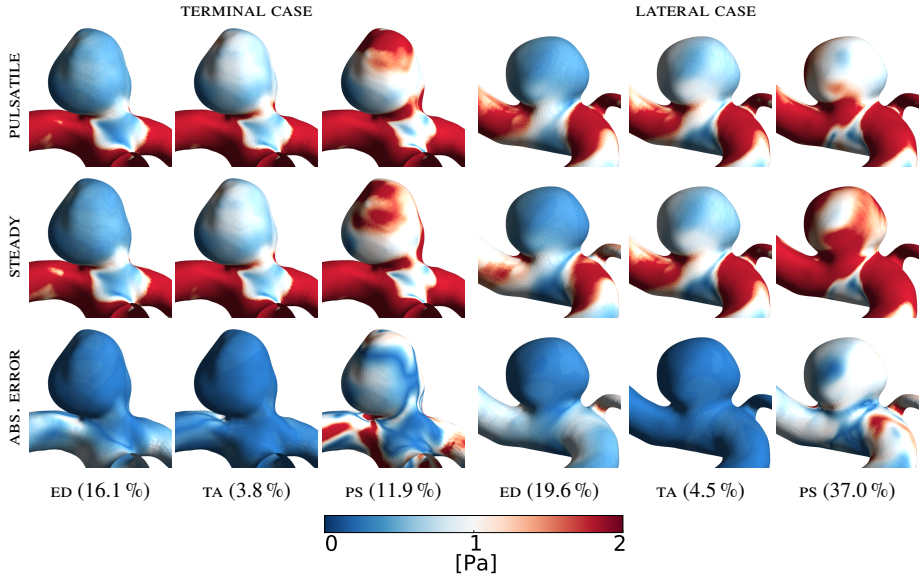

Figure 4.5: *Experiment 1. TA, PS, and ED WSS fields of the pulsatile (row 1) and steady (row 2) flow simulations, and the absolute error of the WSS field calculated at each node of the surface mesh (row 3). All three FRW descriptors were at baseline. View points were selected to best visualize the aneurysm, so images are not necessarily at the same scale. Part of the terminal case's parent vessel was clipped to prevent it from obstructing the view of the aneurysm. The percentages in parentheses indicate the error in space-averaged WSS.*

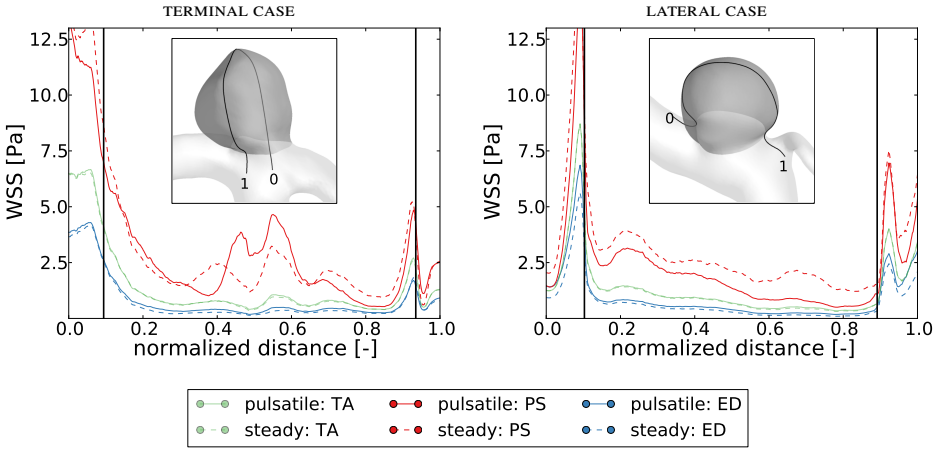

Figure 4.6: *Experiment 1. WSS magnitude along a line traced on the aneurysm wall. All three FRW descriptors were at baseline. Vertical lines indicate the location of the aneurysm neck.*

aneurysms, and for aneurysms with large (8.1 %) vs. small (6.2 %) NSI. The Wilcoxon rank-sum test revealed no significant differences ($p \leq 0.05$).

Table 4.2: *Experiment 2. Summary of error measurements for all 20 aneurysms and for aneurysms grouped by type, volume and NSI.*

	Error in $\overline{\text{WSS}}$[b]			CVRMSE[b]		
Cases[a]	Mean [%]	SE [%]	*p*-value	Mean [%]	SE [%]	*p*-value
All	4.3	0.4		7.1	0.7	
Terminal	4.7	0.6	0.50	8.4	1.2	0.26
Lateral	3.9	0.5		5.9	0.4	
Large volume	4.5	0.4	0.55	7.9	1.0	0.20
Small volume	4.1	0.7		6.4	0.9	
Large NSI	4.4	0.5	0.82	8.1	1.2	0.33
Small NSI	4.3	0.6		6.2	0.7	

[a] Per category, aneurysms were split in two groups of 10, e.g. 'Large volume' and 'Small volume' refer to subsets of 10 aneurysms with largest and smallest volume. NSI = nonsphericity index.
[b] $\overline{\text{WSS}}$ = space-averaged WSS; CVRMSE = coefficient of variation of the root-mean-square error; SE = standard error; *p*-values were calculated with the Wilcoxon rank-sum test.

4.3.3 Computational load

All simulations were run on a cluster with 64 processors (Intel Xeon X5355 2.66 GHz Quad Core) distributed over eight nodes, sharing 16 GB per node. In experiment 2, steady flow simulations were created on average 49 times faster than pulsatile flow simulations. In terms of wall-clock time, pulsatile flow simulations took on average 5 hours (range: 3 to 10 hours) and steady flow simulations took on average 6 minutes (range: 3 to 14 minutes).

4.4 Discussion

4.4.1 Contributions

This study has demonstrated that steady flow simulations can accurately approximate the TA WSS field of an aneurysm. Errors for the aneurysm's PS and ED WSS fields were considered too large, although the WSS distributions were similar. The similarities between steady and pulsatile flow simulations have been previously reported, but have never before been quantified for a large population. In summary, the main contributions of this study are: 1. WSS fields were compared node-by-node and both global and local errors were quantified, 2. the influence of the FRW imposed at the inlet was assessed by systematically varying the heart rate, pulsatility index, and TA flow rate, and 3. a large population of 22 cases was studied, including both terminal and lateral aneurysms, covering a large range of aneurysm volumes and NSIs.

4.4.2 Data interpretation

Despite the complexity of pulsatile flow in blood vessels and aneurysms, relatively small errors were found for the TA WSS field. The parent vessel segment's $\overline{\text{WSS}}$ waveform was

Table 4.3: *Experiment 2. Geometric and hemodynamic characteristics of all 20 aneurysms.*

	Geometry[a]			$\overline{\text{WSS}}$[b]			RMSE[c]	
Case	Type	V [mm^3]	NSI [-]	Pulsatile [Pa]	Steady [Pa]	ε [%]	RMSE [Pa]	CVRMSE [%]
1	T	1315	0.23	0.060	0.057	5.2	0.009	14.3
2	T	201	0.24	0.603	0.583	3.3	0.031	5.2
3	T	6	0.03	0.505	0.490	3.0	0.018	3.5
4	T	91	0.27	0.506	0.474	6.2	0.056	11.0
5	T	67	0.21	0.288	0.281	2.2	0.011	3.8
6	T	88	0.24	0.533	0.515	3.4	0.027	5.1
7	T	197	0.30	0.107	0.099	7.2	0.013	12.1
8	T	114	0.17	0.178	0.164	7.5	0.020	11.3
9	T	25	0.15	0.195	0.186	4.5	0.014	7.3
10	T	275	0.23	0.167	0.159	4.8	0.018	10.7
11	L	101	0.16	0.491	0.480	2.2	0.017	3.6
12	L	1122	0.26	0.054	0.052	4.0	0.004	7.4
13	L	175	0.32	1.120	1.081	3.5	0.053	4.7
14	L	106	0.16	0.095	0.089	6.1	0.007	7.8
15	L	72	0.09	6.755	6.683	1.1	0.309	4.6
16	L	12	0.10	2.438	2.316	5.0	0.142	5.8
17	L	288	0.25	2.033	1.953	3.9	0.132	6.5
18	L	147	0.20	0.365	0.351	4.0	0.023	6.2
19	L	163	0.18	0.193	0.183	5.3	0.013	6.5
20	L	674	0.19	0.448	0.429	4.2	0.025	5.6
mean						4.3		7.1
SE[d]						0.4		0.7

[a] T = terminal; L = lateral; V = volume; NSI = nonsphericity index.
[b] $\overline{\text{WSS}}$ = space-averaged WSS; ε = relative error.
[c] RMSE = root-mean-square error; CVRMSE = coefficient of variation of the RMSE.
[d] SE = standard error.

shifted in phase ahead of the FRW, and steady flow simulations underestimated PS $\overline{\text{WSS}}$ and overestimated ED $\overline{\text{WSS}}$. In contrast, the aneurysm's $\overline{\text{WSS}}$ waveform lagged behind the FRW, and steady flow simulations overestimated PS $\overline{\text{WSS}}$ and underestimated ED $\overline{\text{WSS}}$. This phase lag can be attributed to the inertia of the blood; it takes time for blood in the aneurysm to accelerate and decelerate in response to flow rate changes in the parent vessel. As a result, the PS and ED $\overline{\text{WSS}}$ fell short of reaching the $\overline{\text{WSS}}$ of the corresponding steady flow simulation.

Interestingly, TA $\overline{\text{WSS}}$ was slightly underestimated for all cases in this study. A hint to the explanation of this observation was offered by the series of 13 steady flow simulations of experiment 1. For both cases, we found a quadratic relationship between the flow rate into the aneurysm, which itself is linearly dependent on the flow rate at the inlet, and the aneurysm's $\overline{\text{WSS}}$ (second-order polynomial, coefficient of determination $R^2 > 0.999$). Although this analysis does not take into account the inertia effects, the quadratic relationship could explain the consistent underestimation of TA $\overline{\text{WSS}}$.

The approximation of the TA WSS field was for some aneurysms more accurate

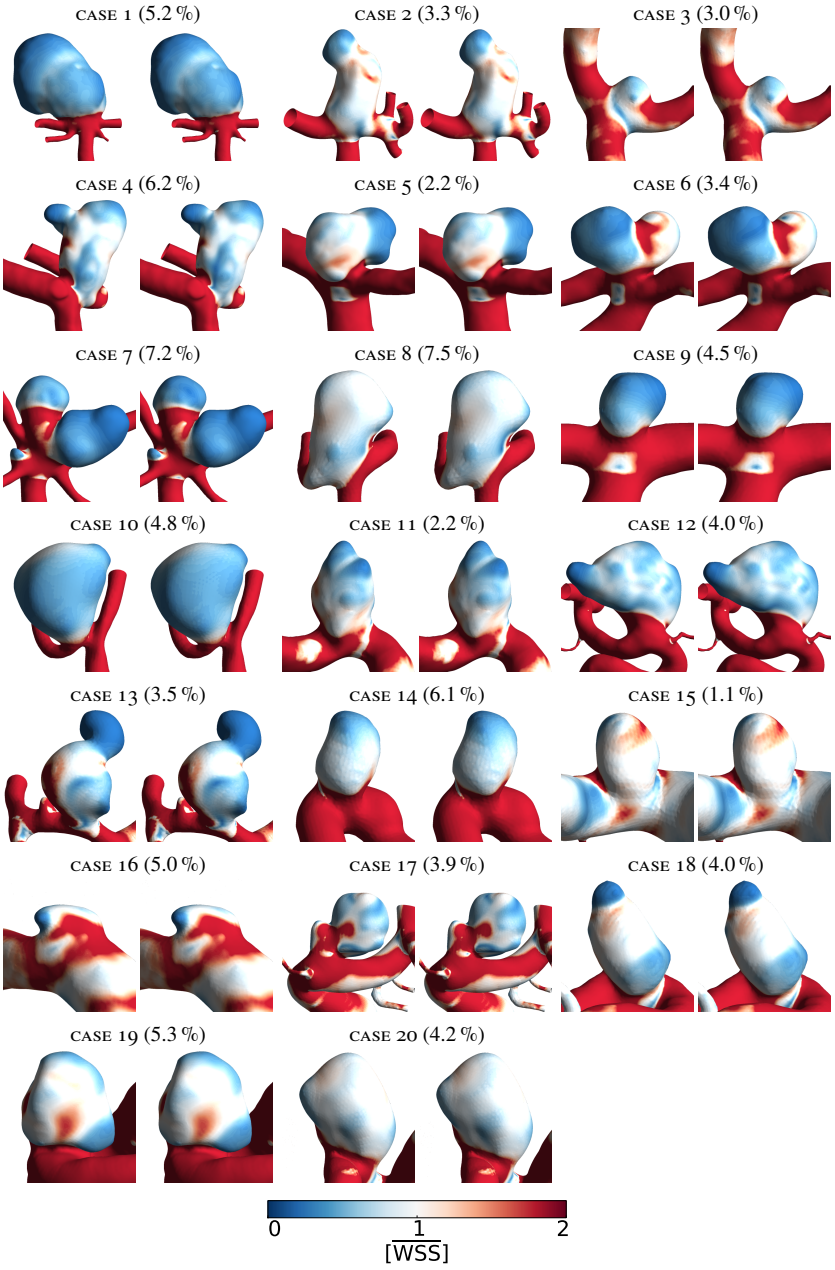

Figure 4.7: *Experiment 2. TA WSS field of the pulsatile (left) and steady (right) flow simulations. Colormaps were normalized by using* $\overline{\text{WSS}}$ *derived from the pulsatile flow simulation as unit. View points were selected to best visualize the aneurysm, so images are not necessarily at the same scale. The percentages in parentheses indicate the error in space-averaged WSS.*

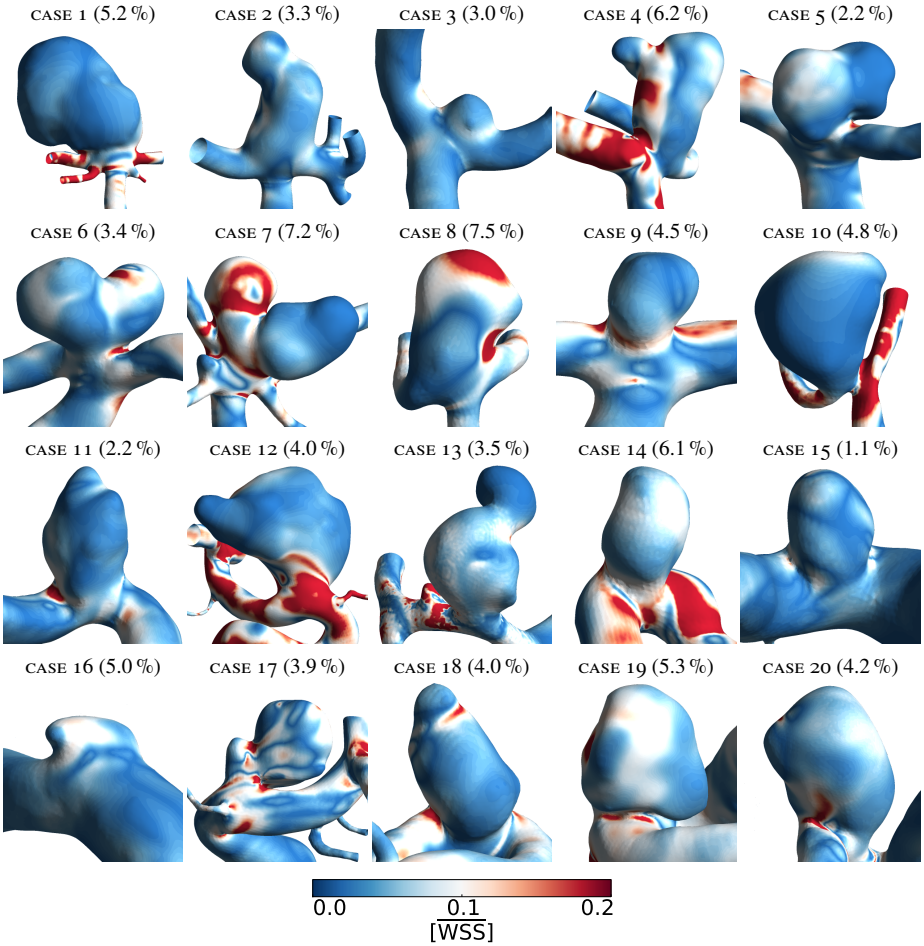

Figure 4.8: *Experiment 2. Absolute error of the TA WSS field calculated at each node of the surface mesh. Colormaps were normalized by using* $\overline{\text{WSS}}$ *derived from the pulsatile flow simulation as unit. View points were selected to best visualize the aneurysm, so images are not necessarily at the same scale. The percentages in parentheses indicate the error in space-averaged WSS.*

than for others. To gain more insight into when steady flow simulations can provide a better approximation, we related the error measurements to the aneurysm's geometry. As might be expected for this statistically small sample, Wilcoxon rank-sum test revealed no significant differences for the investigated geometric variables. However, we did observe a trend toward more accurate approximations for aneurysms that were lateral, small and/or spherical. Perhaps those aneurysms typically have simpler, more stable flow patterns, which are likely associated with smaller errors, whereas terminal, large and/or multilobular aneurysms may have more complex, unstable flow patterns.

4.4.3 Error in perspective

To put in perspective the 4.3 % error we found for TA $\overline{\text{WSS}}$ in experiment 2, we will compare it with the sensitivity of CFD simulations to two key parameters.

The first parameter is the vascular geometry. Failure to properly model the parent vessel has been reported to significantly influence the aneurysm's WSS field [28] and even small differences in the vascular geometry can sometimes cause substantial differences in flow structure [34]. Applying different levels of smoothing to the vascular model can lead to 18.0 % difference in $\overline{\text{WSS}}$ [69] and reconstructing the vascular model from either 3DRA or computed tomographic angiography (CTA) has been shown to give a mean difference in TA $\overline{\text{WSS}}$ of 44.2 % [71], which is one order of magnitude above the error reported in this work.

The second parameter is the inflow boundary condition. In experiment 1, the TA flow rate of the FRW was systematically varied 27 % above and below the baseline value. With respect to the baseline simulations, we found variations in TA $\overline{\text{WSS}}$ of up to 70 %, which confirms results from previous studies by Marzo et al. and Karmonik et al. [102, 129]. Bowker et al. found that even changes within the same patient from rest to exercise increases the TA $\overline{\text{WSS}}$ from 3 to 34 % [21]. In light of these uncertainties, the error with which steady flow simulations can approximate the TA WSS field is relatively small.

4.4.4 Value of steady flow simulations

As mentioned in the introduction, the majority of studies use pulsatile flow simulations to investigate the intra-aneurysmal hemodynamics. However, some studies have argued before that steady flow simulations could already provide useful information about the intra-aneurysmal hemodynamics, including the hemodynamic effect of stents [11, 91, 107], the relationship between the WSS and the biological response of the arterial wall [100, 185], and associations between hemodynamic variables and aneurysm rupture [42].The latter refers to a study of 210 aneurysms by Cebral et al., the largest on this topic to date, in which TA hemodynamic variables were compared between groups of ruptured and unruptured aneurysms. The analysis was repeated five times: twice with pulsatile flow simulations for different heart rates and three times with steady flow simulations under different inflow rate conditions. The authors found that associations between hemodynamic variables and rupture were mostly unaffected by the choice of simulation and concluded that steady flow simulations could be used to extract some hemodynamic variables related to rupture. Our findings suggest that also other studies linking WSS to rupture, such as the 119-aneurysm study by Xiang et al. or the 106-aneurysm study by Miura et al. [137, 209], could be reproduced using steady flow simulations.

The main motivation to use steady flow simulations is to reduce simulation time. In our study, it took on average 6 minutes on a cluster of 64 processor to compute the flow field for one case, nearly 50 times faster than computing the pulsatile equivalent. Even for a ruptured aneurysm that requires immediate treatment this might be fast enough for

use during interventional treatment planning [103]. Further speed-ups could be achieved by allowing higher convergence errors or changing meshing strategy [172]. Please note that the preparation of the CFD simulations is currently a manual process, which also requires significant amounts of time. However, efforts are underway to automate image segmentation [20], branch labeling [19], aneurysm detection [118], and aneurysm neck delineation [116]. This will further facilitate the introduction of CFD into clinical practice. An additional advantage of fast simulation times is that it allows for quick sweeping over input parameters [141], which could help estimate the propagation of uncertainty of, for instance, in- and outflow conditions.

4.4.5 Additional value of pulsatile flow simulations

Although the use of steady flow simulations is an attractive option to significantly reduce simulation times, we must stress that this approach may lead to loss of important information about the pulsatile flow field in the aneurysm. Previous studies have demonstrated the additional value of pulsatile flow simulations. For example, high resolution CFD simulations have revealed high frequency fluctuations in the aneurysm's flow field [16, 62, 189], which might be relevant to aneurysm rupture, and associations have been found between temporal variations of the WSS field and the formation and rupture of aneurysms [41, 127, 209]. In other words, steady flow simulations can be useful to quickly evaluate the aneurysm's flow field, but additional information can be extracted from the more realistic pulsatile flow simulations.

4.5 Conclusions

Steady flow simulations can accurately approximate the TA WSS field of an aneurysm. This has been demonstrated for both terminal and lateral aneurysms, covering a large range of aneurysm volumes and NSIs, and for a systematically varied FRW imposed at the inlet. In light of the sensitivity of hemodynamic simulations to uncertainties in vascular geometry and inflow boundary conditions, this approximation error can be considered negligible when studying associations between the TA WSS field and, for instance, aneurysm rupture. On a cluster of 64 processors, steady flow simulations were computed on average within 6 minutes, nearly 50 times faster than computing the pulsatile equivalent. Such fast computation times could help facilitate the introduction of CFD into clinical practice.

4.A Appendix: Analytical study of steady and pulsatile flow in a tube

This appendix considers viscous, incompressible flow of a Newtonian fluid. The Navier-Stokes equations that govern the motion of this fluid have analytical solutions for fully developed steady and pulsatile flow in a rigid tube with circular cross section [207]. Although the flow field in tortuous blood vessels and aneurysms is highly complex and can not be solved analytically, a deeper understanding of steady and pulsatile flow in arteries can be gained from studying these analytical solutions.

Let $Q(t)$ be a FRW with period T and Q_k its discretization in N real data points. The discrete Fourier transform gives Fourier coefficients $\hat{Q}_n \equiv \frac{1}{N} \sum_{k=0}^{N-1} Q_k \, e^{-2\pi i n k/N}$, such that

$$Q(t) \approx \sum_{n=0}^{N-1} \hat{Q}_n \, e^{i \omega_n t} \tag{4.4}$$

where ω_n is the angular frequency, given by

$$\omega_n = \begin{cases} 2\pi n/T & \text{if } n \leq N/2 \\ -2\pi (N-n)/T & \text{if } n > N/2 \end{cases}$$

For fully developed pulsatile flow in a tube, the velocity profile $v(r,t)$ is a function of radius r and time t alone [182], namely

$$v(r,t) = \frac{2\hat{Q}_0}{\pi R^2}\left[1 - \left(\frac{r}{R}\right)^2\right] + \sum_{n=1}^{N-1} \frac{\hat{Q}_n}{\pi R^2}\left[\frac{1 - \frac{J_0(\beta_n \frac{r}{R})}{J_0(\beta_n)}}{1 - \frac{2J_1(\beta_n)}{\beta_n J_0(\beta_n)}}\right] e^{i \omega_n t} \tag{4.5}$$

where R is the tube's radius, J_0 and J_1 are Bessel functions of the first kind, and $\beta_n = i^{3/2} \alpha_n$ with $\alpha_n = R\sqrt{\omega_n \rho/\mu}$. Note that α_1 is the Womersley number. The corresponding WSS $\tau_w(t)$ is given by

$$\begin{aligned} \tau_w(t) &= -\mu \left(\frac{\partial v}{\partial r}\right)_{r=R} \\ &= \frac{4\mu \hat{Q}_0}{\pi R^3} - \sum_{n=1}^{N-1} \frac{\mu \beta_n \hat{Q}_n}{\pi R^3}\left[\frac{\frac{J_1(\beta_n)}{J_0(\beta_n)}}{1 - \frac{2J_1(\beta_n)}{\beta_n J_0(\beta_n)}}\right] e^{i \omega_n t} \end{aligned} \tag{4.6}$$

The equations describing pulsatile flow in a tube are linear in both velocity and pressure and can therefore be split in a steady and an oscillatory part [210]. The steady part is represented by the first term in Eqs. (4.4)-(4.6) and describes a constant forward flow with TA flow rate $\hat{Q}_0$ and a parabolic velocity profile. The oscillatory is represented by the rest of the terms and describes the back and forth motion of the fluid, which produces zero net flow over the cardiac cycle.

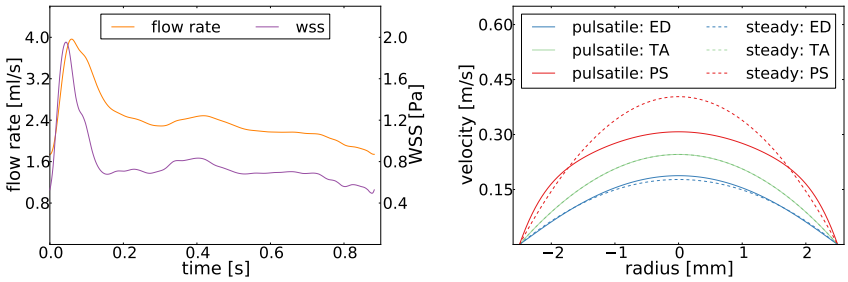

Figure 4.9: *Analytical solution of steady and pulsatile flow in a tube. (left) FRW with all three descriptors at baseline and corresponding WSS waveform. (right) Velocity profiles corresponding to TA, PS, and ED WSS.*

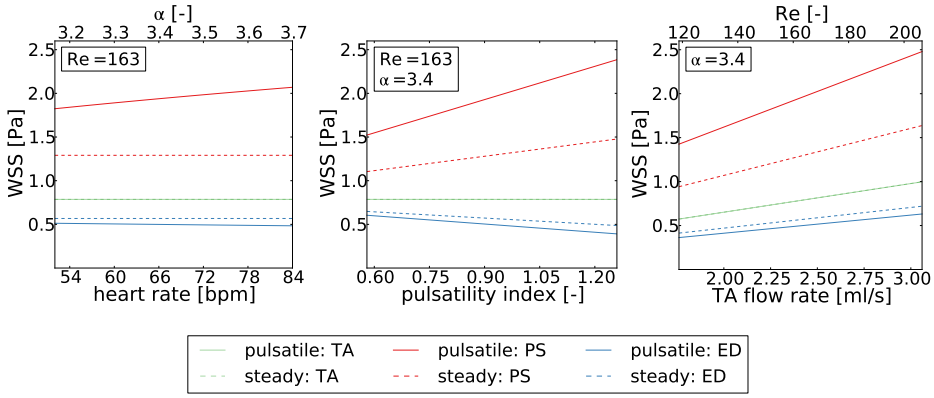

Figure 4.10: *Analytical solution of pulsatile and steady flow in a tube. TA, PS, and ED WSS as function of the three FRW descriptors.*

The Womersley number characterizes the pulsatile flow field. For low Womersley numbers (< 1), the oscillatory part of $v(r,t)$ describes an approximately parabolic velocity profile and the flow field can be considered quasi-steady. For physiological Womersley numbers (~ 3), however, the oscillatory part of $v(r,t)$, and therefore $v(r,t)$ itself, noticeably deviates from a parabolic profile. Especially around PS, during which the blood experiences a relatively large acceleration, inertial forces dominate viscous forces and the velocity profile is more plug-like. As a result, maximum or PS WSS in pulsatile flow is higher than the WSS in steady flow under maximum flow rate conditions and, similarly, minimum or ED WSS in pulsatile flow is lower than the WSS in steady flow under minimum flow rate conditions. TA WSS in pulsatile flow is equal to the WSS in steady flow under TA flow rate conditions given that all but the first term in Eqs. (4.4)-(4.6) vanish when integrated over the cardiac cycle.

To illustrate the difference in WSS between steady and pulsatile flow, we calculated $v(r,t)$ and $\tau_w(t)$ for a tube with a radius of 2.5 mm, which is the typical radius of an ICA [33], and blood with a density of 1060 kg/m^3 and a viscosity of 4 mPa s. The effect of

FRW descriptors on the difference was assessed by fixing two descriptors at baseline and varying the third from lower to upper value as specified in Table 4.1.

Figure 4.9 shows the FRW with all three descriptors at baseline and the corresponding WSS waveform. A phase shift of the WSS waveform ahead of the FRW can be clearly observed at PS. The figure also shows the pulsatile velocity profiles corresponding to TA, PS, and ED WSS. They are shown together with parabolic velocity profiles of steady flow under TA, PS, and ED flow rate conditions.

Figure 4.10 shows the TA, PS, and ED WSS as function of each of the three FRW descriptors. As mentioned before, TA WSS is equal, PS WSS is lower and ED WSS is higher in steady than in pulsatile flow. In terms of the relative difference with respect to the WSS in pulsatile flow: for increasing heart rate, the difference in PS WSS increased from 29.2 to 37.6 % and the difference in ED WSS increased from 10.7 to 17.3 %; for increasing pulsatility index, the difference in PS WSS increased from 27.5 to 38.1 % and the difference in ED WSS increased from 7.3 to 24.4 %; and for all TA flow rates, the difference in PS WSS was constant at 33.9 % and the difference in ED WSS was constant at 14.0 %.

5

Hemodynamic stress at the aneurysm initiation site

Abstract — The aim of our study was to analyze the wall shear stress (WSS) field at the aneurysm initiation site. Ten cases with aneurysms were analyzed and compared with ten controls. All included aneurysms were from a single location, which was neither a bifurcation apex nor the outer wall of a vascular bend. Aneurysms were virtually removed from the vascular models of the cases to mimic the pre-aneurysm geometry. Computational fluid dynamics simulations were created to assess the magnitude, gradient, multidirectionality, and pulsatility of the WSS. Tests were performed to assess the sensitivity of the computed WSS field to the observer virtually removing the aneurysm and to the flow rate imposed at the inlet. To aid the inter-subject comparison of hemodynamic variables, we mapped the branch surfaces onto a two-dimensional parametric space. This approach made it possible to view the whole branch at once for qualitative evaluation. It also allowed us to define a patch for quantitative analysis, which was consistent among subjects and encapsulated all aneurysm initiation sites. This patch was characterized by high time-averaged WSS magnitude (TAWSS) and high TAWSS gradients. The aneurysm initiation site partly overlapped with high TAWSS regions and, among all assessed variables, most consistently coincided with peaks of WSS pulsatility.

Adapted from: Geers AJ, Morales HG, Larrabide I, Butakoff C, Frangi AF. *Wall shear stress at the aneurysm initiation site.* [Prepared for submission]

5.1 Introduction

Cerebral aneurysms are localized, pathological dilatations of cerebral arteries. Their rupture causes subarachnoid hemorrhage and is associated with high rates of morbidity and mortality [83]. Better understanding of the mechanisms underlying aneurysm initiation is crucial for the development of new preventive and therapeutic strategies [90].

While systemic risk factors such as hypertension and connective tissue disorders may weaken the cerebral arteries' ability to maintain homeostasis, hemodynamic stresses appear to be necessary triggers for the pathological remodeling leading to aneurysm formation [53, 64, 133, 143, 148, 162, 173, 186]. In vivo measurements of these stresses are limited by the low spatial and temporal resolution of current imaging techniques [128] and the rarity of imaging a patient prior to aneurysm formation. Instead, computational fluid dynamics (CFD) techniques have been employed to simulate the hemodynamics in vascular geometries with the aneurysm virtually removed to approximate the pre-aneurysm condition [15, 29, 46, 60, 110, 117, 127, 169, 171] and in vascular geometries derived from rare pre-aneurysm images [52, 109, 110, 113]. CFD simulations have also been used to complement histological analyses of aneurysm formation in animal models [134, 135].

Hemodynamic studies have strongly focused on wall shear stress (WSS), which is a key regulator of vascular biology and pathology [53]. In line with the observation that aneurysms predominantly occur at high WSS regions such as bifurcation apices or outer walls of vascular bends [2, 3, 108, 151], many studies have found correlations between the aneurysm initiation site and high WSS [29, 46, 171], especially in combination with high positive WSS gradients (WSSG) [109, 110, 113, 134, 135]. Other studies have found correlations with low WSS [52, 127], WSS patterns involving both high and low WSS [15, 117], or indices describing the oscillatory nature of the WSS and WSSG [46, 60, 127, 169]. These apparent inconsistencies among CFD-based studies can be attributed to the small datasets, variety of aneurysm locations, and subjectivity of data analyses, as pointed out by Chen et al. [46], but also to missing patient-specific information about boundary conditions and properties of the arterial wall.

The aim of our study was to analyze the WSS field at the aneurysm initiation site. All included aneurysms were from a single location, which was neither a bifurcation apex nor the outer wall of a vascular bend. Vascular geometries with the aneurysm removed were matched by controls that never formed an aneurysm at that particular location, but elsewhere. To standardize the data analysis and simplify the comparison of cases, branches of interest were mapped onto the same parametric space. Tests were performed to measure the sensitivity of the computed WSS field to the observer virtually removing the aneurysm and to the flow rate imposed at the inlet.

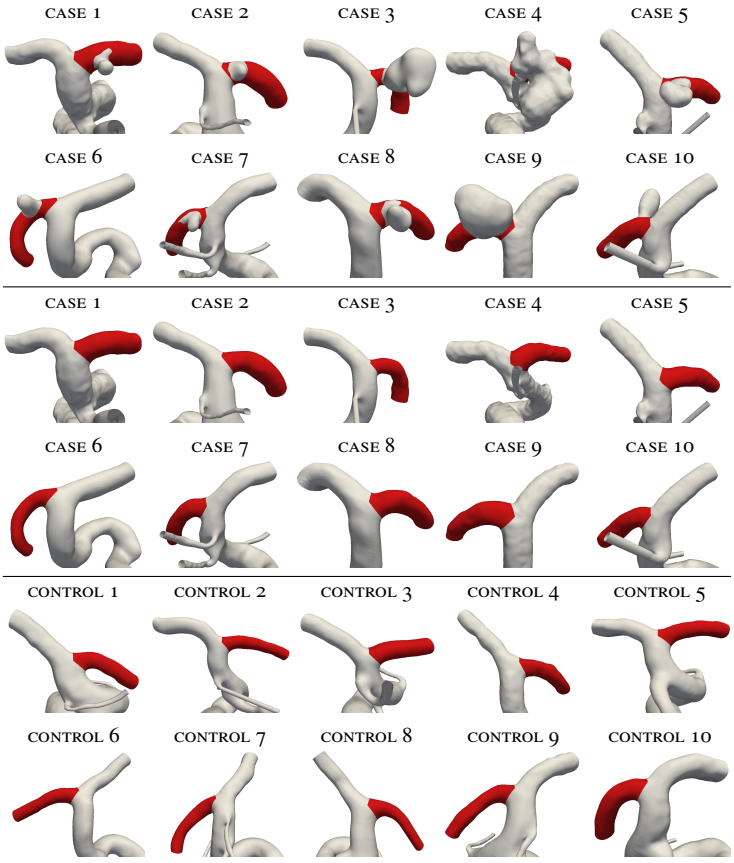

Figure 5.1: *Vascular models of cases with aneurysm (top), cases with the aneurysm virtually removed (middle), and controls (bottom). The ACA is colored red. View points were selected to best visualize the vascular model, so images are not necessarily at the same scale.*

5.2 Methods

5.2.1 Case selection

Twenty patients, ten cases and ten controls, were drawn from a large multicenter database created within the EU project @neurIST [198]. The cases were all the patients in the database with an aneurysm on the A1 segment of the anterior cerebral artery (ACA-A1). They were selected because of their remarkable consistency in aneurysm location: all aneurysms were just distal to the internal carotid artery (ICA) bifurcation with nine cases directed posteriorly and one case directed anteriorly (case 10). Moreover, the location was neither a bifurcation apex nor the outer wall of a vascular bend, which – attributed to being high WSS regions – are the most common aneurysm locations [2, 3, 108, 151]. The controls were patients with an aneurysm at the middle cerebral artery (MCA) bifurcation, hence

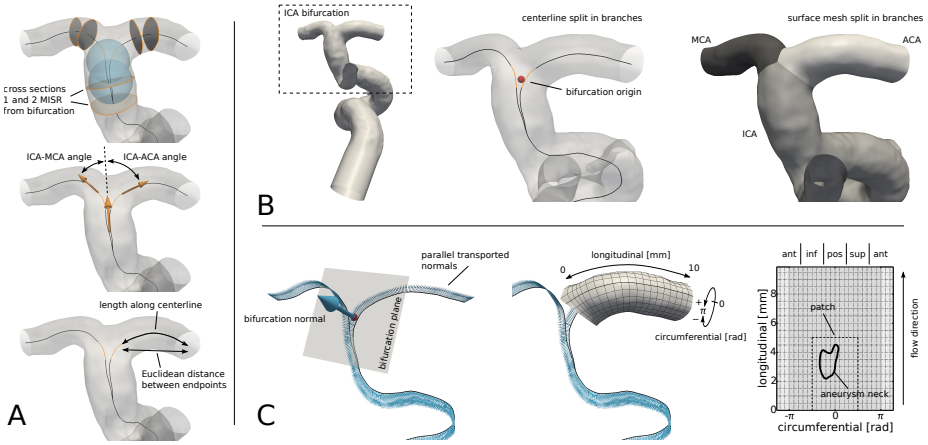

Figure 5.2: *Post-processing steps. A. Bifurcation sections were created one and two maximally inscribed sphere radii (MISR) away from the bifurcation to obtain representative cross sectional areas for the ICA, ACA and MCA. Bifurcation vectors projected onto the bifurcation plane (see panel C) were used to calculate the bifurcation angles. The tortuosity was defined by Eq.* (5.7) *using the branch length along the centerline and the Euclidean distance between its endpoints. B. Centerlines from inlet to ACA outlet and inlet to MCA outlet diverged at the ICA bifurcation and were split into branches. Correspondingly, the vessel wall surface was also split into branches. C. The posteriorly directed normal to the bifurcation plane was parallel transported along the centerline. The ACA was mapped onto a 2D parametric space with a longitudinal and a circumferential coordinate. To view the distribution of hemodynamic variables on the whole branch at once, it was flattened onto a rectangle. Plots of the flattened branch indicate the location of the aneurysm neck and the patch. They also indicate the location of the posterior (pos), anterior (ant), superior (sup) and inferior (inf) sides of the branch. The plot range of the circumferential coordinate was slightly extended to show the continuity of the variable distribution. Duplicated regions were grayed out.*

predisposed to having aneurysms, that did not form an aneurysm at the same location as the cases. They were selected to match cases by patient age (within 2 years) and aneurysm hemisphere (left or right). No other information was considered during the selection process.

5.2.2 Vascular modeling

Patient-specific vascular models, represented by triangular surface meshes, were constructed by segmenting three-dimensional rotational angiography (3DRA) images using a geodesic active regions approach [20]. The ophthalmic artery, anterior choroidal artery and posterior communicating artery branching off the ICA were preserved if successfully segmented. Touching vessels were removed. Models were smoothed using a geometry-preserving smoothing algorithm [142]. To ensure consistency in the extent of the vascular models, inlet and outlet branches were clipped at the same location for all cases and

controls. Inlet branches were clipped at a manually selected location at the start of the cavernous segment of the ICA and then extruded 10 mm to allow for flow to develop. Outlet branches were automatically clipped 10 mm from their proximal bifurcation; those shorter than 10 mm were first extruded. The ACA had to be extruded only for control 6. Figure 5.1 shows the vascular models of all cases and controls.

Aneurysms were virtually removed from the vascular models of the cases to mimic the pre-aneurysm geometry (Figure 5.1). Triangle removal and hole filling operations were iteratively applied to reconstruct the ACA without aneurysm. Subsequently, the vascular model was smoothed and inlet and outlet branches were clipped as described in the previous paragraph. To assess the sensitivity of the computed WSS field to this manual procedure, two observers independently removed the aneurysm for all cases.

The automatic selection of outlet locations made use of centerlines and bifurcation origins generated with the Vascular Modeling Toolkit (VMTK) [5, 152]. Manual mesh editing operations were performed in @neuFuse (B3C, Bologna, Italy) [198], a software application developed within @neurIST.

5.2.3 Blood flow modeling

Unstructured volumetric meshes were created with ICEM CFD 13.0 (ANSYS, Canonsburg, PA, USA) using an octree approach. Meshes were composed of tetrahedral elements with a side length of 0.2 mm and three prism layers with a total height of 0.07 mm and a side length of 0.1 mm. The total number of elements ranged from 2.3 to 6.7 million, the density from 3124 to 4076 elements per mm^3, depending on the surface-area-to-volume ratio of the computational domain. This mesh resolution was chosen following previously performed mesh dependency tests [70].

CFD simulations were created with CFX 13.0 (ANSYS), which is a commercial vertex-centered finite volume solver. We used a second-order advection scheme and a second-order backward Euler transient scheme. Solutions converged until the normalized residual of the WSS everywhere in the computational domain was $< 5 \times 10^{-4}$.

Blood was modeled as an incompressible Newtonian fluid with density $\rho = 1060\,kg/m^3$ and viscosity $\mu = 4\,mPa\,s$. Although blood is a non-Newtonian fluid, assuming constant viscosity is appropriate for our problem [139]. Vessel walls were assumed rigid with a no-slip boundary condition. A parabolic velocity profile was imposed at the inlet. Since patient-specific flow information was unavailable, we estimated the flow rate waveform at the inlet and imposed zero-pressure boundary conditions at all outlets. The shape of the flow rate waveform was obtained from Ford et al. who averaged the waveform shapes of 17 young, normal volunteers [59]. The time-averaged flow rate, Q, was obtained using the relationship from Cebral et al.: $Q = 48.21\,A^{1.84}\,T^{-1}$ where Q is in ml/s, A is the inlet's cross-sectional area in cm^2, and T is the period of the cardiac cycle in s. This relationship was obtained by fitting a power-law function through measurements of Q and A of the ICAs and vertebral arteries of 11 normal volunteers [33]. Reynolds numbers at the inlets ranged from 62 to 441 with an average of 152.

To assess the sensitivity of the computed WSS field to boundary conditions, we repeated the simulations for all cases and controls with a 20 % higher flow rate at the inlet. The cardiac cycle was discretized in 200 uniformly distributed time steps and, to reduce the effect of initial transients, the second of two simulated cardiac cycles was analyzed. These settings were chosen following previously performed time step and cycle dependency tests [70].

A total of 50 CFD simulations were created: 10 cases and 10 controls under 'normal' inflow conditions, 10 cases and 10 controls under 'high' inflow conditions, and 10 cases under 'normal' inflow conditions with the aneurysm removed by the second observer.

5.2.4 Hemodynamic variables

As mentioned in the Introduction (Section 5.1), different aspects of the WSS field are deemed relevant to the initiation of aneurysms. Specifically, we assessed the magnitude, gradient, multidirectionality, and pulsatility of the WSS, according to the definitions below.

Given WSS vector $\boldsymbol{\tau}_w = \boldsymbol{\tau}_w(\boldsymbol{x}, t)$ at surface point $\boldsymbol{x}$ and time t, the time-averaged WSS magnitude (TAWSS) is defined as

$$\mathrm{TAWSS} = \frac{1}{T}\int_0^T |\boldsymbol{\tau}_w| \, \mathrm{d}t \tag{5.1}$$

where T is the period of the cardiac cycle.

For use in the definition of other WSS-related variables, we defined unit vectors in the direction of and perpendicular to the time-averaged WSS vector, respectively $\hat{\boldsymbol{p}}$ and $\hat{\boldsymbol{q}}$, as

$$\hat{\boldsymbol{p}} = \frac{\int_0^T \boldsymbol{\tau}_w \, \mathrm{d}t}{\left|\int_0^T \boldsymbol{\tau}_w \, \mathrm{d}t\right|}, \qquad \hat{\boldsymbol{q}} = \hat{\boldsymbol{p}} \times \hat{\boldsymbol{n}} \tag{5.2}$$

where $\hat{\boldsymbol{n}}$ is the surface normal.

For the gradient of TAWSS (TAWSSG), we used the definition proposed by Meng and colleagues [53, 185], which differentiates between positive and negative gradients with respect to $\hat{\boldsymbol{p}}$, namely,

$$\mathrm{TAWSSG} = \nabla_S(\mathrm{TAWSS}) \cdot \hat{\boldsymbol{p}} \tag{5.3}$$

where ∇_S is the gradient on the vessel wall surface.

Throughout the cardiac cycle, the WSS vector may change direction and not remain parallel to $\hat{\boldsymbol{p}}$. The changing WSS direction is associated with the concept of 'disturbed' flow. To quantify the multidirectionality of disturbed flow, we used the transverse WSS (transWSS), which was recently proposed by Peiffer et al. in the context of atherosclerosis [146]. The transWSS is defined as the time-averaged absolute value of the q-component of the WSS vector, that is,

$$\mathrm{transWSS} = \frac{1}{T}\int_0^T |\boldsymbol{\tau}_w \cdot \hat{\boldsymbol{q}}| \, \mathrm{d}t \tag{5.4}$$

We quantified the temporal variation of the WSS magnitude during the cardiac cycle by calculating the WSS pulsatility index (WSSPI) [73], given by

$$\text{WSSPI} = \frac{\max\limits_{t\in[0,T]} \boldsymbol{\tau}_w - \min\limits_{t\in[0,T]} \boldsymbol{\tau}_w}{\text{TAWSS}} \tag{5.5}$$

As WSS magnitudes may vary substantially between CFD simulations using either patient-specific or estimated boundary conditions, caution is advised when interpreting them [92, 102, 129, 131]. Instead, we chose to focus on the WSS distribution by normalizing TAWSS by the space-averaged TAWSS on the branch ($\overline{\text{TAWSS}}_\text{B}$). For aneurysms, normalized WSS distributions have been shown to remain relatively unchanged across different physiological boundary conditions [129]. TAWSSG and transWSS were similarly normalized by $\overline{\text{TAWSS}}_\text{B}$. Unless stated otherwise, results in this chapter refer to the normalized TAWSS, TAWSSG and transWSS.

5.2.5 Geometric variables

Vascular geometry has a major impact on hemodynamics [71]. To complement the hemodynamic analysis in our study, we characterized the vascular geometry using the framework presented by Piccinelli et al. [152], which is available as part of VMTK. We will briefly outline the procedure. Some of the processing steps are illustrated in Figure 5.2. For more details, refer to [152].

Two centerlines were created: one from the inlet to the MCA outlet and another from the inlet to the ACA outlet. At the ICA bifurcation, the two centerlines diverged into their respective branches and the corresponding bifurcation origin and plane were identified. The normal to the bifurcation plane was set to point posteriorly. Centerlines were split into branches corresponding to the ICA, MCA and ACA.

For each branch, a representative cross sectional area A was defined as the mean surface area of two cross sections. These two sections were created one and two maximally inscribed sphere radii away from the bifurcation. The bifurcation's area ratio [88] was given by

$$\text{area ratio} = \frac{A_\text{ACA} + A_\text{MCA}}{A_\text{ICA}} \tag{5.6}$$

Vectors pointing in the direction of the branches were created and then projected onto the bifurcation plane. The in-plane ICA-ACA and ICA-MCA angles were calculated.

To quantify the tortuosity of the ACA, we used the definition

$$\text{tortuosity} = \frac{L}{D} - 1 \tag{5.7}$$

where L is the length along the centerline and D is the Euclidean distance between its endpoints.

5.2.6 Branch extraction and parametrization

To aid the inter-subject comparison of hemodynamic variables on the surface of the ACA, we used the approach proposed by Antiga et al. [6], which is also available as part of VMTK. Briefly, the vessel wall surface was split into branches corresponding to the previously split centerlines (Figure 5.2). As branches are topologically equivalent to cylinders, the ACA could be mapped onto a two-dimensional (2D) parametric space with a longitudinal coordinate, u, and a periodic circumferential coordinate, v. Coordinate u ranged from 0 to 10 mm, increasing in the direction of the flow. Coordinate v ranged from $-\pi$ to π rad. The position of $v = 0$ was determined by the bifurcation normal parallel transported along the centerline and $v > 0$ was set to correspond to the superior side of the ACA.

5.2.7 Data visualization

Contour plots were created to visualize the distribution of hemodynamic variables on the surface of the ACA. Using the 2D parametrization, the branch surface was flattened onto a rectangle such that u and v corresponded to the vertical and horizontal axes of the plots, respectively (Figure 5.2). This approach made it possible to view the whole branch at once and more easily compare between subjects. Because the circumferential coordinate is periodic, we slightly extended the plot to range from -4 to 4 rad, thus maintaining the visual continuity of the variable distributions. To indicate the location of the aneurysm neck, we calculated the distance from the surface with aneurysm to the surface without aneurysm and plotted a contour line at 0.1 mm. The region enclosed by the aneurysm neck will be referred to as 'aneurysm initiation site'.

5.2.8 Statistical analysis

In this study, we assessed the sensitivity of the computed WSS field to the observer virtually removing the aneurysm and to the flow rate imposed at the inlet. Differences between solutions were quantified by calculating the root-mean-square deviation (RMSD) between TAWSS fields, after linearly interpolating them onto a uniformly remeshed branch surface with a nominal node spacing of 0.05 mm. Solutions of observer 2 were projected onto the remeshed branch surface of observer 1. Since normalized TAWSS fields were considered, for which $\overline{\mathrm{TAWSS}}_{\mathrm{B}} = 1$, the RMSD was equal to the coefficient of variation of the RMSD (CVRMSD). CVRMSD will be expressed as a percentage.

Space-averaged values of variables were calculated for quantitative analysis. Besides analyzing the whole branch, we defined a 'patch' that encapsulated all aneurysm initiation sites. This patch was bound by $u \in [0, 5]$ and $v \in [-\pi/2\ , \pi/2\,]$, see Figure 5.2. For case 10, with the aneurysm directed anteriorly, and its matching control, the patch was defined at the opposite side of the branch, bound by $u \in [0, 5]$ and $v \in [-\pi, -\pi/2\,) \cup (\pi/2\ , \pi]$. Variables were averaged over the branch, patch and non-patch (branch minus patch).

Table 5.1: *Statistical analysis of geometric variables.*

		Mean and standard error		
Variable	Unit	Cases	Controls	p-value[a]
ICA-ACA angle	[°]	77.8 ± 2.7	77.8 ± 3.1	.880
ICA-MCA angle	[°]	40.3 ± 2.5	39.4 ± 3.0	.940
ICA cross sectional area	[mm^2]	10.7 ± 0.8	9.5 ± 1.0	.364
ACA cross sectional area	[mm^2]	5.2 ± 0.6	3.8 ± 0.3	.059
MCA cross sectional area	[mm^2]	6.0 ± 0.3	5.1 ± 0.3	**.049**
ICA bifurcation area ratio	[-]	1.05 ± 0.05	0.98 ± 0.05	.545
ACA tortuosity	[-]	0.12 ± 0.03	0.06 ± 0.01	.059

[a] p-values were calculated with the Wilcoxon rank-sum test; values highlighted in bold face correspond to statistically significant differences with $p < 0.05$.

Table 5.2: *Statistical analysis of hemodynamic variables.*

		Mean and standard error of space-averaged variable values									
		Cases			Controls			p-value[b]			
Variable	Unit	Patch	Non-patch	Branch	Patch	Non-patch	Branch	I	II	III	IV
TAWSS	[$\overline{\text{TAWSS}}_B$]	1.18±0.05	0.94±0.02	1.00±0.00	1.01±0.05	1.00±0.02	1.00±0.00	**.022**	.959	**.034**	1.00
TAWSSG[a]	[$\overline{\text{TAWSS}}_B$/mm]	0.53±0.05	0.34±0.02	0.39±0.02	0.35±0.03	0.26±0.02	0.28±0.02	**.017**	**.013**	**.010**	**.003**
transWSS	[10^{-3} $\overline{\text{TAWSS}}_B$]	42.7±3.9	26.1±3.0	30.4±2.7	31.4±3.2	21.4±1.1	23.7±1.3	**.007**	**.005**	.059	**.028**
WSSPI	[-]	1.52±0.03	1.38±0.03	1.41±0.03	1.45±0.02	1.27±0.02	1.32±0.02	**.005**	**.005**	.082	**.003**

[a] TAWSSG differentiates between positive and negative gradients, so we space-averaged the absolute TAWSSG.

[b] p-values were calculated with the Wilcoxon rank-sum test; the following samples were compared: I. patch vs. non-patch for the cases (paired), II. patch vs. non-patch for the controls (paired), III. patches of the cases vs. patches of the controls (unpaired), and IV. branches of the cases vs. branches of the controls (unpaired); values highlighted in bold face correspond to statistically significant differences with $p < 0.05$.

To test the significance of the differences between regions and between cases and controls, we used the Wilcoxon signed-rank test for paired samples and the Wilcoxon rank-sum test for unpaired samples. Differences were considered statistically significant for $p < 0.05$. The following samples were compared: I. patch vs. non-patch for the cases (paired), II. patch vs. non-patch for the controls (paired), III. patches of the cases vs. patches of the controls (unpaired), and IV. branches of the cases vs. branches of the controls (unpaired).

The Wilcoxon rank-sum test was also used to compare geometric variables between cases and controls. Again, differences were considered statistically significant for $p < 0.05$.

5.3 Results

5.3.1 Geometry

As mentioned in Section 5.2.1, we found a remarkable consistency in location among the ACA aneurysms in the @neurIST database. This observation was confirmed by the consistent location of the aneurysm initiation sites in the contour plots, see Figure 5.3. For cases 1 to 9, the circumferential coordinate of the center of the initiation site was on

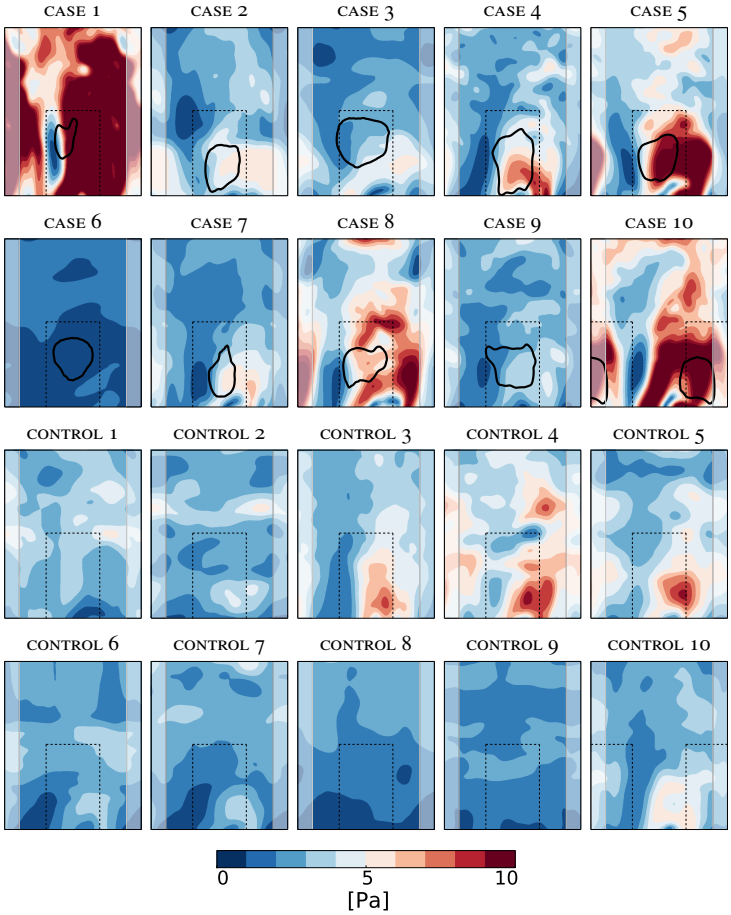

Figure 5.3: *Time-averaged WSS (TAWSS) under 'normal' inflow conditions. The same colormap range was used for all cases and controls. Plot properties are explained in Figure 5.2C.*

average 2° (range: −24 to 13°). For case 10, it was 119°. In other words, most aneurysms were approximately aligned with the transported bifurcation normal.

Table 5.1 reports on the statistical analysis of geometric variables. Bifurcation angles were very similar among cases and controls. Cross sectional areas of branches tended to be larger for cases, but only for the MCA branch these differences were statistically significant. Area ratios were not significantly different. The tortuosity of ACAs showed a non-significant trend of being larger for cases than for controls.

5.3.2 Hemodynamics

Figure 5.3 shows for all cases and controls the non-normalized TAWSS on the ACA. There were large variations in space-averaged TAWSS with values ranging from 1.0 to 11.2 Pa

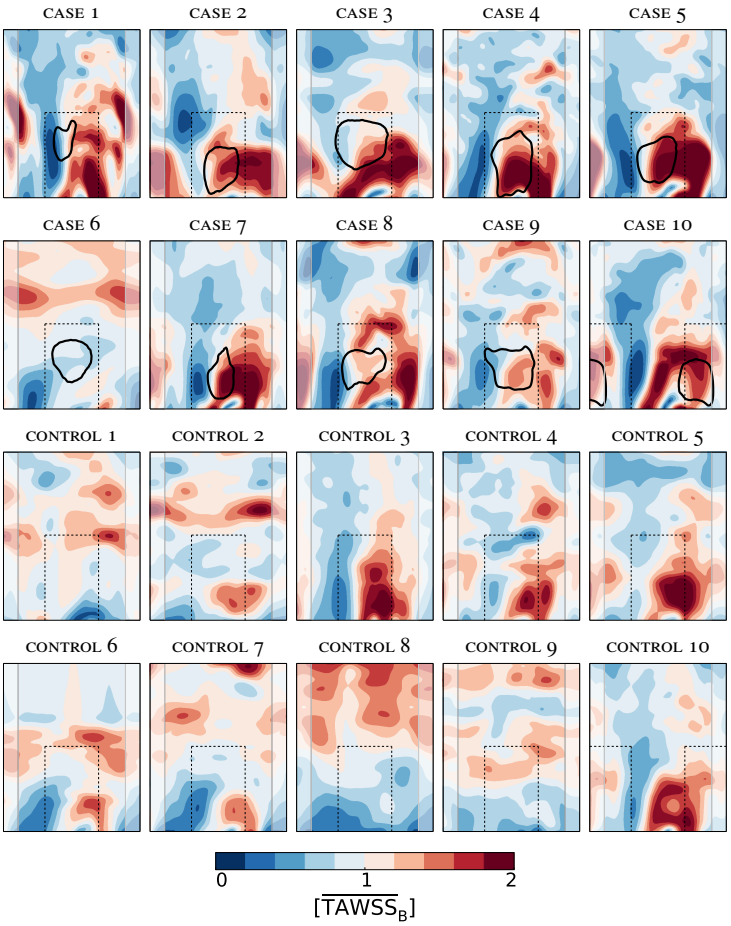

Figure 5.4: *Time-averaged WSS (TAWSS) under 'normal' inflow conditions. Colormaps were normalized by using* $\overline{\text{TAWSS}}_{\text{B}}$ *as unit. Plot properties are explained in Figure 5.2C.*

(mean: 3.5 Pa; standard deviation: 2.2 Pa). Figure 5.4 shows the normalized TAWSS, highlighting the distribution rather than the magnitude. Overall, cases appeared to have a larger spatial variation of TAWSS, covering a wider range of TAWSS values. Close to the apex of the bifurcation and on the superior side of the ACA (see Figure 5.2), TAWSS was relatively high for cases. However, some controls showed similar patterns, e.g. control 3 and control 5, whereas some cases, e.g. case 6, did not. Aneurysm initiation sites partly overlapped with regions of high TAWSS, yet tended to be near the edge of them. Statistical analysis (see Table 5.2) revealed no significant differences between the patch and the rest of the branch (non-patch) for controls, but did show significant differences between those regions for cases. Also, patches of cases experienced significantly higher TAWSS than those of controls. By definition, normalization removed differences in TAWSS between branches.

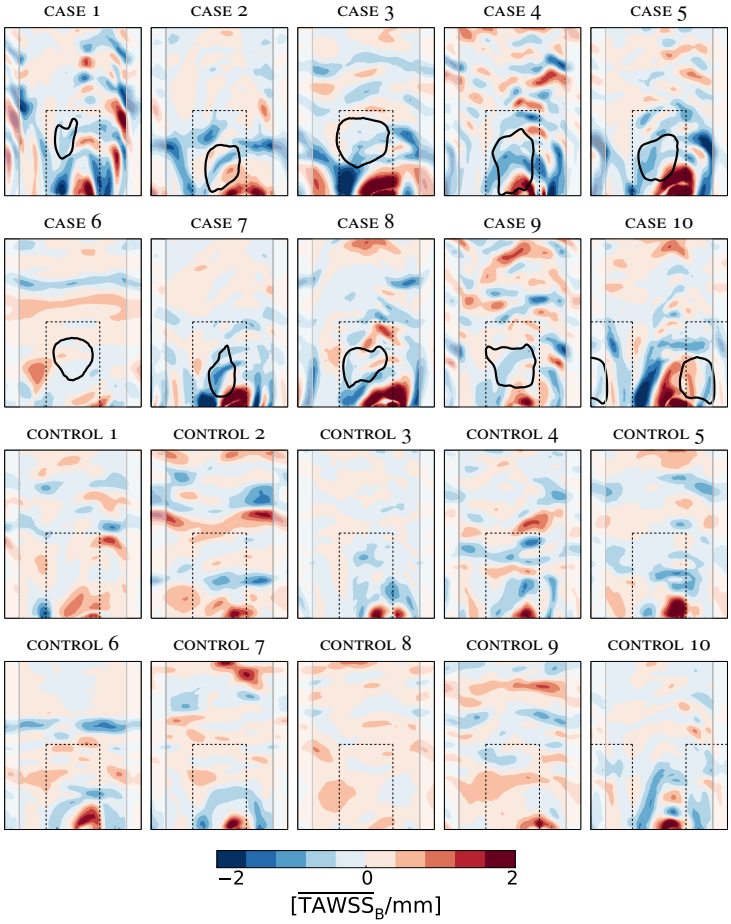

Figure 5.5: *Gradient of the time-averaged WSS (TAWSSG) under 'normal' inflow conditions. Colormaps were normalized by using* $\overline{\text{TAWSS}}_B$/mm *as unit. Plot properties are explained in Figure 5.2C.*

Figure 5.5 shows the distribution of TAWSSG. Cases' larger spatial variation of TAWSS was reflected by higher positive and negative gradients. Correspondingly, the absolute value of TAWSSG was significantly higher, both for the whole branch and for the patch. Although magnitudes varied, distributions were found to be similar for cases and controls: patches experienced significantly higher absolute TAWSSG than the rest of the branch. However, there was no clear correlation between either positive or negative gradients and the aneurysm initiation site.

Figure 5.6 shows the distribution of transWSS. Concentrated regions of high transWSS could be observed, suggesting that flow disturbances remained in the same location throughout the cardiac cycle. As expected, WSS vectors changed direction more strongly closer to the ICA bifurcation. For both cases and controls, patches had significantly higher

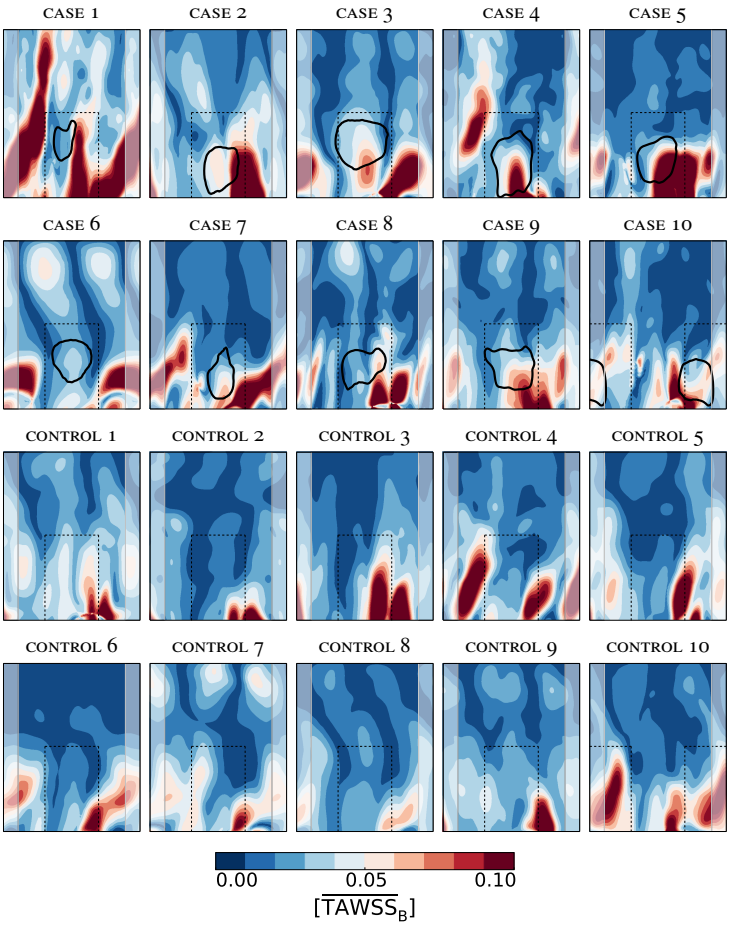

Figure 5.6: *Transverse WSS (transWSS) under 'normal' inflow conditions. Colormaps were normalized by using* $\overline{\text{TAWSS}}_B$ *as unit. Plot properties are explained in Figure 5.2C.*

transWSS than non-patches. On average, transWSS was higher for cases than controls, but only for the whole branch these differences were significant. No clear correlations were found between regions of high transWSS and the aneurysm initiation site.

Animations of the WSS field during the cardiac cycle showed that, although the WSS magnitude obviously changed over time, the distribution remained relatively unchanged*. This means that, at each point on the branch, the WSS magnitude over time resembled the shape of a typical flow rate waveform, which motivated our choice to describe its temporal variation with the pulsatility index. Figure 5.7 shows the distribution of WSSPI. Similar patterns could be observed among cases and controls. Near the bifurcation, regions of relatively high WSSPI were located on the posterior and anterior side of the ACA and regions of relatively low WSSPI were located on the superior and inferior side (see

*View animations online at http://dx.doi.org/10.6084/m9.figshare.1153934

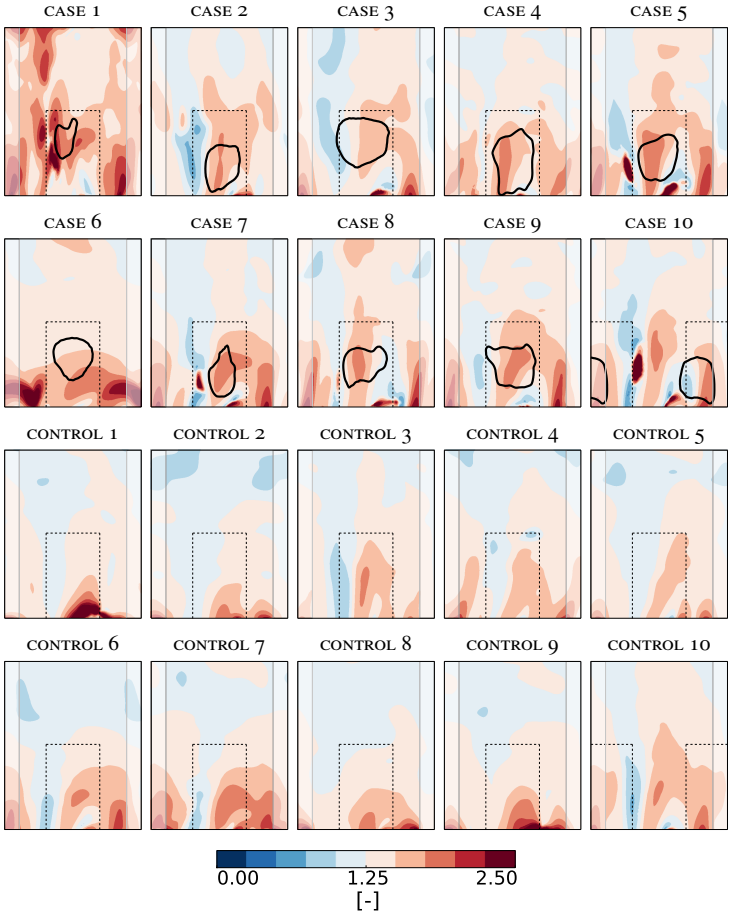

Figure 5.7: *WSS pulsatility index under 'normal' inflow conditions. The same colormap range was used for all cases and controls. Plot properties are explained in Figure 5.2C.*

Figure 5.2). Further downstream, WSSPI was also relatively low. As a result, we found significant differences between patches and non-patches. The main difference between cases and controls was that WSSPI was on average higher for cases, a significant difference for branches but not for patches. Judging from the contour plots, however, we did observe a clear correlation between WSSPI peaks and the aneurysm initiation site. Additional statistical analysis confirmed this observation by revealing that WSSPI was significantly higher for just the aneurysm than for the whole patch (1.61 vs. 1.52, $p = 0.007$), which was not true for any of the other variables. Among the assessed hemodynamic variables, WSSPI most consistently correlated with the aneurysm initiation site.

No pattern was found explaining the deviating aneurysm orientation of case 10. Removing the case and its matching control from analysis did not alter our findings.

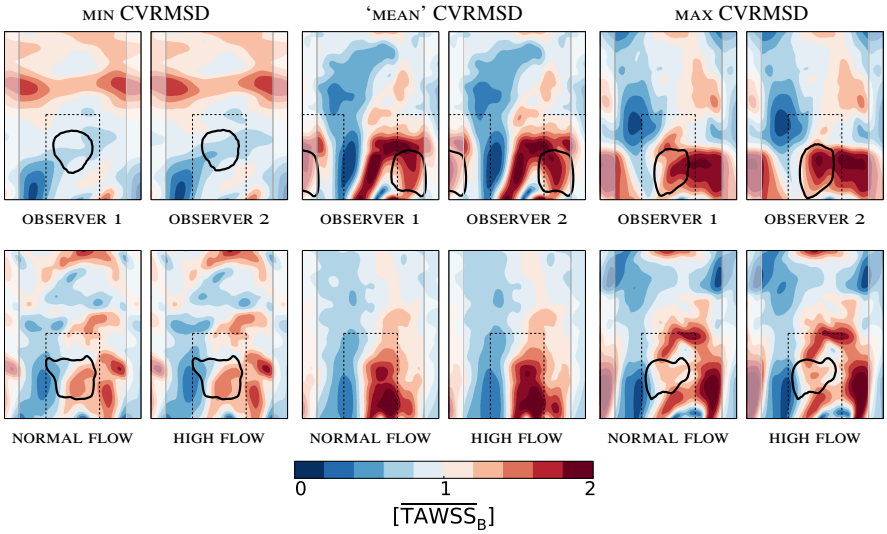

Figure 5.8: *Comparison of TAWSS distributions between observers removing the aneurysm and between 'normal' and 'high' flow rates at the inlet. Displayed are three cases or controls representating minimum, closest-to-mean and maximum CVRMSD. Colormaps were normalized by using* $\overline{\text{TAWSS}}_{\text{B}}$ *as unit. Plot properties are explained in Figure 5.2C.*

5.3.3 Sensitivity analysis

Figure 5.8 shows the differences in TAWSS distribution between the observers manually removing the aneurysm and between 'normal' and 'high' flow rates at the inlet. For each comparison, we chose three representative cases or controls, corresponding to minimum, closest-to-mean and maximum CVRMSD. Good agreement was found between observers and, although increasing the flow rate by 20 % increased the average TAWSS by 28 %, the TAWSS distribution remained relatively unchanged. CVRMSD between observers was 6.17 ± 0.07 % (mean±standard error), range: 3.57 to 8.05 %. CVRMSD between flow rates was 3.96 ± 0.04 %, range: 2.73 to 5.21 %. Reported findings were found to be insensitive to changes in both input parameters.

5.4 Discussion

5.4.1 Contributions

In summary, the main contributions of this study are: 1. the dataset was drawn from a multicenter database and was composed of cases with aneurysms at a single location, which was not in a known region of high WSS, and a matching set of controls, 2. objective comparison of variable distributions was made possible by automatic extraction and parametrization of the branch, 3. to our knowledge, this is the first study to evaluate the

transWSS and WSSPI in the context of aneurysm initiation, and 4. tests were performed to assess the sensitivity of the computed WSS field to the observer virtually removing the aneurysm and to the flow rate imposed at the inlet.

5.4.2 Aneurysm location

The majority of aneurysms are found at the apex of bifurcations or the outer wall of vascular bends, which has long established the importance of hemodynamic stresses in the initiation of cerebral aneurysms [63, 72, 105, 108, 173]. At the bifurcation apex, blood flow impinges the wall and rapidly accelerates and decelerates as it diverts into the branches. The associated WSS is low at the impingement region and high further downstream, with, along the branch, first high positive and then high negative gradients [53]. By complementing animal studies with CFD simulations, Meng and colleagues have gathered evidence indicating that the combination of high WSS and positive WSSG triggers the pathological remodeling leading to aneurysm formation [53, 134, 135]. Other CFD studies, using pre-aneurysm images, have corroborated this finding [109, 110, 113]. With respect to the rest of the branch and the controls, we also found aneurysms to form in regions of relatively high WSS and WSSG. However, although regions of positive WSSG were found close to the bifurcation apex, aneurysms were located further downstream in regions of mixed positive and negative WSSG.

Aneurysms also occur at locations with lesser-known hemodynamic conditions. Studying these locations can provide great insight into the hemodynamic mechanisms underlying aneurysm initiation. For instance, finding high WSS and WSSG in regions that are not commonly dominated by those WSS characteristics, which can be confirmed with controls, would provide stronger evidence in support of their role in aneurysm initiation. Recently, Lauric et al. reported on a study of 10 aneurysms located at the inner wall of the carotid siphon and 25 control ICAs [117]. The location was of particular interest as little was known about the hemodynamic conditions, except that the WSS was expected to be low. They found that aneurysms had formed in regions of low WSS flanked by peaks of high WSS and WSSG; WSS peaks correlated with the aneurysm necks; and controls were characterized by low, almost constant, WSS and WSSG. Similarly, in our study, comparing ACAs harboring aneurysms to ACAs that never formed an aneurysm allowed us to differentiate between hemodynamic stress patterns common to ACAs and those specific to aneurysm formation.

5.4.3 Temporal variation of WSS direction

Apart from their magnitudes, research has also focused on the oscillatory nature of the WSS and WSSG vectors. The most commonly used variable in this regard is the oscillatory shear index (OSI), which was introduced in the context of atherosclerosis [111] but later also used to study aneurysm initiation [109, 169, 171] and rupture [137, 209]. Two other variables were introduced specifically to study aneurysm initiation: the (potential)

aneurysm formation indicator (AFI) [127] and the gradient oscillatory number (GON) [169].

Variable definitions and contour plots for OSI, AFI and GON are included in the Appendix (Section 5.A). In accordance with previous studies, we found strong correlations between these variables, implying that they capture the same flow features [121, 146]: AFI correlated with OSI, GON correlated with absolute TAWSSG. The distribution of GON was very noisy, which can probably largely be attributed to it being the temporal variation of the second-order derivative of the velocity [46]. No clear correlations were found between the variable distributions and the aneurysm initiation site.

Peiffer et al. recently proposed the transWSS and showed that it captures different flow features than OSI [146]. Preliminary results indicated strong correlations with atherosclerotic lesion. Other than OSI and AFI, which give more weight to flow reversal, transWSS focuses solely on the multidirectional (vs. uniaxial) nature of disturbed flow. Given these unique properties, we considered it an interesting new variable to assess in the context of aneurysm initiation. However, although cases had on average significantly higher transWSS values, there were no clear correlations with the aneurysm initiation site.

5.4.4 Temporal variation of WSS magnitude

Among the assessed hemodynamic variables, WSSPI most consistently coincided with the aneurysm initiation site. The variable was introduced as a simple metric to quantify the temporal variation of the WSS magnitude without using noise-prone temporal gradients [121]. Besides the spatial variation of the WSS magnitude, related to the WSSG, and the temporal variation of the WSS direction, our results suggest that the temporal variation of the WSS magnitude is also an important factor to consider when investigating the role of hemodynamic stress in aneurysm initiation. This is in line with the observation that endothelial cells respond differently to temporal vs. spatial variations in WSS [202, 203] and to different types of pulsatile flow [77, 79].

5.4.5 Limitations and future directions

Aneurysms were virtually removed to approximate the pre-aneurysm vascular geometry. This approach has two main limitations. First, manual removal of aneurysms is observer-dependent. We addressed this by repeating the analysis with a second observer and found good agreement (Figure 5.8). Other studies employed automatic removal methods [46, 60, 169], but these preserve less of the vascular geometry and still rely on manually set parameters. Second, aneurysm removal does not account for possible changes in parent vessel geometry due to interaction with the perianeurysmal environment during aneurysm growth [168]. Since ICA bifurcations are not near bone structures, substantial changes were unlikely to have occurred. However, prospective studies are needed for confirmation.

Discrepancies between estimated and patient-specific flow rate waveforms at the inlet have been shown to strongly affect the WSS magnitude [92, 102, 129, 131], but not

the WSS distribution [129]. Therefore, we focused on the distribution by normalizing appropriate variables by the average WSS on the branch. We also repeated the analysis with a 20 % higher inflow rate to confirm that the WSS distribution remained relatively unchanged. The influence of the waveform shape on the WSSPI should be investigated. Regarding the outlets, despite the simplification of zero-pressure boundary conditions, the resulting ACA:MCA flow split of 34:66 closely matched the in vivo measurements (36:64) reported in [212]. Although much can be learned from WSS distributions, we wish to stress that CFD studies scrutinizing the role of hemodynamics in aneurysm initiation and rupture would greatly benefit from patient-specific boundary conditions. Ideally, a range of possible boundary conditions, covering all the patient's levels of exercise, should be considered to obtain a complete picture of the shear stresses exerted on the arterial wall.

Pathogenesis of cerebral aneurysms involves the interplay between mechanical stimuli, vascular biology, and vascular geometry [133]. Therefore, aneurysm initiation is likely caused by a combination of biochemical and biomechanical factors [162]. Although hemodynamic stresses appear to be important, their effect on the vascular biology, i.e. the mechanobiology, should also be modeled to gain a deeper understanding of the underlying mechanisms [85, 200, 201]. Moreover, among hemodynamic stresses, not only the WSS but also pressure-induced tensile stresses are known regulators of vascular biology and should be analyzed [133].

5.5 Conclusions

The aim of this study was to analyze the WSS field at the aneurysm initiation site. Ten cases with aneurysms at a single location were analyzed and compared with ten controls. We found that the general region in which aneurysms had formed was characterized by high TAWSS and high TAWSSG. The aneurysm initiation site partly overlapped with high TAWSS regions and, among all assessed variables, most consistently coincided with peaks of WSSPI.

5.6 Online data

To promote the future use of the dataset, surface meshes of all cases (with and without aneurysm) and controls have been made available on Figshare*.

*Access data online at http://dx.doi.org/10.6084/m9.figshare.1159108

5.A Appendix: Additional hemodynamic variables

This appendix presents the results for three additional hemodynamic variables that describe the oscillatory nature of the WSS and WSSG.

The oscillatory shear index (OSI) was introduced by Ku et al. [111] and later redefined by He and Ku [76]. It describes the oscillatory nature of the WSS vector, $\boldsymbol{\tau}_w$, during the cardiac cycle and has been used extensively in the context of atherosclerosis [147] and aneurysm initiation [109, 169, 171]. It is given by

$$\mathrm{OSI} = \frac{1}{2}\left(1 - \frac{\left|\int_0^T \boldsymbol{\tau}_w \,\mathrm{d}t\right|}{\int_0^T |\boldsymbol{\tau}_w| \,\mathrm{d}t}\right), \qquad \mathrm{OSI} \in [0, \tfrac{1}{2}] \tag{5.8}$$

t is time and T is the cardiac period.

The (potential) aneurysm formation indicator (AFI) was proposed by Mantha et al. [127] to identify flow stagnation zones, which in their study of three sidewall aneurysms coincided with the aneurysm initiation site. It measures the cosine of angle θ between the instantaneous WSS vector and the time-averaged WSS vector, that is,

$$\mathrm{AFI} = \cos\theta = \frac{\boldsymbol{\tau}_w}{|\boldsymbol{\tau}_w|} \cdot \hat{\boldsymbol{p}}, \qquad \mathrm{AFI} \in [-1, 1] \tag{5.9}$$

AFI was obtained at time point H1 of Ford et al.'s flow rate waveform [59], corresponding to midsystolic deceleration during which flow is least stable [68, p. 137].

The gradient oscillatory number (GON) was proposed by Shimogonya et al. [169] to quantify the degree of oscillating tension/compression forces at the aneurysm initiation site. It is given by

$$\mathrm{GON} = 1 - \frac{\left|\int_0^T \boldsymbol{G} \,\mathrm{d}t\right|}{\int_0^T |\boldsymbol{G}| \,\mathrm{d}t}, \qquad \mathrm{GON} \in [0, 1] \tag{5.10}$$

where

$$\boldsymbol{G} = \begin{pmatrix} \nabla_S (\boldsymbol{\tau}_w \cdot \hat{\boldsymbol{p}}) \cdot \hat{\boldsymbol{p}} \\ \nabla_S (\boldsymbol{\tau}_w \cdot \hat{\boldsymbol{q}}) \cdot \hat{\boldsymbol{q}} \end{pmatrix} \tag{5.11}$$

Contour plots of the three variables are in Figures 5.9 (OSI), 5.10 (AFI), and 5.11 (GON). We found strong correlations between OSI and AFI. GON patterns were very noisy and correlated strongly with low absolute TAWSSG. None of the variables correlated with the aneurysm location.

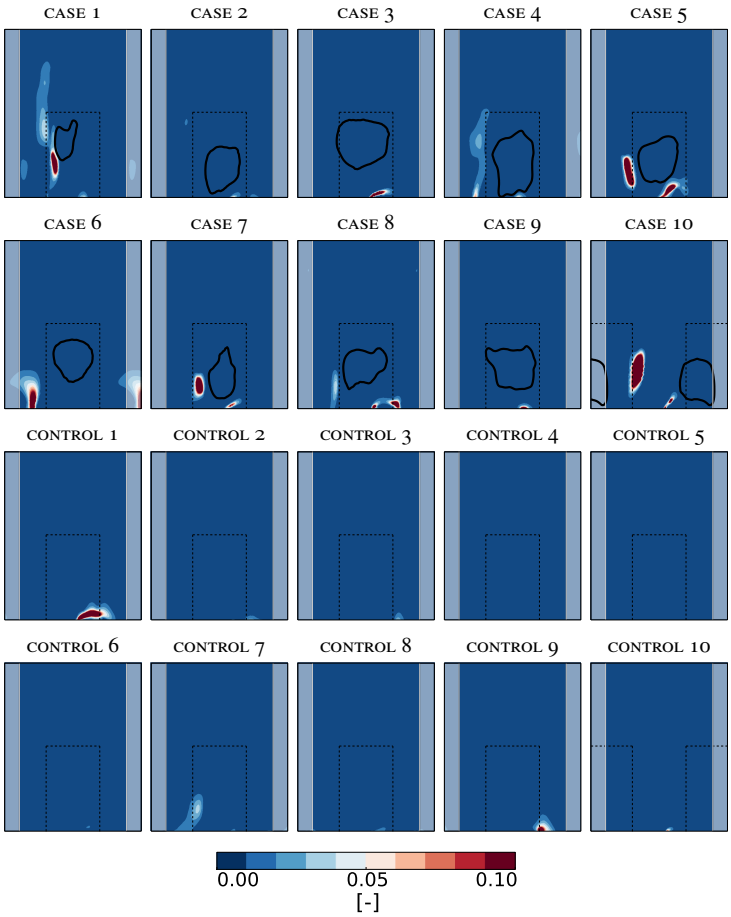

Figure 5.9: *Oscillatory shear index (OSI). Plot properties are explained in Figure 5.2C.*

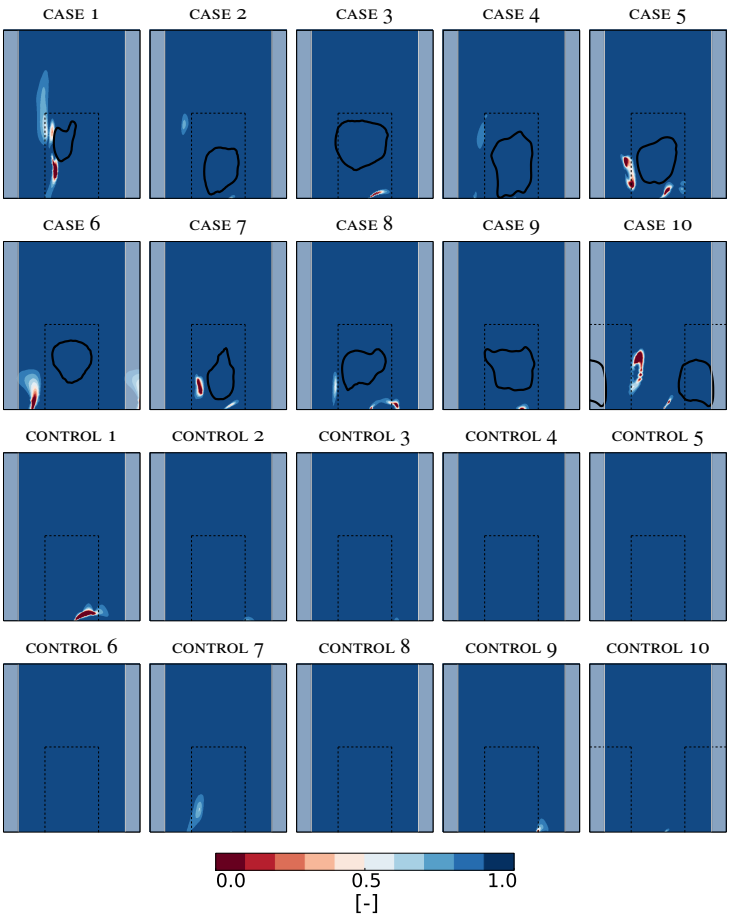

Figure 5.10: *Aneurysm formation indicator (AFI). Plot properties are explained in Figure 5.2C.*

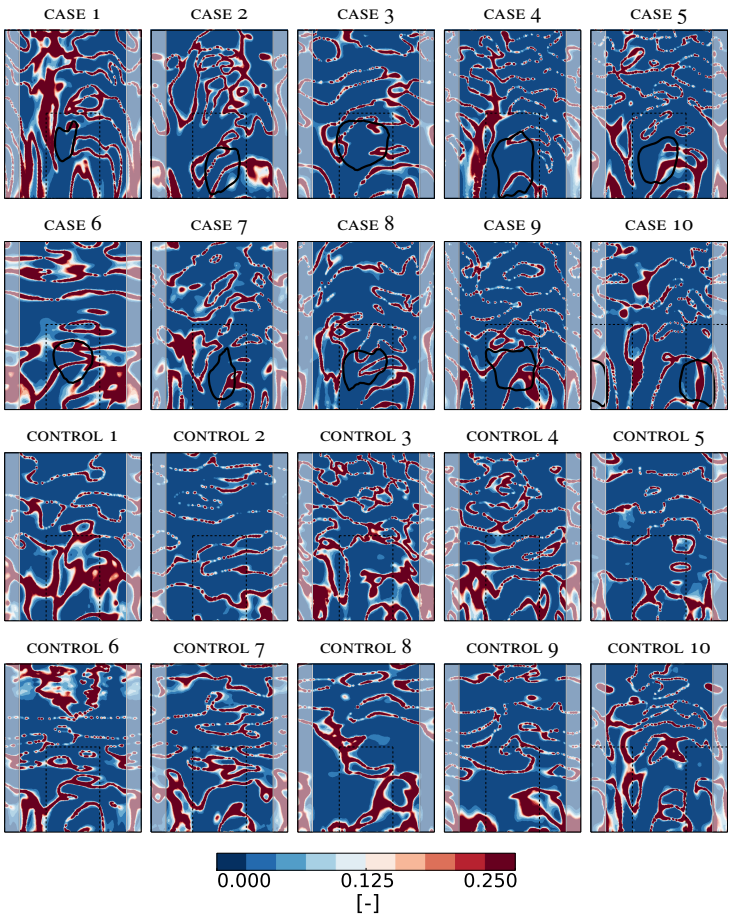

Figure 5.11: *Gradient oscillatory number (GON). Plot properties are explained in Figure 5.2C.*

References

[1] Achille PD and Humphrey JD. Toward large-scale computational fluid-solid-growth models of intracranial aneurysms. *The Yale Journal of Biology and Medicine*, 85(2):217–228, 2012. Cited on page 11.

[2] Alfano JM, Kolega J, Natarajan SK, Xiang J, Paluch RA, Levy EI, Siddiqui AH, and Meng H. Intracranial aneurysms occur more frequently at bifurcation sites that typically experience higher hemodynamic stresses. *Neurosurgery*, 73(3):497–505, 2013. Cited on pages 3, 58 and 59.

[3] Alnaes MS, Isaksen J, Mardal KA, Morgan BRMK, and Ingebrigtsen T. Computation of hemodynamics in the circle of Willis. *Stroke*, 38(9):2500–2505, 2007. Cited on pages 3, 58 and 59.

[4] Anderson JD. *Computational Fluid Dynamics: The Basics with Applications*. McGraw-Hill, Inc., 1995. Cited on page 5.

[5] Antiga L, Piccinelli M, Botti LA, Ene-Iordache B, Remuzzi A, and Steinman DA. An image-based modeling framework for patient-specific computational hemodynamics. *Medical and Biological Engineering and Computing*, 46(11):1097–1112, 2008. Cited on pages 30 and 61.

[6] Antiga L and Steinman DA. Robust and objective decomposition and mapping of bifurcating vessels. *IEEE Transactions on Medical Imaging*, 23(6):704–713, 2004. Cited on page 64.

[7] Anxionnat R, Bracard S, Ducrocq X, Trousset Y, Launay L, Kerrien E, Braun M, Vaillant R, Scomazzoni F, Lebedinsky A, and Picard L. Intracranial aneurysms: Clinical value of 3D digital subtraction angiography in the therapeutic decision and endovascular treatment. *Radiology*, 218(3):799–808, 2001. Cited on page 14.

[8] Appanaboyina S, Mut F, Löhner R, Putman CM, and Cebral JR. Simulation of intracranial aneurysm stenting: Techniques and challenges. *Computer Methods in Applied Mechanics and Engineering*, 198(45–46):3567–3582, 2009. Cited on page 36.

[9] Arrese I, Sarabia R, Pintado R, and Delgado-Rodriguez M. Flow-diverter devices for intracranial aneurysms: Systematic review and meta-analysis. *Neurosurgery*, 73(2):193–199, 2013. Cited on page 3.

[10] Attene M and Falcidieno B. ReMESH: An interactive environment to edit and repair triangle meshes. In *IEEE International Conference on Shape Modeling and Applications (SMI), Matsushima, Japan*, pages 271–276, 2006. Cited on page 15.

[11] Augsburger L, Farhat M, Philippe R, Fonck E, Kulcsar Z, Stergiopulos N, and Rüfenacht DA. Effect of flow diverter porosity on intraaneurysmal blood flow. *Klinische Neuroradiologie*, 19(3):204–214, 2009. Cited on page 52.

[12] Augsburger L, Reymond P, Rüfenacht DA, and Stergiopulos N. Intracranial stents being modeled as a porous medium: Flow simulation in stented cerebral aneurysms. *Annals of Biomedical Engineering*, 39(2):850–863, 2011. Cited on page 26.

[13] Babiker MH, Chong B, Gonzalez LF, Cheema S, and Frakes DH. Finite element modeling of embolic coil deployment: Multifactor characterization of treatment effects on cerebral aneurysm hemodynamics. *Journal of Biomechanics*, 46(16):2809–2816, 2013. Cited on page 26.

[14] Babiker MH, Gonzalez LF, Ryan J, Albuquerque F, Collins D, Elvikis A, and Frakes DH. Influence of stent configuration on cerebral aneurysm fluid dynamics. *Journal of Biomechanics*, 45(3):440–447, 2012. Cited on pages 26 and 36.

[15] Baek H, Jayaraman MV, and Karniadakis GE. Wall shear stress and pressure distribution on aneurysms and infundibulae in the posterior communicating artery bifurcation. *Annals of Biomedical Engineering*, 37(12):2469–2487, 2009. Cited on page 58.

[16] Baek H, Jayaraman MV, Richardson PD, and Karniadakis GE. Flow instability and wall shear stress variation in intracranial aneurysms. *Journal of the Royal Society Interface*, 7(47):967–988, 2010. Cited on page 53.

[17] Bernardini A, Larrabide I, Morales HG, Pennati G, L. Petrini SC, and Frangi AF. Influence of different computational approaches for stent deployment on cerebral aneurysm haemodynamics. *Interface Focus*, 1(3):338–348, 2011. Cited on page 29.

[18] Blanco PJ, Pivello MR, Urquiza SA, and Feijoo RA. On the potentialities of 3D-1D coupled models in hemodynamics simulations. *Journal of Biomechanics*, 42(7):919–930, 2009. Cited on page 11.

[19] Bogunović H, Pozo JM, Cárdenes R, San Román L, and Frangi AF. Anatomical labeling of the circle of Willis using maximum a posteriori probability estimation. *IEEE Transactions on Medical Imaging*, 32(9):1587–1599, 2013. Cited on page 53.

[20] Bogunović H, Pozo JM, Villa-Uriol MC, Majoie CB, van den Berg R, Gratama van Andel HAF, Macho JM, Blasco J, San Román L, and Frangi AF. Automated segmentation of cerebral vasculature with aneurysms in 3DRA and TOF-MRA using geodesic active regions: An evaluation study. *Medical Physics*, 38(1):210–222, 2011. Cited on pages 7, 40, 53 and 60.

[21] Bowker TJ, Watton PN, Summers PE, Byrne JV, and Ventikos Y. Rest versus exercise hemodynamics for middle cerebral artery aneurysms: A computational study. *American Journal of Neuroradiology*, 31(2):317–323, 2010. Cited on pages 21, 22 and 52.

[22] Brennan RL and Prediger DJ. Coefficient kappa: Some uses, misuses, and alternatives. *Educational and Psychological Measurement*, 41(3):687–699, 1981. Cited on page 18.

[23] Brewer CA. ColorBrewer 2.0. `http://www.colorbrewer2.org`. Accessed: 2013-03-04. Cited on page ii.

[24] Brinjikji W, Murad MH, Lanzino G, Cloft HJ, and Kallmes DF. Endovascular treatment of intracranial aneurysms with flow diverters: A meta-analysis. *Stroke*, 44(2):442–447, 2013. Cited on page 3.

[25] Brisman JL, Song JK, and Newell DW. Cerebral aneurysms. *New England Journal of Medicine*, 355(9):928–939, 2006. Cited on pages 2, 3 and 14.

[26] Butty VD, Gudjonsson K, Buchel P, Ventikos Y, Makhijani VB, and Poulikakos D. Residence times and basins of attraction for a realistic right internal carotid artery with two aneurysms. *Biorheology*, 39(3–4):1–8, 2002. Cited on page 6.

[27] Byrne JV, Beltechi R, Yarnold JA, Birks J, and Kamran M. Early experience in the treatment of intracranial aneurysms by endovascular flow diversion: A multicentre prospective study. *Plos One*, 5(9):1–8, 2010. Cited on page 3.

[28] Castro MA, Putman CM, and Cebral JR. Computational fluid dynamics modeling of intracranial aneurysms: Effects of parent artery segmentation on intra-aneurysmal hemodynamics. *American Journal of Neuroradiology*, 27(8):1703–1709, 2006. Cited on pages 22 and 52.

[29] Castro MA, Putman CM, and Cebral JR. Computational analysis of anterior communicating artery aneurysm shear stress before and after aneurysm formation. *Journal of Physics: Conference Series*, 332:012001, 2011. Cited on page 58.

[30] Castro MA, Putman CM, Radaelli AG, Frangi AF, and Cebral JR. Hemodynamics and rupture of terminal cerebral aneurysms. *Academic Radiology*, 16(10):1201–1207, 2009. Cited on pages 14, 17 and 40.

[31] Castro MA, Putman CM, Sheridan MJ, and Cebral JR. Hemodynamic patterns of anterior communicating artery aneurysms: A possible association with rupture. *American Journal of Neuroradiology*, 30(2):297–302, 2009. Cited on pages 14, 17, 22 and 23.

[32] Cavazzuti M, Atherton M, Collins M, and Barozzi G. Beyond the virtual intracranial stenting challenge 2007: Non-Newtonian and flow pulsatility effects. *Journal of Biomechanics*, 43(13):2645–2647, 2010. Cited on page 26.

[33] Cebral JR, Castro M, Putman CM, and Alperin N. Flow-area relationship in internal carotid and vertebral arteries. *Physiological Measurement*, 29(5):585–594, 2008. Cited on pages 41, 42, 55 and 61.

[34] Cebral JR, Castro MA, Appanaboyina S, Putman CM, Millan D, and Frangi AF. Efficient pipeline for image-based patient-specific analysis of cerebral aneurysm hemodynamics: Technique and sensitivity. *IEEE Transactions on Medical Imaging*, 24(4):457–467, 2005. Cited on pages 6, 14, 22 and 52.

[35] Cebral JR, Castro MA, Burgess JE, Pergolizzi RS, Sheridan MJ, and Putman CM. Characterization of cerebral aneurysms for assessing risk of rupture by using patient-specific computational hemodynamics models. *American Journal of Neuroradiology*, 26(10):2550–2559, 2005. Cited on pages 14 and 17.

[36] Cebral JR, Castro MA, Soto O, Lohner R, and Alperin N. Blood-flow models of the circle of Willis from magnetic resonance data. *Journal of Engineering Mathematics*, 47(3/4):369–386, 2003. Cited on page 42.

[37] Cebral JR, Hendrickson S, and Putman CM. Hemodynamics in a lethal basilar artery aneurysm just before its rupture. *American Journal of Neuroradiology*, 30(1):95–98, 2009. Cited on page 14.

[38] Cebral JR, Hernandez M, and Frangi AF. Computational analysis of blood flow dynamics in cerebral aneurysms from CTA and 3D rotational angiography image data. In *International Congress on Computational Bioengineering, Zaragoza, Spain*, 2003. Cited on page 6.

[39] Cebral JR and Lohner R. Efficient simulation of blood flow past complex endovascular devices using an adaptive embedding technique. *IEEE Transactions on Medical Imaging*, 24(4):468–476, 2005. Cited on page 14.

[40] Cebral JR, Mut F, Raschi M, Scrivano E, Ceratto R, Lylyk P, and Putman CM. Aneurysm rupture following treatment with flow-diverting stents: Computational hemodynamics analysis of treatment. *American Journal of Neuroradiology*, 32(1):27–33, 2011. Cited on pages 26 and 40.

[41] Cebral JR, Mut F, Weir J, and Putman CM. Association of hemodynamic characteristics and cerebral aneurysm rupture. *American Journal of Neuroradiology*, 32(2):264–270, 2011. Cited on pages 40 and 53.

[42] Cebral JR, Mut F, Weir J, and Putman CM. Quantitative characterization of the hemodynamic environment in ruptured and unruptured brain aneurysms. *American Journal of Neuroradiology*, 32(1):145–151, 2011. Cited on pages 40 and 52.

[43] Cekirge HS, Yavuz K, Geyik S, and Saatci I. A novel "Y" stent flow diversion technique for the endovascular treatment of bifurcation aneurysms without endosaccular coiling. *American Journal of Neuroradiology*, 32(7):1262–1268, 2011. Cited on page 36.

[44] Cha KS, Balaras E, Lieber BB, Sadasivan C, and Wakhloo AK. Modeling the interaction of coils with the local blood flow after coil embolization of intracranial aneurysms. *Journal of Biomechanical Engineering*, 129(6):873–879, 2007. Cited on page 14.

[45] Chatziprodromou I, Butty VD, Makhijani VB, Poulikakos D, and Ventikos Y. Pulsatile blood flow in anatomically accurate vessels with multiple aneurysms: A medical intervention planning application of computational haemodynamics. *Flow, Turbulence and Combustion*, 71:333–346, 2003. Cited on page 6.

[46] Chen H, Selimovic A, Thompson H, Chiarini A, Penrose J, Ventikos Y, and Watton PN. Investigating the influence of haemodynamic stimuli on intracranial aneurysm inception. *Annals of Biomedical Engineering*, 41(7):1492–1504, 2013. Cited on pages 58 and 73.

[47] Chen P, Quarteroni A, and Rozza G. Simulation-based uncertainty quantification of human arterial network hemodynamics. *International Journal for Numerical Methods in Biomedical Engineering*, 29(6):698–721, 2013. Cited on page 11.

[48] Chien S. Mechanotransduction and endothelial cell homeostasis: the wisdom of the cell. *American Journal of Physiology: Heart and Circulatory Physiology*, 292(3):H1209–H1224, 2007. Cited on page 3.

[49] Cloft HJ, Joseph GJ, and Dion JE. Risk of cerebral angiography in patients with subarachnoid hemorrhage, cerebral aneurysm, and arteriovenous malformation: A meta-analysis. *Stroke*, 30(2):317–320, 1999. Cited on page 14.

[50] Dempere-Marco L, Oubel E, Castro MA, Putman CM, Frangi AF, and Cebral JR. CFD analysis incorporating the influence of wall motion: Application to intracranial aneurysms. In *Proceedings of the 9th International Conference on Medical Image Computing and Computer-Assisted Intervention (MICCAI), Copenhagen, Denmark*, pages 438–445, 2006. Cited on pages 7 and 22.

[51] Dhar S, Tremmel M, Mocco J, Kim M, Yamamoto J, Siddiqui AH, Hopkins L, and Meng H. Morphology parameters for intracranial aneurysm rupture risk assessment. *Neurosurgery*, 63(2):185–197, 2008. Cited on page 43.

[52] Doenitz C, Schebesch KM, Zoephel R, and Brawanski A. A mechanism for the rapid development of intracranial aneurysms: a case study. *Neurosurgery*, 67(5):1213–1221, 2010. Cited on page 58.

[53] Dolan JM, Kolega J, and Meng H. High wall shear stress and spatial gradients in vascular pathology: A review. *Annals of Biomedical Engineering*, 41(7):1411–1427, 2013. Cited on pages 4, 11, 40, 58, 62 and 72.

[54] Etminan N, Beseoglu K, Barrow DL, Bederson J, Brown RD, Connolly ES, Derdeyn CP, Hänggi D, Hasan D, Juvela S, Kasuya H, Kirkpatrick PJ, Knuckey N, Koivisto T, Lanzino G, Lawton MT, LeRoux P, McDougall CG, Mee E, Mocco J, Molyneux A, Morgan MK, Mori K, Morita A, Murayama Y, Nagahiro S, Pasqualin A, Raabe A, Raymond J, Rinkel GJE, Rüfenacht D, Seifert V, Spears J, Steiger HJ, Steinmetz H, Torner JC, Vajkoczy P, Wanke I, Wong GKC, Wong JH, and Macdonald RL. Multidisciplinary consensus on assessment of unruptured intracranial aneurysms: Proposal of an international research group. *Stroke*, 45(5):1523–1530, 2014. Cited on page 3.

[55] Feigin VL, Lawes CMM, a. Bennett D, and Anderson CS. Stroke epidemiology: A review of population-based studies of incidence, prevalence, and case-fatality in the late 20th century. *The Lancet: Neurology*, 2(1):43–53, 2003. Cited on page 2.

[56] Feigin VL, Rinkel GJE, Lawes CM, Algra A, Bennett DA, van Gijn J, and Anderson CS. Risk factors for subarachnoid hemorrhage: An updated systematic review of epidemiological studies. *Stroke*, 36(12):2773–2780, 2005. Cited on page 3.

[57] Fenner JW, Brook B, Clapworthy G, Coveney PV, Feipel V, Gregersen H, Hose DR, Kohl P, Lawford P, McCormack KM, Pinney D, Thomas SR, Jan SVS, Waters S, and Viceconti M. The EuroPhysiome, STEP and a roadmap for the virtual physiological human. *Philosophical Transactions of the Royal Society a-Mathematical Physical and Engineering Sciences*, 366(1878):2979–2999, 2008. Cited on page 5.

[58] Ferns SP, Schneiders JJ, Siebes M, van den Berg R, VanBavel ET, and Majoie CB. Intracranial blood-flow velocity and pressure measurements using an intra-arterial dual-sensor guidewire. *AJNR. American journal of neuroradiology*, 31(2):324–6, 2010. Cited on page 4.

[59] Ford MD, Alperin N, Lee SH, Holdsworth DW, and Steinman DA. Characterization of volumetric flow rate waveforms in the normal internal carotid and vertebral arteries. *Physiological Measurement*, 26(4):477–488, 2005. Cited on pages 41, 42, 61 and 75.

[60] Ford MD, Hoi Y, Piccinelli M, Antiga L, and Steinman DA. An objective approach to digital removal of saccular aneurysms: Technique and applications. *The British Journal of Radiology*, 82(SI-1):S55–S61, 2009. Cited on pages 58 and 73.

[61] Ford MD, Nikolov HN, Milner JS, Lownie SP, Demont EM, Kalata W, Loth F, Holdsworth DW, and Steinman DA. PIV-measured versus CFD-predicted flow dynamics in anatomically realistic cerebral aneurysm models. *Journal of Biomechanical Engineering*, 130(2):21015, 2008. Cited on page 33.

[62] Ford MD and Piomelli U. Exploring high frequency temporal fluctuations in the terminal aneurysm of the basilar bifurcation. *Journal of Biomechanical Engineering*, 134(9):091003, 2012. Cited on page 53.

[63] Foutrakis GN, Yonas H, and Sclabassi RJ. Saccular aneurysm formation in curved and bifurcating arteries. *American Journal of Neuroradiology*, 20(7):1309–1317, 1999. Cited on pages 6 and 72.

[64] Frösen J. Smooth muscle cells and the formation, degeneration, and rupture of saccular intracranial aneurysm wall: A review of current pathophysiological knowledge. *Translational Stroke Research*, 5(3):347–356, 2014. Cited on page 58.

[65] Frösen J, Piippo A, Paetau A, Kangasniemi M, Niemela M, Hernesniemi J, and Jaaskelainen J. Remodeling of saccular cerebral artery aneurysm wall is associated with rupture: Histological analysis of 24 unruptured and 42 ruptured cases. *Stroke*, 35(10):2287–2293, 2004. Cited on page 14.

[66] Fu W, Gu Z, Meng X, Chu B, and Qiao AK. Numerical simulation of hemodynamics in stented internal carotid aneurysm based on patient-specific model. *Journal of Biomechanics*, 43(7):1337–1342, 2010. Cited on pages 26 and 36.

[67] Fukazawa K, Ishida F, Umeda Y, Miura Y, Shimosaka S, Matsushima S, Taki W, and Suzuki H. Using computational fluid dynamics analysis to characterize local hemodynamic features of middle cerebral artery aneurysm rupture points. *World Neurosurgery*, 2013. [Epub ahead of print]. Cited on page 40.

[68] Fung YC. *Biomechanics: Circulation*. Springer, 2nd edition, 1997. Cited on page 75.

[69] Gambaruto AM, Janela J, Moura A, and Sequeira A. Sensitivity of hemodynamics in a patient specific cerebral aneurysm to vascular geometry and blood rheology. *Mathematical Bioscience and Engineering*, 8(2):409–423, 2011. Cited on page 52.

[70] Geers AJ, Larrabide I, Morales HG, and Frangi AF. Approximating hemodynamics of cerebral aneurysms with steady flow simulations. *Journal of Biomechanics*, 47(1):178–185, 2014. Cited on pages 61 and 62.

[71] Geers AJ, Larrabide I, Radaelli AG, Bogunović H, Kim M, Gratama van Andel HAF, Majoie CB, VanBavel E, and Frangi AF. Patient-specific computational hemodynamics of intracranial aneurysms from 3D rotational angiography and CT angiography: An in vivo reproducibility study. *American Journal of Neuroradiology*, 32(3):581–586, 2011. Cited on pages 37, 52 and 63.

[72] Gonzalez CF, Cho YI, Ortega HV, and Moret J. Intracranial aneurysms: Flow analysis of their origin and progression. *American Journal of Neuroradiology*, 13(1):181–188, 1992. Cited on pages 6, 14 and 72.

[73] Gosling RG and King DH. Arterial assessment by Doppler-shift ultrasound. *Proceedings of the Royal Society of Medicine*, 67(6 Pt 1):447–449, 1974. Cited on page 63.

[74] Grinberg L and Karniadakis GE. Outflow boundary conditions for arterial networks with multiple outlets. *Annals of Biomedical Engineering*, 36(9):1496–1514, 2008. Cited on page 36.

[75] Hashimoto T, Meng H, and Young WL. Intracranial aneurysms: Links among inflammation, hemodynamics and vascular remodeling. *Neurological Research*, 28(4):372–380, 2006. Cited on pages 4, 14, 16 and 40.

[76] He X and Ku DN. Pulsatile flow in the human left coronary artery bifurcation: Average conditions. *Journal of Biomechanical Engineering*, 118(1):74–82, 1996. Cited on page 75.

[77] Helmlinger G, Geiger RV, Schreck S, and Nerem RM. Effects of pulsatile flow on cultured vascular endothelial cell morphology. *Journal of Biomechanical Engineering*, 113(2):123–131, 1991. Cited on page 73.

[78] Hernandez M and Frangi AF. Non-parametric geodesic active regions: Method and evaluation for cerebral aneurysms segmentation in 3DRA and CTA. *Medical Image Analysis*, 11(3):224–241, 2007. Cited on pages 7, 14, 15 and 23.

[79] Himburg HA, Dowd SE, and Friedman MH. Frequency-dependent response of the vascular endothelium to pulsatile shear stress. *American Journal of Physiology: Heart and Circulatory Physiology*, 293(1):H645–H653, 2007. Cited on page 73.

[80] Hoi Y, Wasserman BA, Lakatta EG, and Steinman DA. Carotid bifurcation hemodynamics in older adults: Effect of measured versus assumed flow waveform. *Journal of Biomechanical Engineering*, 132(7):71006, 2010. Cited on page 22.

[81] Hoi Y, Wasserman BA, Xie YJ, Najjar SS, Ferruci L, Lakatta EG, Gerstenblith G, and Steinman DA. Characterization of volumetric flow rate waveforms at the carotid bifurcations of older adults. *Physiological Measurement*, 31(3):291–302, 2010. Cited on pages 22, 41 and 42.

[82] Hoi Y, Woodward SH, Kim M, Taulbee DB, and Meng H. Validation of CFD simulations of cerebral aneurysms with implication of geometric variations. *Journal of Biomechanical Engineering*, 128(6):844–851, 2006. Cited on pages 33 and 34.

[83] Hop JW, Rinkel GJ, Algra A, and van Gijn J. Case-fatality rates and functional outcome after subarachnoid hemorrhage: a systematic review. *Stroke*, 28(3):660–664, 1997. Cited on pages 2 and 58.

[84] Humphrey JD. Coupling haemodynamics with vascular wall mechanics and mechanobiology to understand intracranial aneurysms. *International Journal of Computational Fluid Dynamics*, 23(8):569–581, 2009. Cited on page 11.

[85] Humphrey JD and Taylor CA. Intracranial and abdominal aortic aneurysms: Similarities, differences, and need for a new class of computational models. *Annual Review of Biomedical Engineering*, 10:221–246, 2008. Cited on pages 3 and 74.

[86] Hunter JD. Matplotlib: A 2D graphics environment. *Computing In Science & Engineering*, 9(3):90–95, 2007. Cited on pages ii and 30.

[87] Hunter PJ and Borg TK. Integration from proteins to organs: the Physiome Project. *Nature Reviews Molecular Cell Biology*, 4(3):237–243, 2003. Cited on page 5.

[88] Ingebrigtsen T, Morgan MK, Faulder K, Ingebrigtsen L, Sparr T, and Schirmer H. Bifurcation geometry and the presence of cerebral artery aneurysms. *Journal of Neurosurgery*, 101(1):108–113, 2004. Cited on page 63.

[89] Izar B, Rai A, Raghuram K, Rotruck J, and Carpenter J. Comparison of devices used for stent-assisted coiling of intracranial aneurysms. *Plos One*, 6(9):e24875, 2011. Cited on page 36.

[90] Jamous MA, Nagahiro S, Kitazato KT, Satoh K, and Satomi J. Vascular corrosion casts mirroring early morphological changes that lead to the formation of saccular cerebral aneurysm: An experimental study in rats. *Journal of Neurosurgery*, 102(3):532–535, 2005. Cited on page 58.

[91] Janiga G, Rössl C, Skalej M, and Thévenin D. Realistic virtual intracranial stenting and computational fluid dynamics for treatment analysis. *Journal of Biomechanics*, 46(1):7–12, 2013. Cited on pages 36 and 52.

[92] Jansen IGH, Schneiders JJ, Potters WV, van Ooij P, van den Berg R, VanBavel E, Marquering HA, and Majoie CBLM. Generalized versus patient-specific inflow boundary conditions in computational fluid dynamics simulations of cerebral aneurysmal hemodynamics. *American journal of Neuroradiology*, 35(8):1543–1548, 2014. Cited on pages 10, 63 and 73.

[93] Jiang JF and Strother CM. Computational fluid dynamics simulations of intracranial aneurysms at varying heart rates: A "patient-specific" study. *Journal of Biomechanical Engineering*, 131(9):91001, 2009. Cited on page 22.

[94] Johnston SC, Selvin S, and Gress DR. The burden, trends, and demographics of mortality from subarachnoid hemorrhage. *Neurology*, 50(5):1413–1418, 1998. Cited on page 2.

[95] Jou LD, Lee DH, Morsi H, and Mawad ME. Wall shear stress on ruptured and unruptured intracranial aneurysms at the internal carotid artery. *American Journal of Neuroradiology*, 29(9):1761–1767, 2008. Cited on pages 14, 17, 23 and 40.

[96] Jou LD, Mohamed A, Lee DH, and Mawad ME. 3D rotational digital subtraction angiography may underestimate intracranial aneurysms: Findings from two basilar aneurysms. *American Journal of Neuroradiology*, 28(9):1690–1692, 2007. Cited on page 21.

[97] Jou LD, Quick CM, Young WL, Lawton MT, Higashida RT, Martin AJ, and Saloner D. Computational approach to quantifying hemodynamic forces in giant cerebral aneurysms. *American Journal of Neuroradiology*, 24(9):1804–1810, 2003. Cited on page 6.

[98] Juvela S, Porras M, and Poussa K. Natural history of unruptured intracranial aneurysms: Probability of and risk factors for aneurysm rupture. *Journal of Neurosurgery*, 93(3):379–387, 2000. Cited on page 3.

[99] Juvela S, Poussa K, and Porras M. Factors Affecting Formation and Growth of Intracranial Aneurysms : A Long-Term Follow-Up Study. *Stroke*, 32(2):485–491, 2001. Cited on page 3.

[100] Kadasi LM, Dent WC, and Malek AM. Colocalization of thin-walled dome regions with low hemodynamic wall shear stress in unruptured cerebral aneurysms. *Journal of Neurosurgery*, 119(1):172–179, 2013. Cited on page 52.

[101] Kakalis NM, Mitsos AP, Byrne JV, and Ventikos YP. The haemodynamics of endovascular aneurysm treatment: A computational modelling approach for estimating the influence of multiple coil deployment. *IEEE Transactions on Medical Imaging*, 27(6):814–824, 2008. Cited on pages 14, 26 and 40.

[102] Karmonik C, Yen C, Diaz O, Klucznik R, Grossman RG, and Benndorf G. Temporal variations of wall shear stress parameters in intracranial aneurysms-importance of patient-specific inflow waveforms for CFD calculations. *Acta Neurochirurgica*, 152(8):1391–1398, 2010. Cited on pages 10, 37, 52, 63 and 73.

[103] Karmonik C, Yen C, Gabrie E, Partovi S, Horner M, Zhang YJ, Klucznik RP, Diaz O, and Grossman RG. Quantification of speed-up and accuracy of multi-CPU computational flow dynamics simulations of hemodynamics in a posterior communicating artery aneurysm of complex geometry. *Journal of Neurointerventional Surgery*, 5(Suppl 3):iii48–iii55, 2013. Cited on page 53.

[104] Kawaguti M. Numerical Solution of the NS Equations for the Flow Around a Circular Cylinder at Reynolds Number 40. *Journal of the Physical Society of Japan*, 8:747–757, 1953. Cited on page 6.

[105] Kayembe KN, Sasahara M, and Hazama F. Cerebral aneurysms and variations in the Circle of Willis. *Stroke*, 15(5):846–850, 1984. Cited on pages 3, 14 and 72.

[106] Kim M, Levy EI, Meng H, and Hopkins LN. Quantification of hemodynamic changes induced by virtual placement of multiple stents across a wide-necked basilar trunk aneurysm. *Neurosurgery*, 61(6):1305–1312, 2007. Cited on pages 14, 26 and 36.

[107] Kim M, Taulbee DB, Tremmel M, and Meng H. Comparison of two stents in modifying cerebral aneurysm hemodynamics. *Annals of Biomedical Engineering*, 36(5):726–741, 2008. Cited on page 52.

[108] Kondo S, Hashimoto N, Kikuchi H, Hazama F, Nagata I, and Kataoka H. Cerebral aneurysms arising at nonbranching sites: An experimental Study. *Stroke*, 28(2):398–403, 1997. Cited on pages 3, 58, 59 and 72.

[109] Kono K, Fujimoto T, and Terada T. Proximal stenosis may induce initiation of cerebral aneurysms by increasing wall shear stress and wall shear stress gradient. *International Journal for Numerical Methods in Biomedical Engineering*, 2014. [Epub ahead of print]. Cited on pages 58, 72 and 75.

[110] Kono K and Terada T. Hemodynamics of 8 different configurations of stenting for bifurcation aneurysms. *American Journal of Neuroradiology*, 34(10):1980–1986, 2013. Cited on pages 26, 36, 58 and 72.

[111] Ku DN, Giddens DP, Zarins CK, and Glagov S. Pulsatile flow and atherosclerosis in the human carotid bifurcation: Positive correlation between plaque location and low oscillating shear stress. *Arteriosclerosis*, 5(3):293–302, 1985. Cited on pages 17, 72 and 75.

[112] Kulcsar Z, Augsburger L, Reymond P, Pereira VM, Mallik SHAS, Millar J, Wetzel SG, Wanke I, and Rüfenacht DA. Flow diversion treatment: Intra-aneurismal blood flow velocity and WSS reduction are parameters to predict aneurysm thrombosis. *Acta Neurochirurgica*, 154(10):1827–1834, 2012. Cited on page 3.

[113] Kulcsar Z, Ugron A, Marosfoi M, Berentei Z, Paál G, and Szikora I. Hemodynamics of cerebral aneurysm initiation: The role of wall shear stress and spatial wall shear stress gradient. *American Journal of Neuroradiology*, 32(3):587–594, 2011. Cited on pages 58 and 72.

[114] Larrabide I, Aguilar ML, Morales HG, Geers AJ, Kulcsár Z, Rufenacht D, and Frangi AF. Intra-aneurysmal pressure and flow changes induced by flow diverters: Relation to aneurysm size and shape. *American Journal of Neuroradiology*, 34(4):816–822, 2013. Cited on pages 26 and 40.

[115] Larrabide I, Kim M, Augsburger L, Villa-Uriol MC, Rüfenacht DA, and Frangi AF. Fast virtual deployment of self-expandable stents: Method and in vitro evaluation for intracranial aneurysmal stenting. *Medical Image Analysis*, 16(3):721–730, 2012. Cited on pages 14 and 29.

[116] Larrabide I, Villa-Uriol MC, Cárdenes R, Pozo JM, Macho J, Roman LS, Blasco J, Vivas E, Marzo A, Hose DR, and Frangi AF. Three-dimensional morphological analysis of intracranial aneurysms: A fully automated method for aneurysm sac isolation and quantification. *Medical Physics*, 38(5):2439–2449, 2011. Cited on pages 41 and 53.

[117] Lauric A, Hippelheuser J, Safain MG, and Malek AM. Curvature effect on hemodynamic Conditions at the inner bend of the carotid siphon and its relation to aneurysm formation. *Journal of Biomechanics*, 2014. [Epub ahead of print]. Cited on pages 58 and 72.

[118] Lauric A, Miller E, Frisken S, and Malek AM. Automated detection of intracranial aneurysms based on parent vessel 3D analysis. *Medical Image Analysis*, 14(2):149–159, 2010. Cited on page 53.

[119] Lawson MF, Newman WC, Chi Y, Mocco JD, and Hoh BL. Stent-associated flow remodeling causes further occlusion of incompletely coiled aneurysms. *Neurosurgery*, 69(3):598–603, 2011. Cited on page 36.

[120] Lee RM. Morphology of cerebral arteries. *Pharmacology & Therapeutics*, 66(1):149–173, 1995. Cited on page 3.

[121] Lee SW, Antiga L, and Steinman DA. Correlations among indicators of disturbed flow at the normal carotid bifurcation. *Journal of Biomechanical Engineering*, 131(6):061013, 2009. Cited on page 73.

[122] Lell MM, Anders K, Uder M, Klotz E, Ditt H, Vega-Higuera F, Boskamp T, Bautz WA, and Tomandl BF. New techniques in CT angiography. *Radiographics*, 26:S45–S62, 2006. Cited on page 24.

[123] Liou TM and Li YC. Effects of stent porosity on hemodynamics in a sidewall aneurysm model. *Journal of Biomechanics*, 41:1174–1183, 2008. Cited on page 14.

[124] Lylyk P, Miranda C, Ceratto R, Ferrario A, Scrivano E, Luna HR, Berez AL, Tran Q, Nelson PK, and Fiorella D. Curative endovascular reconstruction of cerebral aneurysms with the pipeline embolization device: The Buenos Aires experience. *Neurosurgery*, 64(4):632–642, 2009. Cited on page 3.

[125] Malek AM, Alper SL, and Izumo S. Hemodynamic shear stress and its role in atherosclerosis. *Journal of the American Medical Association*, 282(21):2035–2042, 1999. Cited on pages 4 and 40.

[126] Mantha AR, Benndorf G, Hernandez A, and Metcalfe RW. Stability of pulsatile blood flow at the ostium of cerebral aneurysms. *Journal of Biomechanics*, 42(8):1081–1087, 2009. Cited on page 40.

[127] Mantha AR, Karmonik C, Benndorf G, Strother C, and Metcalfe RW. Hemodynamics in a cerebral artery before and after the formation of an aneurysm. *American Journal of Neuroradiology*, 27(5):1113–1118, 2006. Cited on pages 53, 58, 73 and 75.

[128] Markl M, Frydrychowicz A, Kozerke S, Hope M, and Wieben O. 4D flow MRI. *Journal of Magnetic Resonance Imaging*, 36(5):1015–1036, 2012. Cited on pages 4 and 58.

[129] Marzo A, Singh PK, Larrabide I, Radaelli AG, Coley SC, Gwilliam M, Wilkinson I, Lawford PV, Reymond P, Patel U, Frangi AF, and Hose DR. Computational hemodynamics in cerebral aneurysms: The effects of modeled versus measured boundary conditions. *Annals of Biomedical Engineering*, 39(2):884–896, 2011. Cited on pages 10, 52, 63, 73 and 74.

[130] Mazumdar JN. *Biofluid Mechanics*. World Scientific, 1992. Cited on page 5.

[131] McGah P, Levitt MR, Barbour MC, Morton RP, Nerva JD, Mourad PD, Ghodke BV, Hallam DK, Sekhar LN, Kim LJ, and Aliseda A. Accuracy of computational cerebral aneurysm hemodynamics using patient-specific endovascular measurements. *Annals of Biomedical Engineering*, 42(3):503–514, 2014. Cited on pages 4, 10, 37, 63 and 73.

[132] McKinney AM, Palmer CS, Truwit CL, Karagulle A, and Teksam M. Detection of aneurysms by 64-section multidetector CT angiography in patients acutely suspected of having an intracranial aneurysm and comparison with digital subtraction and 3D rotational angiography. *American Journal of Neuroradiology*, 29(3):594–602, 2008. Cited on page 24.

[133] Meng H, Tutino VM, Xiang JP, and Siddiqui A. High WSS or low WSS? Complex interactions of hemodynamics with intracranial aneurysm initiation, growth, and rupture: Toward a unifying hypothesis. *American Journal of Neuroradiology*, 35(7):1254–1262, 2014. Cited on pages 4, 58 and 74.

[134] Meng H, Wang Z, Gao BL, Hoi Y, Metaxa EM, Swartz DD, and Kolega J. Complex hemodynamics at the apex of an arterial bifurcation induces vascular remodeling resembling cerebral aneurysm initiation. *Stroke*, 38(6):1924–1931, 2007. Cited on pages 11, 58 and 72.

[135] Metaxa EM, Tremmel M, Natarajan SK, Xiang JP, Paluch RA, Mandelbaum M, Siddiqui AH, Kolega J, Mocco J, and Meng H. Characterization of critical hemodynamics contributing to aneurysmal remodeling at the basilar terminus in a rabbit model. *Stroke*, 41(8):1774–1782, 2010. Cited on pages 11, 58 and 72.

[136] Metcalfe RW. The promise of computational fluid dynamics as a tool for delineating therapeutic options in the treatment of aneurysms. *American Journal of Neuroradiology*, 24(4):553–554, 2003. Cited on page 26.

[137] Miura Y, Ishida F, Umeda Y, Tanemura H, Suzuki H, Matsushima S, Shimosaka S, and Taki W. Low wall shear stress is independently associated with the rupture status of middle cerebral artery aneurysms. *Stroke*, 44(2):519–521, 2013. Cited on pages 40, 52 and 72.

[138] Molyneux AJ, Kerr RS, Yu LM, Clarke M, Sneade M, Yarnold JA, and Sandercock P. International Subarachnoid Aneurysm Trial (ISAT) of neurosurgical clipping versus endovascular coiling in 2143 patients with ruptured intracranial aneurysms: A randomised comparison of effects on survival, dependency, seizures, rebleeding, subgr. *Lancet*, 366(9488):809–817, 2005. Cited on page 3.

[139] Morales HG, Larrabide I, Geers AJ, Aguilar ML, and Frangi AF. Newtonian and non-Newtonian blood flow in coiled cerebral aneurysms. *Journal of Biomechanics*, 46(13):2158–2164, 2013. Cited on page 61.

[140] Morales HG, Larrabide I, Geers AJ, Roman LS, Blasco J, Macho JM, and Frangi AF. A virtual coiling technique for image-based aneurysm models by dynamic path planning. *IEEE Transactions on Medical Imaging*, 32(1):119–129, 2013. Cited on pages 7, 26 and 40.

[141] Müller JD, Jitsumura M, and Müller-Kronast NHF. Sensitivity of flow simulations in a cerebral aneurysm. *Journal of Biomechanics*, 45(15):2539–2548, 2012. Cited on pages 40 and 53.

[142] Nealen A, Igarashi T, Sorkine O, and Alexa M. Laplacian mesh optimization. In *Proceedings of the 4th International Conference on Computer Graphics and Interactive Techniques in Australasia and Southeast Asia (GRAPHITE), Kuala Lumpur, Malaysia*, pages 381–389, 2006. Cited on pages 29, 40 and 60.

[143] Nixon AM, Gunel M, and Sumpio BE. The critical role of hemodynamics in the development of cerebral vascular disease. *Journal of Neurosurgery*, 112(6):1240–1253, 2010. Cited on pages 3 and 58.

[144] Palero V, Lobera J, and Arroyo M. Three-component velocity field measurement in confined liquid flows with high-speed digital image plane holography. *Experiments in Fluids*, 49(2):471–483, 2010. Cited on pages 26, 27 and 34.

[145] Passerini T, de Luca M, Formaggia L, Quarteroni A, and Veneziani A. A 3D/1D geometrical multiscale model of cerebral vasculature. *Journal of Engineering Mathematics*, 64(4):319–330, 2009. Cited on page 11.

[146] Peiffer V, , Sherwin SJ, and Weinberg PD. Computation in the rabbit aorta of a new metric – the transverse wall shear stress – to quantify the multidirectional character of disturbed blood flow. *Journal of Biomechanics*, 46(15):2651–2658, 2013. Cited on pages 62 and 73.

[147] Peiffer V, Sherwin SJ, and Weinberg PD. Does low and oscillatory wall shear stress correlate spatially with early atherosclerosis? A systematic review. *Cardiovascular Research*, 99(2):242–250, 2013. Cited on page 75.

[148] Penn DL, Komotar RJ, and Connolly ES. Hemodynamic mechanisms underlying cerebral aneurysm pathogenesis. *Journal of Clinical Neuroscience*, 18(11):1435–1438, 2011. Cited on page 58.

[149] Penn DL, Witte SR, Komotar RJ, and Connolly ES. The role of vascular remodeling and inflammation in the pathogenesis of intracranial aneurysms. *Journal of Clinical Neuroscience*, 21(1):28–32, 2014. Cited on page 4.

[150] Perktold K, Gruber K, Kenner T, and Florian H. Calculation of pulsatile flow and particle paths in an aneurysm model. *Basic Research in Cardiology*, 79(3):253–261, 1984. Cited on page 6.

[151] Piccinelli M, Bacigaluppi S, Boccardi E, Ene-Iordache B, Remuzzi A, Veneziani A, and Antiga L. Geometry of the internal carotid artery and recurrent patterns in location, orientation and rupture status of lateral aneurysms: An image-based computational study. *Neurosurgery*, 68(5):1270–1285, 2011. Cited on pages 3, 58 and 59.

[152] Piccinelli M, Veneziani A, D. A. Steinman DA, Remuzzi A, and Antiga L. A framework for geometric analysis of vascular structures: Application to cerebral aneurysms. *IEEE Transactions on Medical Imaging*, 28(8):1141–1155, 2009. Cited on pages 61 and 63.

[153] Piotin M, Gailloud P, Bidaut L, Mandai S, Muster M, Moret J, and Rüfenacht DA. CT angiography, MR angiography and rotational digital subtraction angiography for volumetric assessment of intracranial aneurysms: An experimental study. *Neuroradiology*, 45(6):404–409, 2003. Cited on page 14.

[154] Raaymakers TW, Rinkel GJE, Limburg M, and Algra A. Mortality and morbidity of surgery for unruptured intracranial aneurysms: A meta-analysis. *Stroke*, 29(8):1531–1538, 1998. Cited on page 3.

[155] Radaelli AG, Augsburger L, Cebral JR, Ohta M, Rüfenacht DA, Balossino R, Benndorf G, Hose DR, Marzo A, Metcalfe RW, Mortier P, Mut F, Reymond P, Socci L, Verhegghe B, and Frangi AF. Reproducibility of haemodynamical simulations in a subject-specific stented aneurysm model: A report on the Virtual Intracranial Stenting Challenge 2007. *Journal of Biomechanics*, 41(10):2069–2081, 2008. Cited on pages 14, 26, 34 and 36.

[156] Raffel M, Willert C, Wereley ST, and Kompenhans J. *Particle image velocimetry: A practical guide*. Springer, 2nd edition, 2007. Cited on page 27.

[157] Raschi M, Mut F, Byrne G, Putman CM, Tateshima S, nuela FV, Tanoue T, Tanishita K, and Cebral JR. CFD and PIV analysis of hemodynamics in a growing intracranial aneurysm. *International Journal for Numerical Methods in Biomedical Engineering*, 28(2):214–228, 2012. Cited on page 33.

[158] Reneman RS, Arts T, and Hoeks AP. Wall shear stress – an important determinant of endothelial cell function and structure – in the arterial system in vivo: Discrepancies with theory. *Journal of Vascular Research*, 43(3):251–269, 2006. Cited on pages 4 and 16.

[159] Rinkel GJE, Djibuti M, Algra A, and van Gijn J. Prevalence and risk of rupture of intracranial aneurysms: A systematic review. *Stroke*, 29(1):251–256, 1998. Cited on page 2.

[160] Romijn M, Gratama van Andel HAF, van Walderveen MA, Sprengers ME, van Rijn JC, van Rooij WJ, Venema HW, Grimbergen CA, den Heeten GJ, and Majoie CB. Diagnostic accuracy of CT angiography with matched mask bone elimination for detection of intracranial aneurysms: Comparison with digital subtraction angiography and 3D rotational angiography. *American Journal of Neuroradiology*, 29(1):134–139, 2008. Cited on pages 14 and 15.

[161] Ruigrok YM, Rinkel GJE, and Wijmenga C. Genetics of intracranial aneurysms. *The Lancet: Neurology*, 24(3):371–377, 1993. Cited on page 3.

[162] Sadasivan C, Fiorella DJ, Woo HH, and Lieber BB. Physical factors effecting cerebral aneurysm pathophysiology. *Annals of Biomedical Engineering*, 41(7):1347–1365, 2013. Cited on pages 3, 4, 58 and 74.

[163] Schneiders JJ, Ferns SP, van Ooij P, Siebes M, Nederveen AJ, van den Berg R, van Lieshout J, Jansen G, VanBavel E, and Majoie CB. Comparison of Phase-Contrast MR Imaging and Endovascular Sonography for Intracranial Blood Flow Velocity Measurements. *American Journal of Neuroradiology*, 33(9):1786–1790, 2012. Cited on pages 4 and 10.

[164] Schneiders JJ, Marquering HA, Antiga L, van den Berg R, VanBavel E, and Majoie CB. Intracranial aneurysm neck size overestimation with 3D rotational angiography: The impact on intra-aneurysmal hemodynamics simulated with computational fluid dynamics. *American Journal of Neuroradiology*, 34(1):121–128, 2013. Cited on pages 10 and 37.

[165] Schneiders JJ, Marquering HA, van den Berg R, VanBavel E, Velthuis B, Rinkel GJE, and Majoie CB. Rupture-associated changes of cerebral aneurysm geometry: High-resolution 3D imaging before and after rupture. *American Journal of Neuroradiology*, 35(7):1358–1362, 2014. Cited on page 10.

[166] Schneiders JJ, VanBavel E, Majoie CB, Ferns SP, and van den Berg R. A flow-diverting stent is not a pressure-diverting stent. *American Journal of Neuroradiology*, 34(1):E1–4, 2013. Cited on page 4.

[167] Sforza DM, Putman CM, and Cebral JR. Hemodynamics of cerebral aneurysms. *Annual Review of Fluid Mechanics*, 41:91–107, 2009. Cited on page 26.

[168] Sforza DM, Tateshima CMPS, nuela FV, and Cebral JR. Effects of perianeurysmal environment during the growth of cerebral aneurysms: A case study. *American Journal of Neuroradiology*, 33(6):1115–1120, 2012. Cited on pages 10 and 73.

[169] Shimogonya Y, Ishikawa T, Imai Y, Matsuki N, and Yamaguchi T. Can temporal fluctuation in spatial wall shear stress gradient initiate a cerebral aneurysm? A proposed novel hemodynamic index, the gradient oscillatory number (GON). *Journal of Biomechanics*, 42(4):550–554, 2009. Cited on pages 26, 58, 72, 73 and 75.

[170] Shojima M, Oshima M, Takagi K, Torii R, Hayakawa M, Katada K, Morita A, and Kirino T. Magnitude and role of wall shear stress on cerebral aneurysm: Computational fluid dynamic study of 20 middle cerebral artery aneurysms. *Stroke*, 35(11):2500–2505, 2004. Cited on page 40.

[171] Singh PK, Marzo A, Howard B, Rüfenacht DA, Bijlenga P, Frangi AF, Lawford PV, Coley SC, Hose DR, and Patel UJ. Effects of smoking and hypertension on wall shear stress and oscillatory shear index at the site of intracranial aneurysm formation. *Clinical Neurology and Neurosurgery*, 112(4):306–313, 2010. Cited on pages 58, 72 and 75.

[172] Spiegel M, Redel T, Zhang YJ, Struffert T, Hornegger J, Grossman RG, Doerfler A, and Karmonik C. Tetrahedral vs. polyhedral mesh size evaluation on flow velocity and wall shear stress for cerebral hemodynamic simulation. *Computer Methods in Biomechanics and Biomedical Engineering*, 14(1):9–22, 2011. Cited on page 53.

[173] Stehbens WE. Etiology of intracranial berry aneurysms. *Journal of Neurosurgery*, 70(6):823–831, 1989. Cited on pages 3, 58 and 72.

[174] Steinman DA, Hoi Y, Fahy P, Morris L, Walsh MT, Aristokleous N, Anayiotos AS, Papaharilaou Y, Arzani A, Shadden SC, Berg P, Janiga G, Bols J, Segers P, Bressloff NW, Cibis M, Gijsen FH, Cito S, Pallareacutes J, Browne LD, Costelloe JA, Lynch AG, Degroote J, Vierendeels J, Fu W, Qiao A, Hodis S, Kallmes DF, Kalsi H, Long Q, Kheyfets VO, Finol EA, Kono K, Malek AM, Lauric A, Menon PG, Pekkan K, Moghadam ME, Marsden AL, Oshima M, Katagiri K, Peiffer V, Mohamied Y, Sherwin SJ, Schaller J, Goubergrits L, Usera G, Mendina M, Valen-Sendstad K, Habets DF, Xiang J, Meng H, Yu Y, Karniadakis GE, Shaffer N, and Loth F. Variability of computational fluid dynamics solutions for pressure and flow in a giant aneurysm: The ASME 2012 Summer Bioengineering Conference CFD challenge. *Journal of Biomechanical Engineering – Transactions of the ASME*, 135(2):021016, 2013. Cited on page 37.

[175] Steinman DA, Milner JS, Norley CJ, Lownie SP, and Holdsworth DW. Image-based computational simulation of flow dynamics in a giant intracranial aneurysm. *American Journal of Neuroradiology*, 24(4):559–566, 2003. Cited on page 6.

[176] Steinman DA and Taylor CA. Flow imaging and computing: Large artery hemodynamics. *Annals of Biomedical Engineering*, 33(12):1704–1709, 2005. Cited on page 26.

[177] Sugahara T, Korogi Y, Nakashima K, Hamatake S, Honda S, and Takahashi M. Comparison of 2D and 3D digital subtraction angiography in evaluation of intracranial aneurysms. *American Journal of Neuroradiology*, 23(9):1545–1552, 2002. Cited on page 14.

[178] Sun Q, Groth A, and Aach T. Comprehensive validation of computational fluid dynamics simulations of in-vivo blood flow in patient-specific cerebral aneurysms. *Medical Physics*, 39(2):742–54, 2012. Cited on page 4.

[179] Szikora I, Berentei Z, Kulcsar Z, Barath K, Berez A, Bose A, and Nyary I. Endovascular treatment of intracranial aneurysms with parent vessel reconstruction using balloon and self expandable stents. *Acta Neurochirurgica*, 148(7):711–723, 2006. Cited on page 36.

[180] Szikora I, Berentei Z, Kulcsar Z, Marosfoi M, Vajda ZS, Lee W, Berez A, and Nelson PK. Treatment of intracranial aneurysms by functional reconstruction of the parent artery: The Budapest experience with the pipeline embolization device. *American Journal of Neuroradiology*, 31(6):1139–1147, 2010. Cited on page 3.

[181] Tanoue S, Kiyosue H, Kenai H, Nakamura T, Yamashita M, and Mori H. Three-dimensional reconstructed images after rotational angiography in the evaluation of intracranial aneurysms: Surgical correlation. *Neurosurgery*, 47(4):866–871, 2000. Cited on page 14.

[182] Taylor CA, Hughes TJR, and Zarins CK. Finite element modeling of blood flow in arteries. *Computer Methods in Applied Mechanics and Engineering*, 158(1/2):155–196, 1998. Cited on page 54.

[183] Thom A. The Flow Past Circular Cylinders at Low Speeds. *Proceedings of the Royal Society A: Mathematical, Physical and Engineering Sciences*, 141(845):651–669, 1933. Cited on page 6.

[184] Thomas JB, Milner JS, Rutt BK, and Steinman DA. Reproducibility of image-based computational fluid dynamics models of the human carotid bifurcation. *Annals of Biomedical Engineering*, 31(2):132–141, 2003. Cited on pages 14 and 22.

[185] Tremmel M, Xiang JP, Hoi Y, Kolega J, Siddiqui A, Mocco J, and Meng H. Mapping vascular response to in vivo Hemodynamics: Application to increased flow at the basilar terminus. *Biomechanics and Modeling in Mechanobiology*, 9(4):421–434, 2010. Cited on pages 52 and 62.

[186] Turjman AS, Turjman F, and Edelman ER. Role of fluid dynamics and inflammation in intracranial aneurysm formation. *Circulation*, 129(3):373–382, 2014. Cited on pages 4 and 58.

[187] Ugron A, Farinas M, Kiss L, and Páal G. Unsteady velocity measurements in a realistic intracranial aneurysm model. *Experiments in Fluids*, 52(1):37–52, 2011. Cited on pages 33 and 34.

[188] Usera G, Vernet A, and Ferré JA. A parallel block-structured finite volume method for flows in complex geometry with sliding interfaces. *Flow, Turbulence and Combustion*, 81(3):471–495, 2008. Cited on pages 29 and 30.

[189] Valen-Sendstad K, Mardal KA, and Steinman DA. High-resolution computational fluid dynamics detects high-frequency velocity fluctuations in bifurcation, but not sidewall, aneurysms of the middle cerebral artery. *Journal of Biomechanics*, 46(2):402–407, 2013. Cited on page 53.

[190] van Gijn J, Kerr RS, and Rinkel GJE. Subarachnoid haemorrhage. *Lancet*, 369(9558):306–318, 2007. Cited on page 2.

[191] van Ooij P, Guédon A, Poelma C, Schneiders J, Rutten MCM, Marquering HA, Majoie CB, VanBavel E, and Nederveen AJ. Complex flow patterns in a real-size intracranial aneurysm phantom: Phase contrast MRI compared with particle image velocimetry and computational fluid dynamics. *NMR in Biomedicine*, 25(1):14–26, 2012. Cited on page 31.

[192] van Ooij P, Potters WV, Guédon A, Schneiders J, Marquering HA, Majoie CB, VanBavel E, and Nederveen AJ. Wall shear stress estimated with phase contrast MRI in an in vitro and in vivo intracranial aneurysm. *Journal of Magnetic Resonance Imaging*, 38(4):876–884, 2013. Cited on page 4.

[193] van Rooij WJ, Bechan RS, Peluso JP, and Sluzewski M. Endovascular treatment of intracranial aneurysms in the flow diverter era: Frequency of use and results in a consecutive series of 550 treatments in a single centre. *Interventional Neuroradiology*, 20(4):428–435, 2014. Cited on page 3.

[194] van Rooij WJ and Sluzewski M. Procedural morbidity and mortality of elective coil treatment of unruptured intracranial aneurysms. *American Journal of Neuroradiology*, 27(8):1678–1680, 2006. Cited on page 3.

[195] van Rooij WJ, Sprengers ME, de Gast AN, Peluso JP, and Sluzewski M. 3D rotational angiography: The new gold standard in the detection of additional intracranial aneurysms. *American Journal of Neuroradiology*, 29(5):976–979, 2008. Cited on page 14.

[196] VanBavel E. Effects of shear stress on endothelial cells: possible relevance for ultrasound applications. *Progress in Biophysics and Molecular Biology*, 93(1–3):374–383, 2007. Cited on page 4.

[197] Venugopal P, Valentino D, Schmitt H, Villablanca JP, nuela FV, and Duckwiler G. Sensitivity of patient-specific numerical simulation of cerebal aneurysm hemodynamics to inflow boundary conditions. *Journal of Neurosurgery*, 106(6):1051–1060, 2007. Cited on page 22.

[198] Villa-Uriol MC, Berti G, Hose DR, Marzo A, Chiarini A, Penrose J, Pozo JM, Schmidt JG, Singh PK, Lycett R, Larrabide I, and Frangi AF. @neurIST complex information processing toolchain for the integrated management of cerebral aneurysms. *Interface Focus*, 1(3):308–319, 2011. Cited on pages 40, 41, 59 and 61.

[199] Vlak MHM, Rinkel GJE, Greebe P, van der Bom JG, and Algra A. Trigger factors for rupture of intracranial aneurysms in relation to patient and aneurysm characteristics. *Journal of Neurology*, 259(7):1298–1302, 2012. Cited on page 4.

[200] Watton PN, Raberger NB, Holzapfel GA, and Ventikos Y. Coupling the hemodynamic environment to the evolution of cerebral aneurysms: Computational framework and numerical examples. *Journal of Biomechanical Engineering*, 131(10):101003, 2009. Cited on pages 11 and 74.

[201] Watton PN, Selimovic A, Raberger NB, Huang P, Holzapfel GA, and Ventikos Y. Modelling evolution and the evolving mechanical environment of saccular cerebral aneurysms. *Biomechanics and Modeling in Mechanobiology*, 10(1):109–132, 2010. Cited on pages 11 and 74.

[202] White CR, Haidekker M, Bao X, and Frangos JA. Temporal gradients in shear, but not spatial gradients, stimulate endothelial cell proliferation. *Circulation*, 103(20):2508–2513, 2001. Cited on page 73.

[203] White CR, Stevens HY, Haidekker M, and Frangos JA. Temporal gradients in shear, but not spatial gradients, stimulate ERK1/2 activation in human endothelial cells. *American Journal of Physiology: Heart and Circulatory Physiology*, 289(6):H2350–H2355, 2005. Cited on page 73.

[204] White PM, Wardlaw JM, and Easton V. Can noninvasive imaging accurately depict intracranial aneurysms? A systematic review. *Radiology*, 217(2):361–370, 2000. Cited on page 14.

[205] Wiebers DO, 3rd JH, Whisnant JP, Jr. RDB, Meissner I, Piepgras DG, Forbes GS, Thielen K, Nichols D, O'Fallon WM, Peacock J, Jaeger L, Kassell NF, Kongable-Beckman GL, and Torner JC. Unruptured intracranial aneurysms: Natural history, clinical outcome, and risks of surgical and endovascular treatment. *Lancet*, 362(9378):103–110, 2003. Cited on page 3.

[206] Willinsky RA, Taylor SM, TerBrugge K, Farb RI, Tomlinson G, and Montanera W. Neurologic complications of cerebral angiography: Prospective analysis of 2,899 procedures and review of the literature. *Radiology*, 227(2):522–528, 2003. Cited on page 14.

[207] Womersley JR. Method for the calculation of velocity, rate of flow and viscous drag in arteries when the pressure gradient is known. *Journal of Physiology*, 127(3):553–563, 1955. Cited on page 54.

[208] Wootton DM and Ku DN. Fluid mechanics of vascular systems, diseases, and thrombosis. *Annual Review of Biomedical Engineering*, 1:299–329, 1999. Cited on page 36.

[209] Xiang JP, Natarajan SK, Tremmel M, Ma D, Mocco J, Hopkins LN, Siddiqui AH, Levy EI, and Meng H. Hemodynamic-morphologic discriminants for intracranial aneurysm rupture. *Stroke*, 42(1):144–152, 2011. Cited on pages 40, 52, 53 and 72.

[210] Zamir M. *The physics of pulsatile flow*. Springer-Verlag, 2000. Cited on pages 5 and 54.

[211] Zenteno MA, Santos-Franco JA, Freitas-Modenesi J, Gómez C, Murillo-Bonilla L, Aburto-Murrieta Y, Díaz-Romero R, Nathal E, Gómez-Llata S, and Lee A. Use of the sole stenting technique for the management of aneurysms in the posterior circulation in a prospective series of 20 patients. *Plos One*, 8(1):e55413, 2013. Cited on page 36.

[212] Zhao M, Amin-Hanjani S, Ruland S, Curcio AP, Ostergren L, and Charbel FT. Regional cerebral blood flow using quantitative MR angiography. *American Journal of Neuroradiology*, 28(8):1470–1473, 2007. Cited on page 74.

Curriculum Vitae

Arjan Geers* was born on April 28, 1983 in Naarden, The Netherlands. He grew up in Almere, a planned city 30 km to the east of Amsterdam. After attending primary school at Klaverweide (1987–1990) and Duizendpoot (1990–1996), and high school at Oostvaarders College (1996–2002), he went on to study at the University of Amsterdam. In 2006, he obtained a BSc degree in Physics and Astrophysics. His BSc thesis project, carried out at the Academic Medical Center (AMC) in Amsterdam under the supervision of Dr. Geert Streekstra, was about detecting the topology of coronary vessel trees from cryomicrotome images. In 2008, he obtained a MSc degree (*cum laude*) in Biomedical Physics. He wrote his MSc thesis under the supervision of Prof. Ed van Bavel about computational modeling of blood flow in cerebral aneurysms. Research for this project was conducted at the AMC and during a 6-month research stay at the Universitat Pompeu Fabra (UPF) in Barcelona, Spain. After graduation, he returned to Barcelona to begin his PhD studies under the supervision of Dr. Ignacio Larrabide and Prof. Alejandro Frangi.

During his time in Barcelona, he continued working on computational modeling of blood flow in cerebral aneurysms. Through his work, he has gained interest and expertise in computational fluid dynamics, shape analysis of 3D geometries, medical device modeling, and medical image analysis.

Since November 2013, Arjan has been living in London, UK. As of Februari 2015, he will be living in Edinburgh, UK.

*Arjan's full name is Adrianus Johannes Geers. For all but official documents, he uses Arjan Geers. The name he uses on scientific publications is a combination of the two: Arjan J. Geers. It preserves the two initials, making it easier to find in academic databases, and the name by which he is generally known.

Publications

Journal papers

1. **Geers AJ**, Morales HG, Larrabide I, Butakoff C, Frangi AF. *Wall shear stress at the aneurysm initiation site.* [Prepared for submission]

2. Berg P, Roloff C, Beuing O, Sugiyama SI, Aristokleous N, Anayiotos AS, Ashton N, Bressloff NW, Brown AG, Chung BJ, Cebral JR, Copelli G, Fu W, Qiao A, **Geers AJ**, Hodis S, Dragomir-Daescu D, Imdieke E, Khan MO, Valen-Sendstad K, Kono K, Meng H, Xiang J, Menon PG, Albal PG, Mierka O, Münster R, Morales HG, Osman J, Goubergrits L, Pallares J, Cito S, Passalacqua A, Piskin S, Pekkan K, Ramalho S, Marques N, Sanchi S, Schumacher KR, Sturgeon J, Švihlová H, Hron J, Usera G, Mendina M, Steinman DA, Janiga G. *The Computational Fluid Dynamics Rupture Challenge 2013 – Phase II: Variability of hemodynamic simulations in two intracranial aneurysms.* [Under review]

3. Larrabide I, **Geers AJ**, Morales HG, Bijlenga P, Rüfenacht DA. *Change in aneurysmal flow pulsatility after flow diverter treatment.* Computerized Medical Imaging and Graphics, 2015. [Published online ahead of print]

4. Tobon-Gomez C, **Geers AJ**, Peters J, Weese J, Pinto K, Karim R, Ammar M, Daoudi A., Margeta J, Sandoval Z, Stender B, Zheng Y, Zuluaga MA, Betancur J, Ayache N, Chikh MA, Dillenseger JL, Kelm BM, Mahmoudi S, Ourselin S, Schlaefer A, Schaeffter T, Razavi R, Rhode KS. *Benchmark for algorithms segmenting the left atrium from 3D CT and MRI datasets.* IEEE Transactions on Medical Imaging, 2015. [Published online ahead of print]

5. Cito S, **Geers AJ**, Arroyo MP, Palero VR, Pallarés J, Vernet A, Blasco J, San Román L, Fu W, Qiao A, Janiga G, Miura Y, Ohta M, Mendina M, Usera G, Frangi AF. *Accuracy and reproducibility of patient-specific hemodynamic models of stented intracranial aneurysms: Report on the Virtual Intracranial Stenting Challenge 2011.* Annals of Biomedical Engineering, 43(1):154–167, 2015.

6. **Geers AJ**, Larrabide I, Morales HG, Frangi AF. *Approximating hemodynamics of cerebral aneurysms with steady flow simulations.* Journal of Biomechanics, 47(1):178–185, 2014.

7. Larrabide I, **Geers AJ**, Morales HG, Frangi AF, Aguilar ML, Rüfenacht DA. *Effect of aneurysm and ICA morphology on hemodynamics before and after flow diverter treatment.* Journal of Neurointerventional Surgery, 2014. [Published online ahead of print]

8. Morales HG, Larrabide I, **Geers AJ**, San Román L, Blasco J, Macho JM, Frangi AF. *A virtual coiling technique for image-based aneurysm models by dynamic path planning.* IEEE Transactions on Medical Imaging, 32(1):119–129, 2013.

9. Morales HG, Larrabide I, **Geers AJ**, Dai D, Kallmes DF, Frangi AF. *Analysis and quantification of endovascular coil distribution inside saccular aneurysms using histological images.* Journal of Neurointerventional Surgery, 5:iii33–37, 2013.

10. Morales HG, Larrabide I, **Geers AJ**, Aguilar ML, Frangi AF. *Newtonian and non-Newtonian blood flow in coiled cerebral aneurysms.* Journal of Biomechanics, 46(13):2158–2164, 2013.

11. Larrabide I, Aguilar ML, Morales HG, **Geers AJ**, Kulcsár Z, Rüfenacht DA, Frangi AF. *Intra-aneurysmal pressure and flow changes induced by flow diverters: Relation to aneurysm size and shape.* American Journal of Neuroradiology, 34(4):816–822, 2012.

12. Larrabide I, Villa-Uriol MC, Cardenes R, Barbarito V, Carotenuto L, **Geers AJ**, Morales HG, Pozo JM, Mazzeo MD, Bogunovic H, Omedas P, Riccobene C, Macho JM, Frangi AF. *AngioLab: A software tool for morphological analysis and endovascular treatment planning of intracranial aneurysms.* Computer Methods and Programs in Biomedicine, 108(2):806–819, 2012.

13. **Geers AJ**, Larrabide I, Radaelli AG, Bogunovic H, Kim M, Gratama van Andel HAF, Majoie CB, VanBavel E, Frangi AF. *Patient-specific computational hemodynamics of intracranial aneurysms from 3D rotational angiography and CT angiography: An in vivo reproducibility study.* American Journal of Neuroradiology, 32(3):581–586, 2011.

14. Villa-Uriol MC, Larrabide I, Pozo JM, Kim M, Camara O, De Craene M, Zhang C, **Geers AJ**, Morales HG, Bogunovic H, Cardenes R, Frangi AF. *Toward integrated management of cerebral aneurysms.* Philosophical Transactions of the Royal Society A: Mathematical, Physical, and Engineering Sciences, 368(1921):2961–2982, 2010.

Conference papers

1. Larrabide I, **Geers AJ**, Aguilar ML, Morales HG, Rufenacht DA, Frangi AF. *Influence of vascular morphology on hemodynamic changes after flow diverter placement in saccular intracranial aneurysms.* MICCAI Workshop on Computer Assisted Stenting (STENT), Nice, France, 2012.

2. Morales HG, Larrabide I, Aguilar M, **Geers AJ**, Macho JM, San Roman L, Frangi AF. *Comparison of two techniques of endovascular coil modeling in cerebral aneurysms using CFD.* International Symposium on Biomedical Imaging (ISBI), Barcelona, Spain, 2012.

3. **Geers AJ**, Larrabide I, Morales HG, Villa-Uriol MC, Frangi AF. *Comparing geometry and hemodynamics of MCA aneurysms.* International Conference on Mathematical and Computational Biomedical Engineering (CMBE), Washington, DC, USA, 2011.

4. Morales HG, Larrabide I, Villa-Uriol MC, **Geers AJ**, Frangi AF. *Towards the validation of a virtual coiling technique using a real versus a simulated bolus injection.* International Conference on Mathematical and Computational Biomedical Engineering (CMBE), Washington, DC, USA, 2011

5. **Geers AJ**, Larrabide I, Morales HG, Frangi AF. *Comparison of steady-state and transient blood flow simulations of intracranial aneurysms.* International Conference of the IEEE Engineering in Medicine and Biology Society (EMBC), Buenos Aires, Argentina, 2010.

6. Villa-Uriol MC, Larrabide I, Pozo JM, Bogunovic H, Omedas P, Barbarito V, Carotenuto L, Riccobene C, Planes X, Martelli Y, **Geers AJ**, Frangi AF. *AngioLab: Integrated technology for patient-specific management of intracranial aneurysms.* International Conference of the IEEE Engineering in Medicine and Biology Society (EMBC), Buenos Aires, Argentina, 2010.

7. **Geers AJ**, Larrabide I, Radaelli AG, Bogunovic H, Gratama van Andel HAF, Majoie CB, Frangi AF. *Reproducibility of image-based computational hemodynamics in intracranial aneurysms: Comparison of CTA and 3DRA*. International Symposium on Biomedical Imaging (ISBI), Boston, MA, USA, 2009.

Conference abstracts

1. **Geers AJ**, Morales HG, Larrabide I, Butakoff C, Frangi AF. *Wall shear stress at aneurysm initiation site*. International Symposium on Biomechanics in Vascular Biology and Cardiovascular Disease, Montreal, QC, Canada, 2014.

2. Cito S, Pallares J, Vernet A, **Geers AJ**, Cuesta I. *Hemodynamics analysis of several stent treatments of a patient specific anterior communicating artery aneurysm.* ASME Summer Bioengineering Conference (SBC), Fajardo, Puerto Rico, USA, 2012.

3. Cito S, **Geers AJ**, Arroyo P, Pallares J, Vernet A, Palero VR, Lobera J, Frangi AF. *Particle imaging velocimetry benchmark for validation of three-dimensional computational fluid dynamics in a cerebral aneurysm model.* International Interdisciplinary Cerebrovascular Symposium (ICS), Shanghai, China, 2011.

4. **Geers AJ**, Larrabide I, Morales HG, Frangi AF. *Relationship between geometry and hemodynamics of MCA aneurysms.* International Interdisciplinary Cerebrovascular Symposium (ICS), Shanghai, China, 2011.

5. Larrabide I, Aguilar M, Morales HG, **Geers AJ**, Rüfenacht DA, Frangi AF. *Hemodynamic quantification of aneurysms after treatment with flow diversion device.* International Interdisciplinary Cerebrovascular Symposium (ICS), Shanghai, China, 2011.

6. Morales HG, Larrabide I, **Geers AJ**, Kallmes DF, Dai D, Ding YH, Frangi AF. *Histological analysis of endovascular coil distribution.* International Interdisciplinary Cerebrovascular Symposium (ICS), Shanghai, China, 2011.

7. **Geers AJ**, Larrabide I, Morales HG, Cito S, Villa-Uriol MC, Frangi AF. *Steady-state and transient hemodynamic simulations of virtually treated intracranial aneurysms.* International Intracranial Stent Meeting (ICS), Houston, TX, USA, 2010.

8. **Geers AJ**, Radaelli AG, Majoie CB, Gratama van Andel HAF, VanBavel E, Frangi AF. *Quantitative sensitivity analysis to image modality of computed hemodynamics in intracranial aneurysms.* International Intracranial Stent Meeting (ICS), Ankara, Turkey, 2008.

Book chapters

1. Villa-Uriol MC, Larrabide I, Pozo JM, Kim M, De Craene M, Camara O, Zhang C, **Geers AJ**, Bogunovic H, Morales HG, Frangi AF. *Cerebral aneurysms: A patient-specific and image-based management pipeline.* Computational Vision and Medical Image Processing: Recent Trends, Springer, 19:327–349, 2011.

Letters

1. **Geers AJ**, Larrabide I, Radaelli AG, Bogunovic H, Kim M, Frangi AF, Gratama van Andel HAF, Majoie CB, VanBavel E. *Reply: Identifying "truth" in computational*

fluid dynamics research. American Journal of Neuroradiology, 32(6):E123-E123, 2011.

Blog posts

1. **Geers AJ**. *Patient-specific computational hemodynamics of intracranial aneurysms from 3D rotational angiography and CT angiography: An in vivo reproducibility study.* American Journal of Neuroradiology News Digest, December, 2014.

Data

1. **Geers AJ**. *WSS at the aneurysm initiation site: Vascular models.* Figshare. 2014. DOI: 10.6084/m9.figshare.1159108

2. **Geers AJ**. *Virtual Intracranial Stenting Challenge 2011 (VISC11): Input data.* Figshare. 2014.
DOI: 10.6084/m9.figshare.1060443

3. **Geers AJ**, Cito S, Arroyo MP, Palero VR. *Virtual Intracranial Stenting Challenge 2011 (VISC11): Particle imaging velocimetry data.* Figshare. 2014.
DOI: 10.6084/m9.figshare.1060453

4. **Geers AJ**, Cito S. *Virtual Intracranial Stenting Challenge 2011 (VISC11): CFD solutions group E.* Figshare. 2014.
DOI: 10.6084/m9.figshare.1060464

Acknowledgments

In closing, I would like to express my gratitude to the people without whose support this thesis would not have been possible.

First of all, I would like to thank my supervisors Alejandro Frangi and Ignacio Larrabide. Alex, thanks for giving me the opportunity to be part of such an ambitious research group and advising me throughout the years. The lessons I have learned at CISTIB go far beyond merely scientific research. Nacho, thank you so much for your dedication in supervising my day-to-day work. If you have limits in time or space outside of which you would not drop everything and help me out, I am not aware of it.

If there was such a thing as a peer-supervisor, I would not need a second to think of one. Hernán Morales, as fellow PhD student working on the same topic you have supported me in many different ways. You were the second pair of eyes for countless plots and problems, you were always up for improvised journal clubs, and you were a lot of fun to hang out with, both in the lab and during conference trips.

Thanks to Ed van Bavel, Charles Majoie, and Hugo Gratama van Andel from the University of Amsterdam. You are the reason I got into this field of research, went to Barcelona and started this adventure. It has been a pleasure to see your work on aneurysmal hemodynamics continue with many interesting studies.

Thanks to those that collaborated on VISC'11. To Pilar Arroyo and Virginia Palero for providing the phantom and assisting with the PIV measurements. To Luis San Román and Jordi Blasco for scanning the phantom and proposing treatment configurations. To the challenge participants for their high-quality submissions and quick feedback.

Thanks to clinicians Charles Majoie, Daniel Rüfenacht, Elio Vivas, Jordi Blasco, Juan Macho, Juhana Frösen, Luis San Román, Pankaj Singh, and Philippe Bijlenga. Computational modeling starts and ends with your invaluable input. Thanks for your enthusiasm for our work and for sharing your clinical expertise.

Thanks to the partners of the @neurIST project, especially those that contributed to the construction of the @neurIST database: Advanced Simulation & Design GmbH (Germany), ANSYS Europe Ltd (UK), Hospital Clínic i Provincial de Barcelona (Spain), Hospital General de Catalunya (Spain), Hôpitaux Universitaires de Genève (Switzerland), Royal Hallamshire Hospital (UK), Super Computing Solution s.r.l. (Italy), The University of Sheffield (UK), and Université de Genève (Switzerland). It was a wonderful experience

to participate in a large collaboration between academia, industry, and clinical centers.

Open science practices allow scientists to see further and progress faster. Much of the work presented in this thesis greatly benefited from open-source software and I would like to especially highlight the Vascular Modeling Toolkit (VMTK) developed by Luca Antiga. Luca, thank you so much for your important contribution to the field in general and my thesis in particular. Thanks for the stimulating discussions and for sparking my interest in Python.

Many thanks to Bart Bijnens for his scientific mentorship throughout the PhD. Often accompanied by beer and good food, you sanity checked my ideas, entertained discussions about anything, and in the face of academic politics always brought the conversation back to research.

Thanks to Oscar Camara for welcoming me to the office and seminars of PhySense. Your continuation of biomedical research at DTIC made the last few years of the PhD a lot easier.

Thanks to the people of CISTIB I directly worked with. To Alessandro Radaelli for supervising my work in the first couple of months. To Salvatore Cito for co-organizing the challenge and his help on all things CFD. To Martha Aguilar and Carolina Valencia for building meticulous datasets. To Gerhard Engelbrecht and María Cruz Villa-Uriol for helping me make some sense out of the @neurIST database. To José María Pozo for the many physics discussions. To Hrvoje Bogunović for his segmentations and for gladly sharing his knowledge on medical imaging. To Minsuok Kim for his tangible enthusiasm for science. To Constantine Butakoff for being able to solve any problem.

Big thanks to all the people of CISTIB for creating such an enjoyable environment and to everyone from Més Que Un Social Club and The Dark Side for making Barcelona an even better city to live. Thanks to Tampa (Vaselin) and La Cervecita (Angie and Joaquin) for hosting us numerous times.

Doing research and 'being a lab' is not possible without the support from administrative staff. I would like to give special thanks to CISTIB's PMO and to DTIC's *secretaria* for keeping things running so smoothly, even under unusual circumstances.

Mom and dad, thanks for your support, your interest in my work, and for fully embracing every new step we take. Vincent, thanks for being a great example as my big brother. During my PhD I have had the fortune to see my family grow. With Kerstin, Alejo, Paola, Luz Dary, Robert, Nacho, and Nancy I seem to have won the in-law jackpot.

Cata, you are my favorite kind of superhero: loving, caring, patient, funny, smart, and, at times, a little crazy. You have helped me in every possible way during the PhD. I am very lucky to share my life with you.